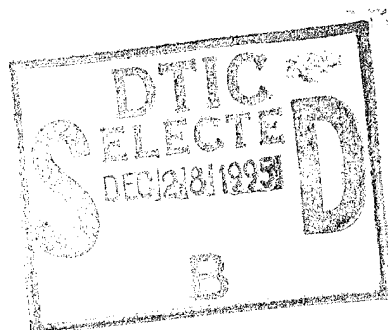NASA Contractor Report 3881

Longitudinal Splitting in Unidirectional Composites, Analysis and Experiments

James G. Goree and Jeffrey M. Wolla
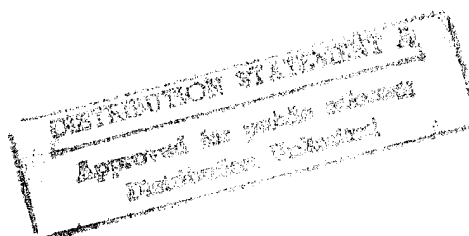
DTIC
SELECTED
DEC 28 1995
B

DEPARTMENT OF DEFENSE
PLASTICS TECHNICAL EVALUATION CENTER
PCSTINCOM, DOVER, N. J. 07801

19951214 016

DISTRIBUTION STATEMENT A
Approved for public release;
Distribution Unlimited

NASA

DISCLAIMER NOTICE

UNCLASSIFIED

Technical Report
distributed by

DEFENSE
TECHNICAL
INFORMATION
CENTER

DTIC Acquiring Information-
Imparting Knowledge

Cameron Station
Alexandria, Virginia 22304-6145

UNCLASSIFIED
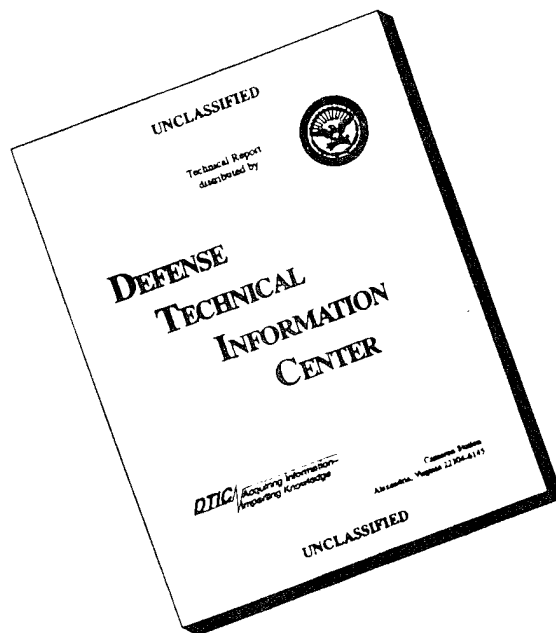
THIS DOCUMENT IS BEST QUALITY AVAILABLE. THE COPY FURNISHED TO DTIC CONTAINED A SIGNIFICANT NUMBER OF PAGES WHICH DO NOT REPRODUCE LEGIBLY.

```
--    1   OF      1
--                    **DTIC DOES NOT HAVE THIS ITEM**
-- 1 -   AD NUMBER: D439451
-- 5 -   CORPORATE AUTHOR: CLEMSON UNIV  SC DEPT OF MECHANICAL ENGINEERING
-- 6 -   UNCLASSIFIED TITLE:      LONGITUDINAL SPLITTING IN UNIDIRECTIONAL
--       COMPOSITES, ANALYSIS AND EXPERIMENTS.
--10 -   PERSONAL AUTHORS: GOREE,J. G. ;WOLLA,J. M. ;
--11 -   REPORT DATE:        APR    1980
--12 -   PAGINATION:    114P
--15 -   CONTRACT NUMBER: NSG-1297
--18 -   MONITOR ACRONYM: NASA
--19 -   MONITOR SERIES:  CR-3081
--20 -   REPORT CLASSIFICATION: UNCLASSIFIED
--22 -   LIMITATIONS (ALPHA):     APPROVED FOR PUBLIC RELEASE; DISTRIBUTION
--       UNLIMITED. AVAILABILITY: NATIONAL TECHNICAL INFORMATION SERVICE,
--       SPRINGFIELD, VA. 22161  NASA CR-3081.
--33 -   LIMITATION CODES:   1
--******
--                    END OF DISPLAY LIST

--              <<ENTER NEXT COMMAND>>
```

NASA Contractor Report 3881

Longitudinal Splitting in Unidirectional Composites, Analysis and Experiments

James G. Goree and Jeffrey M. Wolla

Clemson University
Clemson, South Carolina

NASA

National Aeronautics
and Space Administration

Scientific and Technical
Information Branch

1985

TABLE OF CONTENTS

ACKNOWLEDGMENTS

LIST OF FIGURES

List of Figures (Cont'd)

LIST OF TABLES

LIST OF SYMBOLS

A_F	Fiber cross-sectional area.
$A(\theta)$	Function defined in Equation (35).
AE	Acoustic emission.
B_m	Fourier series coefficients.
COD	Crack opening displacement.
d	Spacing between fibers.
$D^2(\theta)$	Function defined in Equation (30).
E_F	Fiber modulus.
$f(\eta)$	Function defined in Equation (23).
FFD	Film-to-focus distance.
$g(\eta)$	Axial displacement difference defined in Equation (39).
G_M	Shear modulus of the matrix region.
h	Shear transfer distance.
ℓ	Axial split length.
L	Total axial damage length.
LEFM	Linear elastic fracture mechanics.
m	Broken fiber index.
n	Fiber index number.
N	Index number of the last broken fiber.
NBF	Number of broken fibers.
t	Lamina thickness.
T_o	Material parameter defined in Equation (18).
$u(y)|_n$	Transverse displacement of the nth fiber.
$v(y)|_n$	Axial displacement of the nth fiber.

$V(\eta)\|_n$	Normalized axial displacement.
$V(\eta,\theta)$	Transform function for the axial displacement as defined in Equation (24).
y	Axial coordinate.
α	Normalized total axial damage length.
β	Normalized axial split length.
$\delta^2(\theta)$	Function defined in Equation (30).
η	Normalized axial coordinate.
$\sigma_F(y)\|_n$	Axial fiber stress in the nth fiber.
$\sigma_M(y)\|_n$	Transverse matrix normal stress in the region bounded by the (n-1) and (n) fibers.
σ_n	Stress concentration for the nth fiber.
σ_∞	Applied remote tensile stress.
$\tau(y)\|_n$	Shear stress within the matrix region bounded by the (n-1) and (n) fibers.
τ_o	Matrix yield stress in shear.
τ_o	Normalized yield stress in shear.
$<\ >$	Unit step function.

CHAPTER I

INTRODUCTION

Composite materials are, in general, formed when two or more chemically distinct materials are combined so that a distinct interface will separate the components (as opposed to alloys). Each of the constituent materials has its own physical properties, but the resulting composite has properties different from each material alone. It is desirable for the composite to take advantage of selected properties from each constituent. Of the several types of composite materials, the category of particular interest is the continuous fiber-reinforced, or fibrous, composite. This type consists of one phase which is usually much stronger (fiber) than the other phase (matrix). This combination leads to anisotropic properties which provide the capability of designing for specific characteristics such as high strength in one critical direction. This is also the composite material that has been the most analyzed and reported in the literature.

The text [1] by Jones presents a macroscopic approach to predicting composite properties and behavior. A more statistical approach is presented by Zweben [2] where the statistical scatter of fiber strength and local fiber overstress due to fiber discontinuities are considered. These analyses concentrate on initially undamaged composites.

Work is also being done where some type of initial damage is present in the laminate, usually in the form of a crack through both the fiber and matrix. The goal is to determine how the composite strength and fracture behavior under loading are affected by this damage. Some

of the fracture processes known to occur in fibrous composites are plastic deformation, matrix microcracking and macrocracking, fiber fracture, fiber-matrix debonding, and delamination between laminae. Zweben [3] discusses some of the macroscopic and micromechanical approaches that have been used to predict strength and crack propagation in the damaged composite. A macroscopic approach typically treats the composite as a homogeneous, anisotropic material and applies classical linear elastic fracture mechanics (LEFM). This method has been successful only up to the point where the complex modes of failure due to the heterogeneity of the composite begin to occur. These failure modes affect stress distributions in a manner unaccountable for by LEFM.

On the micromechanical level, the heterogeneity of the composite is considered. The composite is separated into fiber, matrix, interface, and interlaminar regions. Zweben points out that the drawback to using LEFM at this level is the extreme complexity of the analysis involved. Kanninen, Rybicki, and Griffith [4] have completed preliminary development of a model which considers a small, heterogeneous region at the crack tip. The rest of the composite is taken as an elastic, anisotropic continuum. The heterogeneous region is modeled by finite element methods and is capable of simulating several different fracture modes. This model is limited to small damage zones, though, since the assumed damage can not exceed the boundary between the heterogeneous region and the anisotropic continuum.

The approach Zweben concentrates on is the "material modeling" concept. In this method, assumptions about the material behavior are made in an effort to simplify the analysis. The resulting simplified model should incorporate the major influences affecting fracture. Zweben

specifically deals with the shear-lag stress transfer mechanism for 0° layers. The shear-lag model assumes that the extensional stiffness of the fibers is much larger than that of the matrix. As a result, the fibers carry all the extensional stresses and the matrix only shear stresses. In addition, the model assumes that the matrix shear stresses are dependent only on the axial displacements of adjacent fibers. The shear-lag model was first applied to unidirectional composites by Hedgepeth [5]. He considered a two-dimensional array of fibers surrounded by matrix material with a notch consisting of an arbitrary number of broken fibers. Stress concentrations in the first unbroken fiber were determined as a function of the number of broken fibers. Hedgepeth and Van Dyke [6] extended this analysis to a three-dimensional array of fibers. They also considered a two-dimensional case with one broken fiber and matrix yielding (ideally plastic) between the broken fiber and the adjacent fiber. Later, Hedgepeth and Van Dyke [7] modified the matrix behavior to account for disbonding between the broken fiber and the matrix instead of matrix yielding. Due to the use of an influence function technique to solve these problems, only one broken fiber could be considered when matrix damage was present. Eringen and Kim [8] made use of a dual integral technique with Fourier transforms to solve a modified form of the original Hedgepeth problem. The shear-lag representation was changed to include transverse fiber displacements and the transverse matrix normal stresses were also calculated. Goree and Gross [9] extended the Eringen and Kim analysis to three-dimensions. The use of the dual integral technique and Fourier series made it possible to consider matrix damage with more than one broken fiber using the shear-lag model. Goree and Gross [10] accomplished this when they worked the

two-dimensional problem with an arbitrary number of broken fibers and both matrix yielding and splitting between the last broken fiber and the first unbroken fiber. More recent developments in the use of the shear-lag model are [11], where Dharani, Jones, and Goree considered transverse matrix and fiber damage and constraint layers.

As evidenced by the above work, the use of the shear-lag model as a simplified representation of the stress transfer at a notch tip has been well developed. As with any theory on material behavior, experimentation is necessary to validate it. It is of particular importance in the case of "material modeling". It is necessary to determine if the simplified model contains the proper approximations for stress fields and failure criteria to predict the actual material behavior adequately.

Several published accounts exist which make direct comparisons of experimental results to various analytical models. Brinson and Yeow [12] compared results for tensile tests on notched graphite/epoxy laminates to a model based on LEFM. They found some agreement, but point out that the models are restricted to self similar crack growth. Peters [13] tested unidirectional boron/epoxy and boron/aluminum laminates. He also points out the inability of LEFM to account for the damage growth non-colinear with the notch. It was particularly obvious with the boron/epoxy where the low shear strength of the epoxy led to shear crack formation parallel to the fibers and complete crack blunting. He also found that the fracture behavior of laminates which did exhibit self similar crack growth was dependent on several material parameters which LEFM does not consider. On the other hand, Awerbuch and Hahn [14] reported good agreement between experimental and predicted values for fracture strengths of boron/aluminum laminates. In addition, they

report good agreement for crack opening displacement (COD) versus load curves. The model for predicting the COD incorporated longitudinal matrix damage. It is apparent that varying conclusions have been reached as to the ability of LEFM to predict composite fracture behavior. It appears, at best, to be applicable only in limited cases.

Goree and Jones [15] have conducted an extensive experimental program to compare the behavior of unidirectional, notched boron/aluminum laminates to the behavior predicted by shear-lag analysis. The model included longitudinal matrix damage and transverse matrix and fiber damage. They found that the shear lag model predicted several modes of fracture behavior accurately. Good agreement was found for COD values, amount of stable transverse notch extension and longitudinal matrix yielding, and notched fracture strengths.

The work of Goree and Jones has indicated that the shear-lag model is effective in predicting the complex fracture behavior of boron/aluminum laminates. Aluminum is a ductile matrix and exhibits longitudinal damage in the form of yielding, not splitting. It is known that unidirectional graphite/epoxy laminates will exhibit matrix splitting due to the brittle nature of the epoxy. The shear-lag model of [10] has predicted that after a split is initiated, a seven to ten percent increase in load will result in unstable split growth. This behavior has been observed qualitatively for graphite/epoxy with some experimental work reported by Mar and Lin [16]. It was the objective of this study to examine quantitatively this fracture behavior and to determine if the shear-lag model does provide an accurate prediction.

The ability to detect the precise moment of split initiation will be of prime importance to this study. A survey of recent experimental

work revealed that monitoring of acoustic emissions has gained popularity as a tool for detecting the occurrence of deformation and fracture processes in composites, as well as other types of materials, equipment, and structures. The availability of a state-of-the-art acoustic emission (AE) monitoring system[1] made this method a logical choice for use in detecting split initiation. The system could also monitor damage growth throughout the life of each test.

Acoustic emissions are defined as transient elastic waves generated by the rapid release of energy within a material. The release of energy will usually be due to deformation or fracture processes occurring in the material. The generated wave will be detected by a piezoelectric transducer and converted to an electrical signal. This signal is commonly passed through a preamplifier with a bandpass filter and then through another amplifier. After amplification, the signal can be analyzed to determine its characteristic parameters. How these parameters are defined and interpreted is dependent on how the wave is modeled.

Figure (1) shows a proposed model for the acoustic wave. It is a common approach to model the wave as a damped sinusoid, as has been done in this study. From the figure, several characteristics of the wave can be found that will be useful in quantifying the wave. These wave parameters are: counts, amplitude, duration, rise time, and energy. The threshold indicates an internal voltage threshold that must be exceeded by the signal voltage before the wave is considered to be detected. The numbers of oscillations or spikes above this threshold is the number of counts associated with the wave. The maximum oscillation or voltage is the amplitude of the wave and the time that the wave remains above the

---

1. Model 3400 Acoustic Analyzer from Physical Acoustics, Inc., Princeton, N.J.
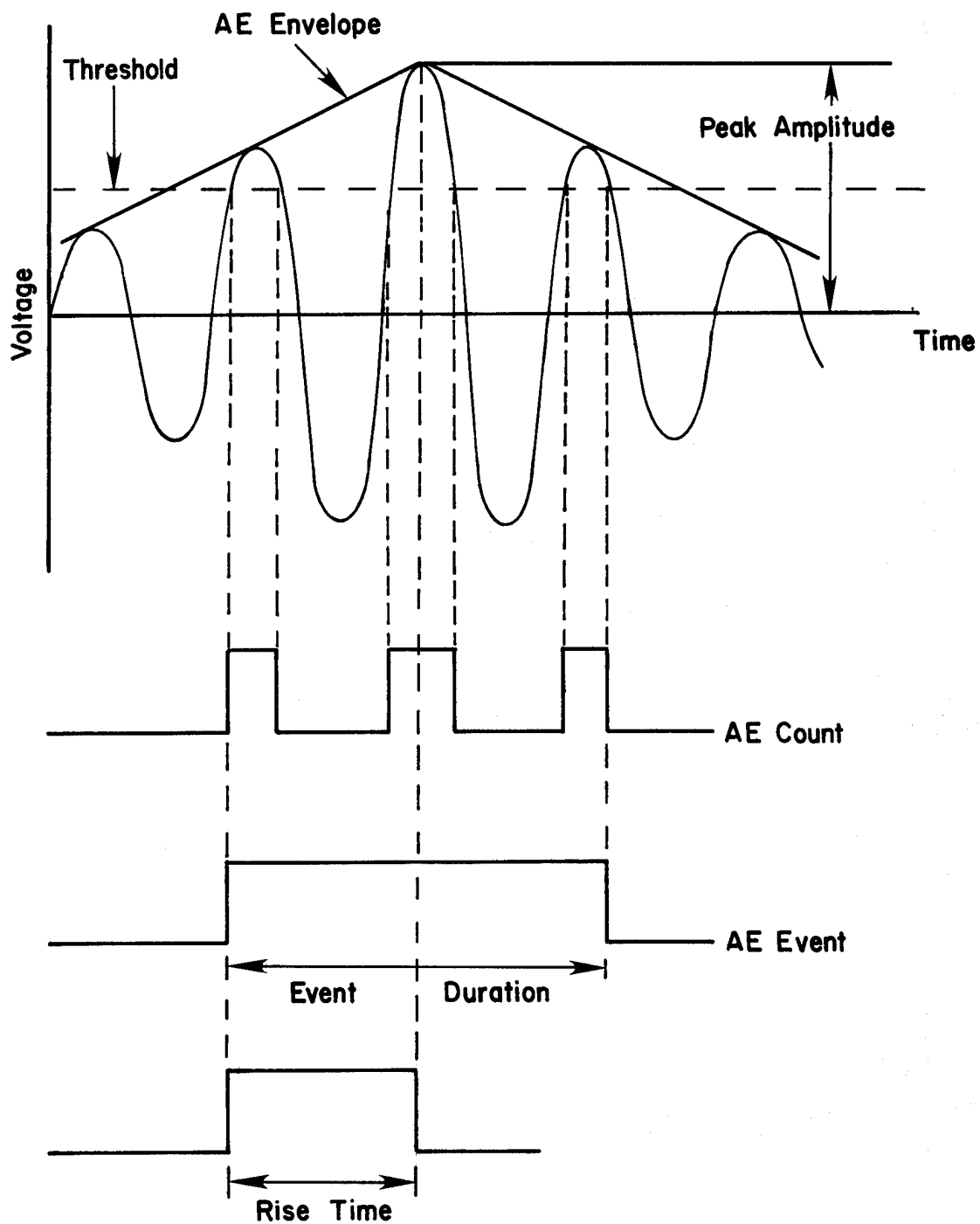
Figure 1. Model of the acoustic wave.

threshold is the duration. Rise time is defined as the time elapsed from signal detection to when the peak amplitude is reached. Finally, an integrating circuit will quantify the area under the wave envelope to give a relative energy value. Counts, amplitude, and energy have been the parameters most often measured and reported in the literature. Recently, interest has increased in examining the frequency content of the waves. Ideally, a particular type of deformation or fracture process will generate AE waves with consistent and identifiable acoustic characteristics. The identifiable characteristics would serve as the "acoustic signature" for the particular type of event and allow investigators to pinpoint the failure modes.

Another attempt to model the acoustic wave has been presented by Stephens and Pollack [17]. They consider the wave to be a pulselike function, rather than oscillatory. They describe how the pulse model satisfies the physical constraints of material deformation, while the oscillatory model does not. These constraints deal with the lengthening of a coupon or the lowering of the applied stress due to the event that generated the wave. A pulselike stress wave is of a form that can contribute to such changes, while an oscillatory stress wave has a mean value of zero and can not. Experimental data is supportive of this model, but, as Alers and Graham [18] point out, this data is in the low frequency range where resonant vibrations can be set up. This makes the results highly dependent on coupon geometry. Which model is a more accurate representation of the acoustic wave will not affect this study though, since it is the characteristics of the signal that are of interest and not how they are transmitted.

It should be pointed out that the wave parameters being used are not sufficient to completely describe the wave. Conserved properties such as momentum need to be considered to develop a complete description. As Evans and Linzer [19] point out, due to the tensor nature of the AE process, there are six independent measurements that would be needed to completely characterize a single event. The analysis and equipment are not available for this type of wave characterization, but the parameters that are considered are adequate for present applications.

AE monitoring has been used to show trends in fracture processes, but it will find ideal usage if it can be used to detect and identify particular processes. This will enable AE monitoring to be used effectively in fracture studies where several modes of failure can occur. With this in mind, several theoretical and experimental studies have been done in an attempt to correlate fracture processes to AE parameters.

Both Evans and Linzer [19] and Tetelman and Evans [20] have presented models to correlate AE to fracture processes in brittle materials. In [20], LEFM of microcracking and plastic deformation are correlated to the count rate of a damped, sinusoidal AE wave. In particular, they consider the count rate to be dependent on the energy released by the failure event. Evans and Linzer deal with similar failure processes and do a more thorough theoretical characterization of the AE wave. These studies have provided a theoretical explanation for why particular failure events will produce a particular acoustic signature. They have taken observed AE data from past experimental data and been able to correlate trends in the data to theoretical models. However, they point

out that the models are first order approximations and lack direct verification.

For fibrous composites in particular, Harris, Tetelman, and Darwish [21] have developed a theoretical model that relates AE to fiber breaks during a tensile test. A model predicts the number of AE counts that will be observed per fiber break as a function of strain level. This model is combined with an experimentally determined relation between the number of fiber breaks and the composite strain for a particular laminate. They found good experimental agreement and concluded that once the fiber breaking versus strain relation for a composite was known, it would be possible to predict the percentage of broken fibers in any subsequent test based solely on the number of AE counts. Hennecke and Jones [22] have also investigated this model. They tested different types of laminates and found good correlation. They also point out that the AE technique was more sensitive to damage than was stress-strain curve analysis. The AE would indicate subtle changes in the modulus of the laminate that were not observed from stress-strain data.

Rotem and Altus [23] have done a more complete analysis of composite fracture modes and the corresponding acoustic emissions. They used count distributions to distinguish between four different fracture modes that occurred in unidirectional laminates. The fracture modes considered were fiber fracture, matrix cracking parallel to the fibers, matrix cracking perpendicular to the fibers, and delamination. They concluded that the AE waves generated by a particular fracture mode had a unique count distribution that was characteristic of both the fracture mode and the laminate itself. They also found that the AE wave had a unique constant relation to the energy released by the fracture process. This

relation could be used as part of the acoustic signature for the fracture process.

AE monitoring has been proven to be a sensitive method for monitoring and characterizing damage in composites. These were major reasons for using AE monitoring in this study. It would be able to detect split initiation in the graphite/epoxy laminates. However, the use of AE monitoring requires some special considerations. Hamstad [24 and 25] gives a detailed account of these special considerations with an emphasis on testing of composite materials. The primary considerations for reliable AE monitoring are: extraneous noise, signal attenuation, the Kaiser effect, coupon variability, identification and interpretation of potential AE sources, and location of the AE source. These all had some effect on the experimental program used.

Extraneous noise needs to be filtered out or reduced since it may obscure the actual AE data. Primary sources of noise are testing machine vibration and the action of mechanically gripping the tabs on the ends of the test coupon. Unloading and reloading the coupon in such a manner that it must be regripped should be avoided. Also, electrical noise may be present.

Signal attenuation presents a problem in that it causes a loss of signal and possibly an alteration of the character of the signal. The signal may be altered to the point where it can no longer serve as an effective signature of the event. Factors influencing the degree of attenuation are: geometric spreading of the AE wave, material absorption of wave energy, reflection and alternate wave paths, and dispersion of the AE wave due to different speeds of propagation of the different components of the wave. The anisotropic nature of fibrous composites

compounds some of these effects. Little can be done to prevent these losses except for placing the transducers as close as possible to the suspected AE source to reduce the distance the wave must travel before being detected and,therefore, reducing the time and distance over which these factors can act. This points out the importance of identifying the location of the potential AE sources.

It is also advantageous to identify the types of AE sources that will be present. If more than one fracture mode will be present, one needs to be aware that different AE signatures will be present and need to be distinguished. For this study, it was known that the dominant form of damage would be matrix splitting parallel to the fibers and that the initial source would be located at the tips of the center notch.

The Kaiser effect is defined as the immediately irreversible characteristic of acoustic emission phenomenon resulting from an applied stress. In other words, if a coupon is loaded to a certain stress level and then unloaded, there should be no new AE upon reloading until the previous peak stress level is reached. In the case of viscoelastic materials, time at the stress level also becomes a factor. The objective of this study was not to test for the existence of the Kaiser effect, but it would be helpful if it did exist since the damage was being documented as a function of applied stress. If damage was occurring (indicated by AE being detected) during the reload cycles before the previous peak stress level was reached, then the data analysis would become more complicated.

Since it has been shown that AE signatures are dependent on the material, as well as on the type of fracture, coupon variability had to be considered. Ideally, all coupons should have come from identically

fabricated laminates, preferably from the same batch. Likewise, the coupon preparation and testing techniques should be as identical as possible for each coupon. To account for variations, it becomes necessary to duplicate all tests.

AE source location during the tests is made possible by having two or more transducers. The relative times at which an AE wave is detected at each transducer can be used to pinpoint the source location. In [26] and [27], a triangularization technique has been used successfully to locate damage and damage growth in graphite/epoxy panels. In this study, source location was used in an attempt to track the growth of the matrix splits. It was found that problems with wave propagation from splits on one side of the notch to the transducer on the opposite side of the notch made the location results unreliable.

Radiography and brittle coating techniques were also used to monitor crack growth. Goree and Jones [15] have presented the development of these procedures and any modifications for this study will be discussed in the next chapter.

To summarize, the objective of this study was to experimentally determine the fracture behavior of notched, unidirectional graphite/-epoxy laminates by the use of AE monitoring, radiography and brittle coating techniques. The point of split initiation and the rate of split growth were of primary interest. The actual behavior was compared to behavior predicted by the two-dimensional shear lag model with longitudinal matrix splitting and yielding [10].

Certain commercial materials are identified in this paper in order to specify adequately which materials were investigated in the research effort. In no case does such identification imply recommendation or

14

endorsement of the product by Clemson University, nor does it imply that the materials are necessarily the only ones or the best ones available for the purpose.

CHAPTER II

EXPERIMENTAL PROCEDURE

Materials and Coupon Preparation

The material used in this investigation was unidirectional graphite/epoxy pre-preg tape composed of T300[2] graphite fibers in an 5208[3] epoxy matrix. All laminates were eight plies thick with an average laminate thickness of 1.27 mm (0.159 mm per ply). The fiber volume fraction was 50 percent with the average fiber bundle cross-sectional area being $1.40 \times 10^{-8} m^2$ (0.134 mm diameter). The fiber cross-sectional area was found by assuming a fiber centerline spacing of 0.178 mm. The centerline spacing was also used to determine number of broken fibers (NBF) for a known notch width.

The inventory of test coupons consisted of equal numbers of 25.4, 50.8, and 73 mm wide coupons. For each coupon width (W), four different notch widths (2a) were used. The notch widths were chosen to obtain approximate notch width to coupon width ratios (2a/W) of one-eighth, three-sixteenths, one-fourth, and one-half. For the 73 mm coupons, the notch widths were calculated on the basis of a 76.2 mm coupon width. This was done so the notch widths would be multiples of the notch widths for the 25.4 mm and 50.8 mm coupons. The 73 mm width had to be used since this was the maximum width that the testing machine would accommodate. The coupon inventory is summarized in Table I and Figure (2)

---

2. T300 - graphite fibers, manufactured by Union Carbide.

3. Rigidite 5208 - epoxy resin, Registered trademark of Narmco Materials, Inc.

shows the various coupon widths and a typical graphite/epoxy sheet from which they were fabricated.

Table I. Inventory of coupons used in the study.

Coupon Width (W)	Notch Width (2a)	NBF	Quantity
25.4 mm	3.18 mm	19	2
25.4 mm	4.76 mm	27	2
25.4 mm	6.35 mm	37	3
25.4 mm	12.70 mm	71	2
50.8 mm	6.35 mm	37	3
50.8 mm	9.53 mm	55	2
50.8 mm	12.70 mm	71	2
50.8 mm	25.40 mm	143	2
73.0 mm	9.53 mm	55	2
73.0 mm	14.29 mm	81	2
73.0 mm	19.05 mm	107	2
73.0 mm	38.10 mm	215	2

The coupons were formed by shearing the laminate sheets to the appropriate widths in a metal shear. All coupons were approximately 298 mm long. The notches were machined with a diamond end mill and were centered on the coupon. The notches were not sharp edged flaws such as narrow slits, but analysis by Dharani, et. al., [11] has shown that the shape of the notch has little or no effect on the stress concentrations at the notch tip for unidirectional composites. Therefore, for economic and time reasons, end milling was chosen over more sophisticated methods such as electrostatic discharge machining (EDM) for notch formation. After being cut to the proper size, all surfaces and edges of the coupons were sanded to reduce surface flaws and provide a clean, smooth surface for strain gage attachment.
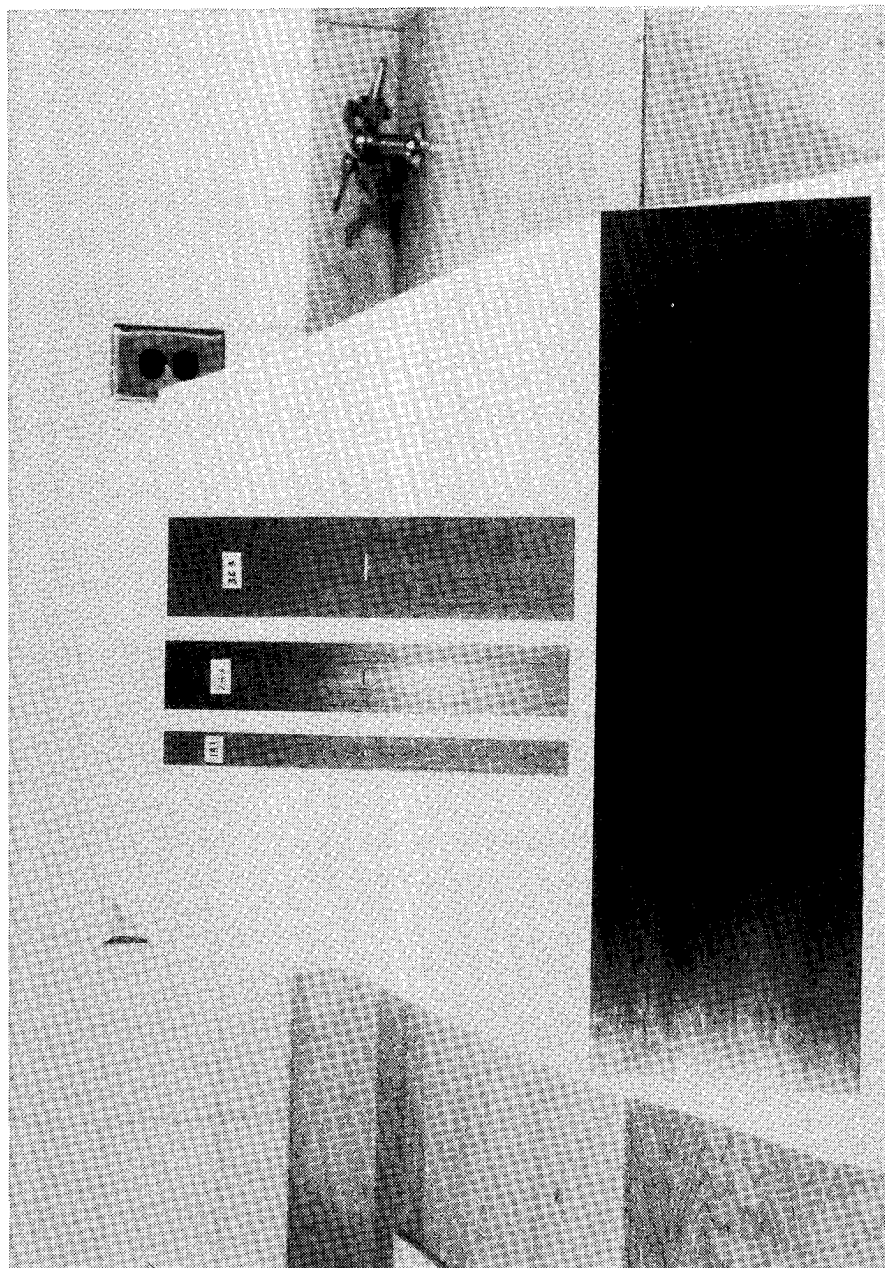
Figure 2. Representative coupon widths and graphite/epoxy sheet from which they are fabricated.

Two strain gages were placed on each coupon at a distance of 63.5 mm or 76.2 mm below the notch. The 76.2 mm location was used on narrow coupons so the strain gages would not interfere with the placement of the acoustic emission sensors. The strain gage locations were chosen to be approximately equidistant between the notch and the end grips to provide for measurement of remote strain while reducing the effect of the end grips. The gages were also placed at the approximate midpoint between the free edge and a line perpendicular to the tip of the notch. Finally, 25.4 mm doublers were bonded with epoxy to the ends of the coupons to provide a gripping surface and prevent crushing of the coupon by the mechanical grips. Figure (3) shows a sketch of a prepared coupon and Figure (4) shows the progression of coupon preparation.

Acoustic Emission Monitoring

The acoustic emission (AE) equipment used was the 3400 Acoustic Emission Analyzer manufactured by Physical Acoustics Corporation of Princeton, New Jersey. It utilized four independent channels with a separate parametric channel for real time data acquisition. Each of the four channels had a model R-15 piezoelectric transducer for detection of acoustic emissions. In addition, each channel had individual threshold voltage and amplification settings. The AE data was analyzed and stored on floppy disks as each test was run. The storage of all test data made post-analysis possible.

The four transducers were placed on the coupon as shown in Figure (5). The active sensors were located 63.5 mm directly above and below the notch and were responsible for detecting split initiation at the notch tip and split growth extending away from the notch. Any acoustic events arising from these failure modes would hit these sensors first

Aluminum Doubler

Fiber Direction

W

Notch

$\leftarrow 2a \rightarrow$

Strain Gages
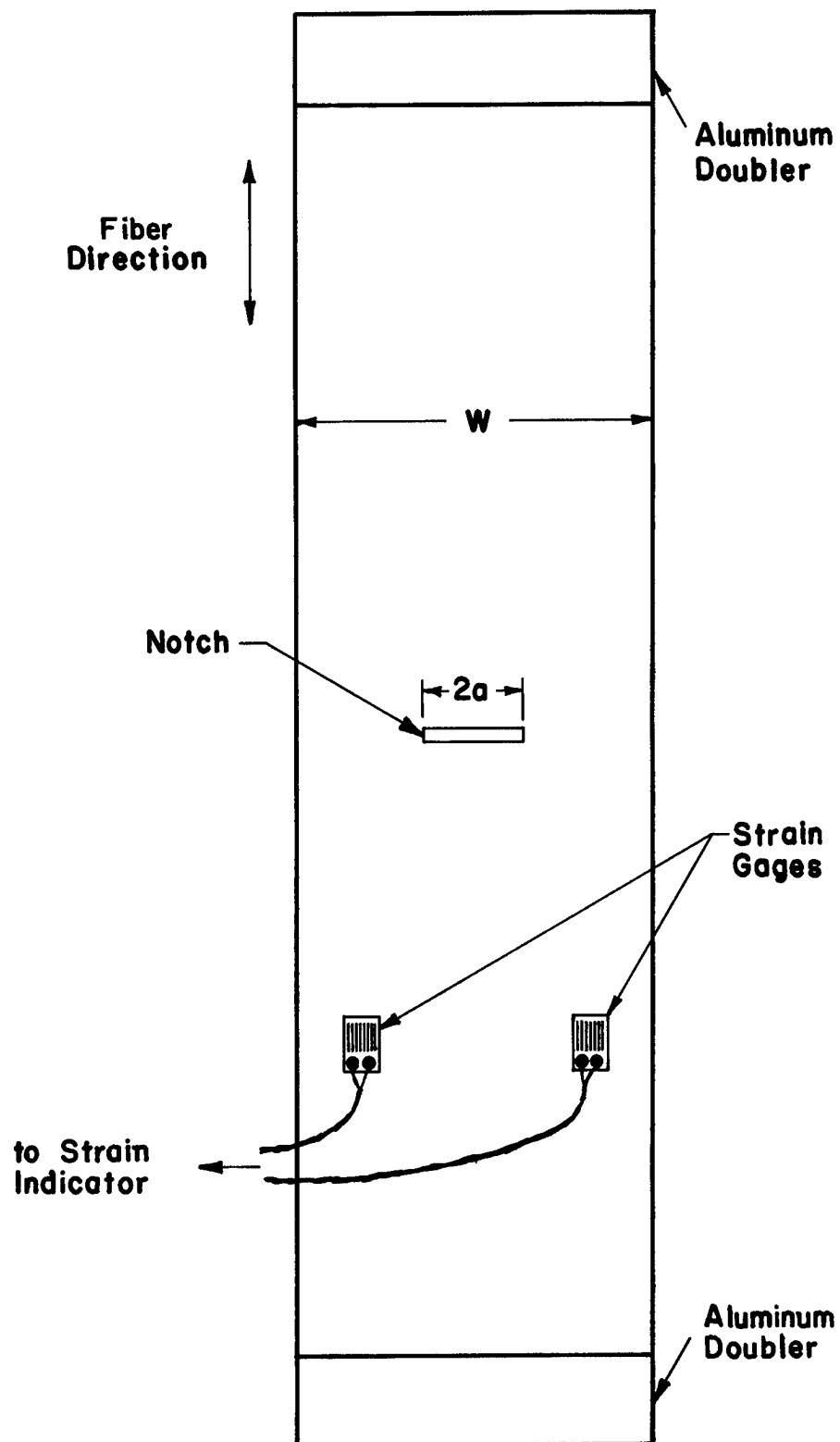
to Strain Indicator

Aluminum Doubler

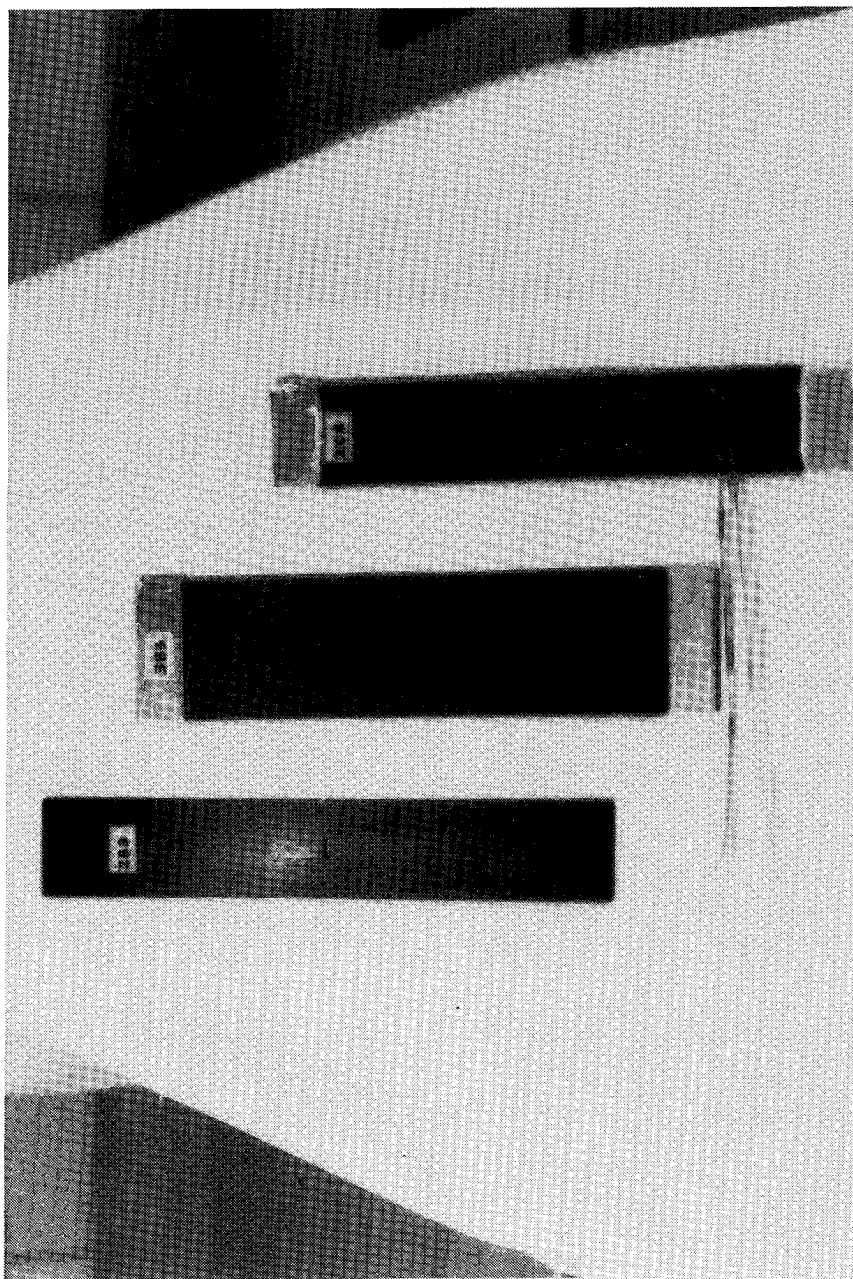Figure 3. Sketch of prepared coupon.

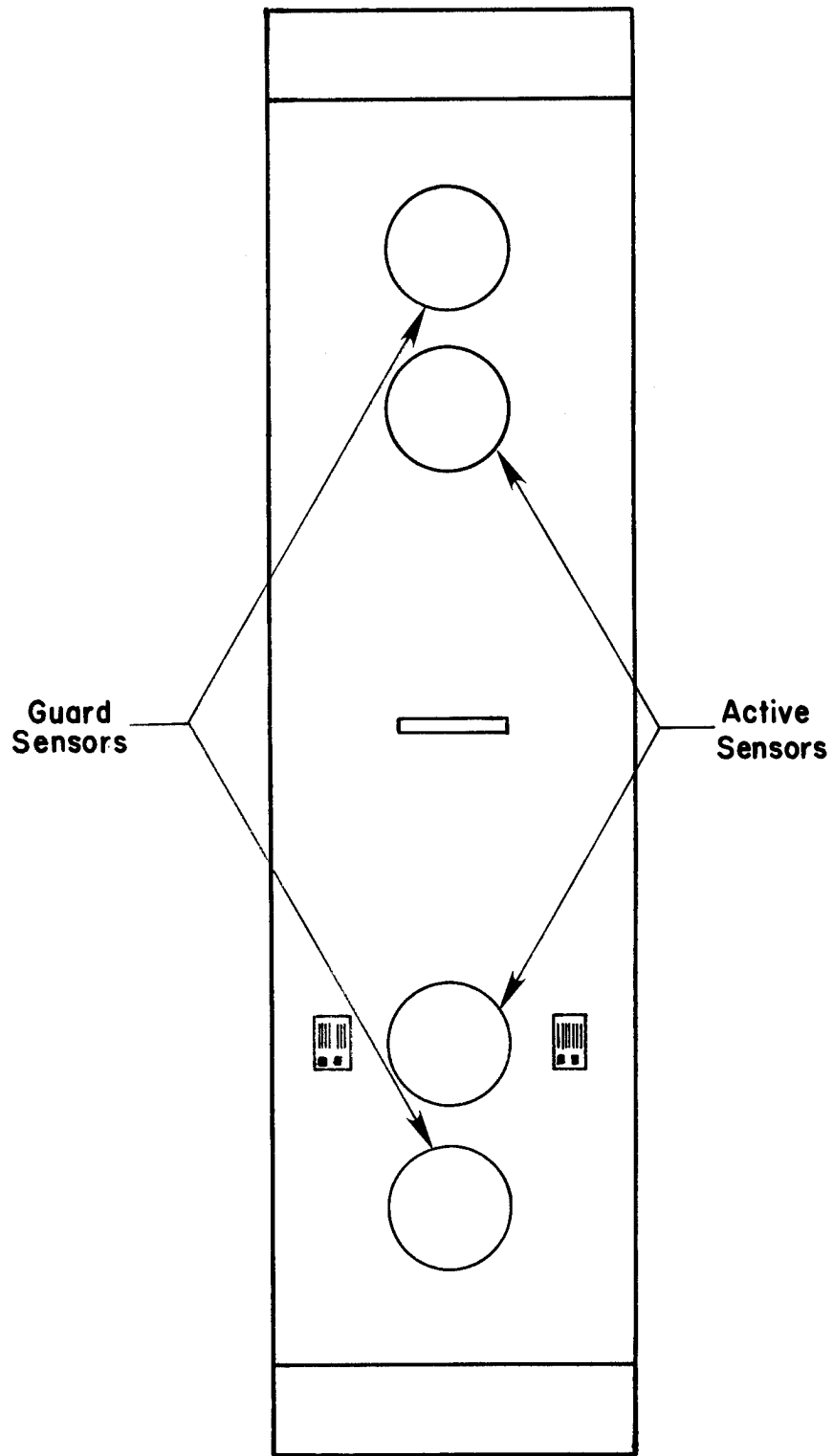Figure 4. Progression of coupon preparation.

Figure 5. Sketch of coupon showing the location of the acoustic
emission sensors.

and be recorded in the data set. The outer sensors, or guard sensors, were placed directly outside the active sensors. By placing them at this location, any events created in the coupon by testing machine vibration or mechanical gripping noise would hit these sensors first and be rejected. These events are rejected due to the sensors being designated as guard sensors in the initial test setup. Therefore, this setup enabled the machine and grip noise to be filtered out as the test was being run. Electrical noise was minimized by using shielded cables. All the sensors were attached to the coupon surface with high vacuum grease and held in place by rubber bands. The vacuum grease served as a coupling medium between the coupon surface and the ceramic plate of the transducers.

Results from several baseline tests on unnotched coupons and trial runs on notched coupons provided information on suitable threshold voltage and amplification settings for the AE analyzer. It was determined that a threshold voltage of 0.5 volts and 60 decibels of amplification would allow detection of all AE events of importance to this study (split initiation, split growth), while ignoring events of little or no consequence. The baseline tests showed that a reduction of threshold voltage by a factor of ten (from 1 volt to 0.1 volt) resulted in an increase in the number of events recorded by a factor of ten. The extra events consisted mostly of low energy events. In other words, the lower threshold accepted many more events, but little or no extra information on matrix splitting events. Using a threshold of 0.5 volts approximately doubled the number of events from the 1.0 volt case. This threshold value provided a low enough level to ensure that no event of importance would be filtered out while keeping the total number of

events down to a manageable level to be stored on disk. From the same reasoning, a 60 decibel amplification setting was chosen over a 40 or 80 decibel setting.

The baseline tests also indicated that more than 95 percent of all events recorded fell below a minimum limit on at least one of the four AE parameters: duration, counts, energy, and amplitude. Preliminary tests on notched coupons showed that an event that could be associated with a split in the matrix exceeded these minimum limits for all parameters. More than ten percent of the events from the notched coupons exceeded these limits. The low percentage of matrix split events in the baseline tests would be expected since only a small amount of matrix splitting occurs in the baseline coupons before the ultimate failure strain of the fibers is reached and the coupon fails catastrophically. The notched coupons localized the damage and caused the matrix splitting to occur when only a fraction of ultimate load was present. What this accomplished was the establishment of parameter limits that an event must exceed before it would be assumed to be due to split initiation or split growth.

The AE analyzer was used to detect split initiation by monitoring the energy level of the events as they occurred. Upon the detection of the first event of significant energy (greater than the minimum level), or the detection of ten cumulative events, the loading was stopped. Radiographs taken at this point usually indicated splits as small as one millimeter in length in one or two of the four possible directions. The wider notches would have longer initial splits and higher split energies. In only three of the 24 tests did the visibly identifiable split initiation event fall below any of the minimum parameter levels. After

split initiation, the AE analyzer was used to indicate split growth. A rapid rise in the event rate would indicate large split growth and enable the loading to be stopped and the amount of growth determined using X-rays with dye penetrant. In the same way, slow event rates indicated small, stable split growth and allowed the range of stable growth to be determined.

The AE analyzer was equipped with 100kHz-300kHz bandpass filters in the preamplifiers. From sample tests on graphite/epoxy and boron/aluminum, it was found that this frequency range would allow detection of the major events such as matrix splitting and fiber breaks. Since the frequency range was satisfactory and past work [24] has also shown this range to be of primary interest, no attempt was made to vary this filtering parameter.

Location calibrations were obtained before each test. This involved the input of a repeating pulse from a pulser/calibrator unit into the upper guard sensor so that this sensor could act as a controllable AE source. The AE analyzer would measure the time elapsed between a pulse hitting the upper active sensor to when it hit the lower active sensor. The average timing value, in microseconds, was stored as part of the test data and used to predict the location of the source of actual test events relative to the active sensors. For each event, the analyzer would note which sensor was hit first and the amount of time elapsed until the event hit the other sensor. Knowing the timing value from the calibration, which corresponded to an event traveling the full distance between sensors, the location of the event source could be predicted. For example, if both sensors were hit at essentially at the same time, the source location would be predicted as the midpoint between the sensors.

The AE analyzer also provided a method for continuous monitoring of the strain levels. The voltage output from the strain indicator was amplified and input to the AE analyzer through the separate parametric channel. Whenever an event was detected, the strain voltage was stored along with the other event data. The voltage-to-strain relationship had been determined by prior calibration, making it possible to calculate an approximate remote strain level present when each event occurred. This was particularly advantageous when determining the strain level at which the split initiation event occurred. Also, the strain level reached during each load increment could be verified by comparing the strain value recorded directly from the strain indicator to the maximum voltage found for the events that occurred during that load increment.

Radiographic Procedure

The procedure for taking radiographs of the coupons was modified from a technique used by Goree and Jones [15]. It involved the use of a portable, low level X-ray source to expose Polaroid Type 55 film. The X-ray source was a Model MTK 140 Be X-ray machine manufactured by the Philips Company of West Germany. The previous work by Goree and Jones provided starting points for current levels, voltage levels, exposure times, and film to focus distances (FFD). They point out that an X-ray of a graphite/epoxy coupon produces no distinct fiber pattern. In addition, the matrix splits do not show up on the radiograph. To make the splits visible, an X-ray enhancing penetrant had to be injected at the notch before each radiograph was taken. The penetrant was a solution of zinc iodide (60 grams) with isopropyl alcohol (10 ml), water (8 ml), and Kodak Photo-Flo 200 (3 ml). The solution was able to penetrate the matrix splits and flow both up and down the splits. The radiographs

would show the location of the penetrant as dark lines within the gray image of the coupon. From the radiographs, the split lengths could be measured directly. Figure (6) shows a representative radiograph of matrix splitting.

All radiographs were taken using a tube current of 5 mA and a 76 cm FFD. Initially, an exposure time of 2.2 minutes at 30 kV were used, but this was later modified to an exposure time of one minute at 40 kV. It was found that this combination of exposure time and voltage level provided good contrast between the splits and the coupon itself, while reducing the amount of time needed for the radiograph.

The radiographs also provided information on the crack opening displacement (COD) of the notch. The notch image would be examined under a stereo-microscope and magnified seven times. A scale divided into 0.1 mm increments was used to measure the opening of the notch. This method could only be used on radiographs taken up to the point of split initiation though, since subsequent radiographs were taken after the splits had grown and the load had been reduced to prevent creep in the matrix at the tip of the splits. With a reduced load, the radiograph would indicate a smaller COD than was actually present at the load level reached to produce that particular amount of matrix splitting. Therefore, the COD measured would not correspond to the actual value at full load or to the value for a notch at the reduced load with no matrix splitting.

Brittle Coating and Photographic Technique

The graphite/epoxy sheets used for this study had a smooth surface and a rough surface. The rough surface was sanded and used for strain gage attachment and AE sensor placement. The smooth side was cleaned
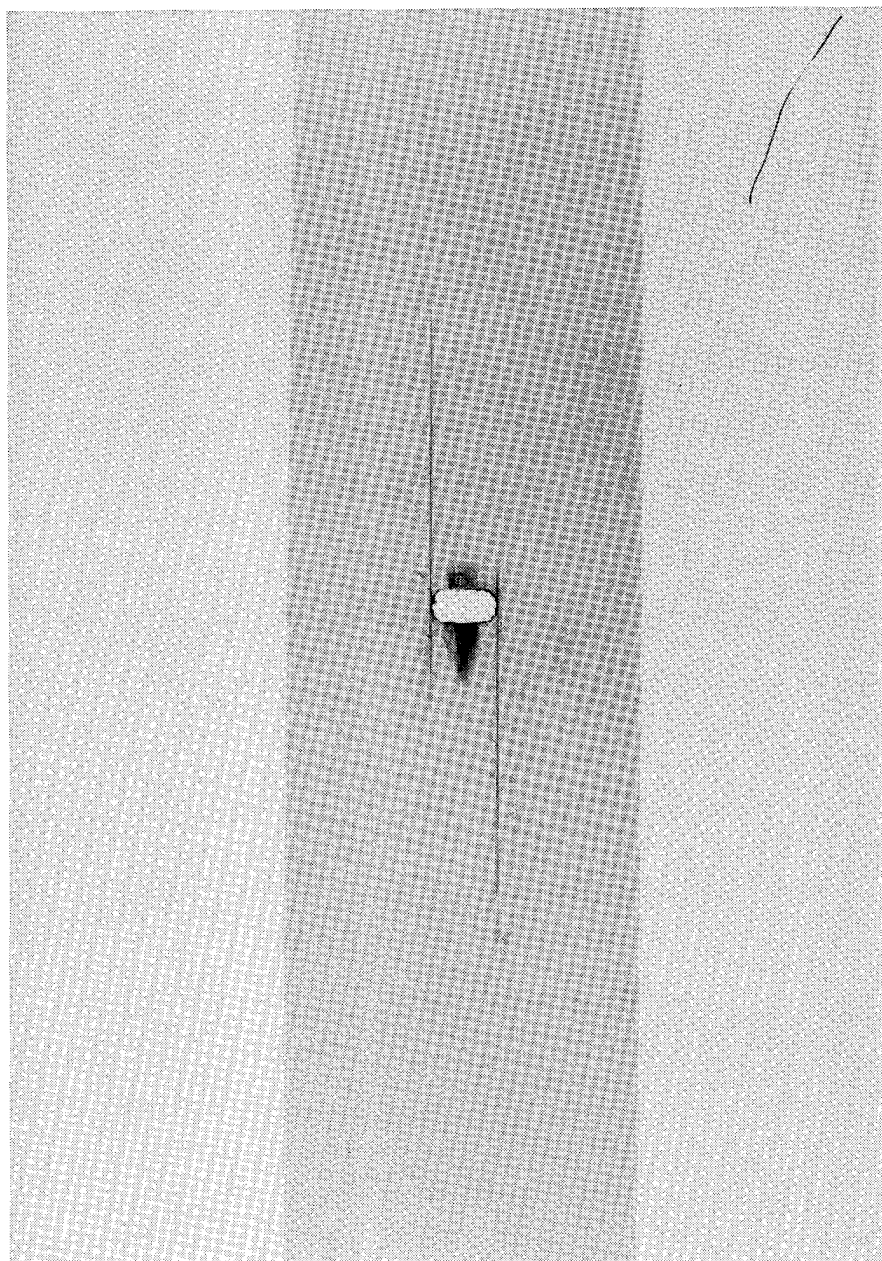
Figure 6. Typical radiograph showing matrix splitting.

and then coated with a brittle lacquer by a technique used by Goree and Jones. This involved applying up to twenty thin coats of lacquer with at least two minutes drying time between coats. The result was a clear, shiny finish on the black epoxy surface. On some coupons, a silver undercoat was applied first to see if it would improve the contrast between cracks in the lacquer and the underlying surface. The brittle lacquer used was Tenslac, manufactured by the Micro-Measurements Division of the Measurements Group, Raleigh, North Carolina.

During a test, the lacquer would crack when the underlying surface reached the threshold strain for the lacquer. Due to this behavior, the brittle coating provided a second method for measurement of matrix split length and a possible indication of matrix yielding at the split tip. The matrix splits would cause the lacquer to crack and allow direct measurement of the split length during the test. One drawback to this was that the lacquer would not give any noticeable indication of splits that were shorter than approximately 10 mm in length. Splits of this length or shorter had to be measured from radiographs. In most cases, both brittle coating and radiograph measurements were available and they provided a good method for verification of results. Also, there were instances when the radiographs would be inconclusive due to poor solution penetration or image contrast and the brittle coating measurements served as good backup measurements.

Photographs were taken of the brittle coating during each test for later detailed analysis of split lengths and yield zones. The coupon surface was illuminated with a tungsten light source. It was found that the angle of the light source to the coupon surface had no significant effect on the ability to detect brittle coating cracks due to matrix

splitting. In fact, the cracks due to matrix splitting were easily detected with room lighting alone. On the other hand, Goree and Jones found that an angle of 30 degrees from the surface normal greatly enhanced the ability to see cracks due to matrix yielding. Therefore, the 30 degree angle was used to improve the detection of matrix yielding behavior.

A 35 mm Nikon FM camera was used with a Vivitar zoom lens to allow for close up photographs of the coupon surface around the notch. The camera was mounted on a tripod to allow long shutter speeds to be used. To improve the depth of field, an f-stop of 8 was desired. For each photograph, the aperture was set to within one-half stop of 8 and the shutter speed adjusted to give the longest exposure time possible for the lighting conditions present at the time. The film used was Technical Pan Film 2415 (Estar-AH Base) from Kodak. A standard developing procedure was followed using Kodak D-19 developer. A previous study had shown that the D-19 developing process yielded a high contrast photograph with good resolution. Figure (7) shows a typical brittle coating photograph.

As mentioned previously, a silver undercoating was used on some coupons to see if the contrast was improved. It was found that the undercoating provided no significant improvement in the ability to detect cracks by direct visual inspection and actually reduced the contrast in the photographs. In fact, the brittle coating cracks were essentially undetectable in the photographs of undercoated coupons, but were easily measured from photographs of coupons with no undercoat. As with the radiographs, the negatives were examined under a stereo-microscope to measure the matrix split length and examine the lacquer for cracks due to yielding.
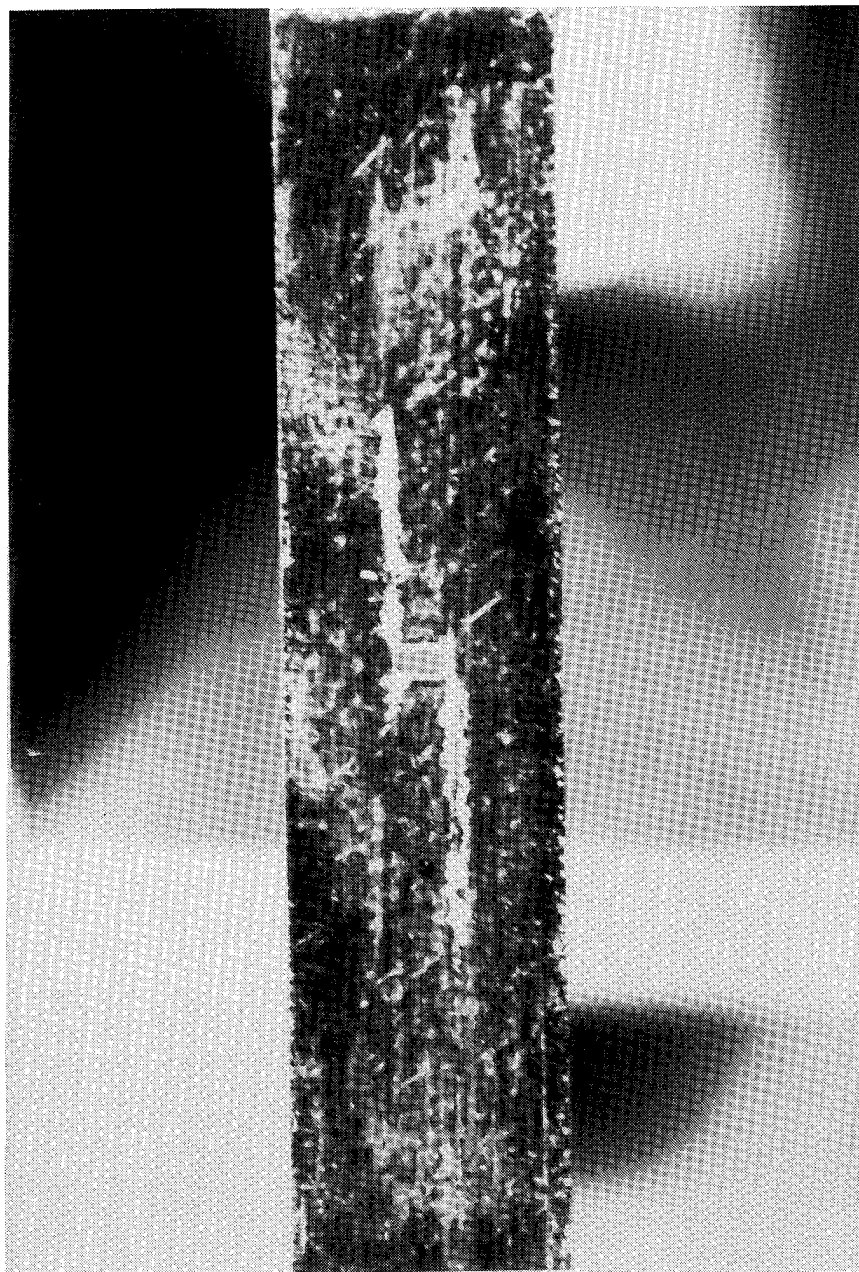
Figure 7. Typical brittle coating photograph.

General Testing Procedure

After the coupon was prepared and the brittle coating had dried for at least one day, it was ready for the tensile test. First, the four AE sensors were fixed in position with vacuum grease and rubber bands. Then the coupon was aligned in the Baldwin testing machine. Figure (8) shows a typical coupon setup with the X-ray film in position. The AE analyzer and disk storage were initialized and a location calibration was performed. After a baseline radiograph and photograph were taken, the loading could begin.

The loading sequence began by loading the coupon up to approximately 90 percent of the anticipated split initiation load. The rate of loading never exceeded 0.05 inches per minute. The AE sensors would be turned off while penetrant was injected at the notch. A radiograph was taken from which a COD value could be obtained. This radiograph also served to verify that no splits had initiated without the expected AE indications described earlier. The AE sensors were turned off to prevent the AE analyzer from recording events associated with handling of the coupon during penetrant injection or X-ray film attachment.

Next, the AE sensors would be turned back on and the loading continued until the AE data indicated that an event of sufficient energy to be a matrix split occurred. This nearly always occurred within the first ten events detected. The readings from the two strain gages and the load from the testing machine would be recorded and then the load would be dropped approximately 25 percent. The unloading was done to prevent creep from taking place in the matrix at the split tip. The AE sensors would record any events that occurred during the unloading. After unloading, the AE sensors were turned off and a radiograph taken.
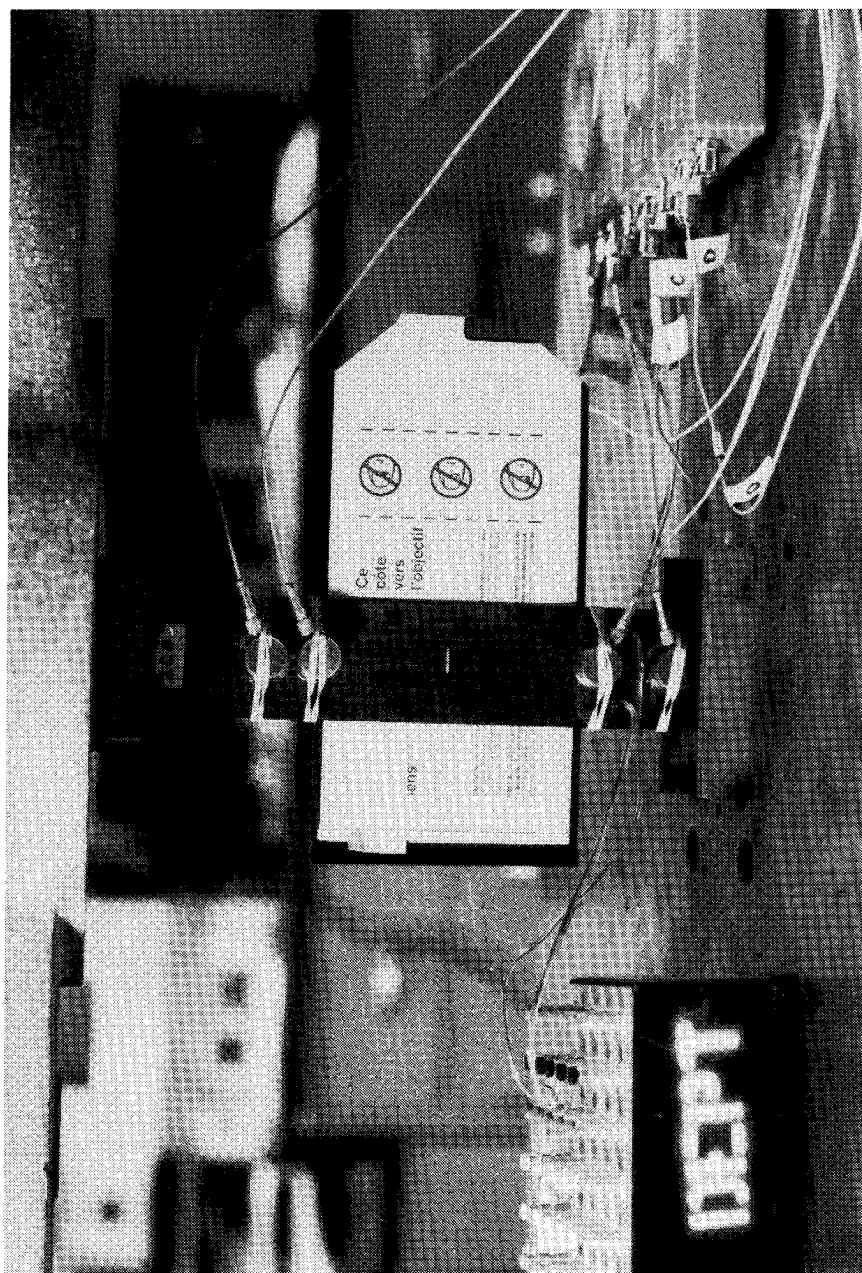
32

Figure 8. Closeup of coupon in the tensile test machine with X-ray film attached.

No photograph was taken unless there were visible cracks in the brittle coating.

After the radiograph verified the split initiation, the AE sensors were reactivated and the loading continued until an increase of approximately 100 microstrain over the previous peak level was reached or a rapid rise in the AE event rate was experienced. As before, the strains and load were recorded, the load was dropped approximately 25 percent, the AE sensors were turned off, a radiograph was taken, and a photograph was taken if necessary. This sequence was continued until all the splits had grown to at least 50 mm in length. An average of 13 radiographs and eight photographs were taken for each test. Figures (9) and (10) show the general test setup used.

It should be noted that the AE sensors were always on during any unloading or reloading of coupons. Of particular interest was the observation that a significant number of AE events did not occur during reloading until the previous peak strain was reached. This apparently supports the existence of the Kaiser effect. Also, it was stated that the load increments were based on a 100 microstrain increase or a rapid event rate increase. What was considered to be a rapid event rate increase varied from the beginning of the test to the end. During periods of slow split growth, a sudden jump of ten events was considered significant. As the load increased and the splits began to grow in larger steps, it was possible to record 100 to 200 events in a span of two to three seconds. Therefore, it was not possible to set a constant number of AE events that must be detected between load increments.
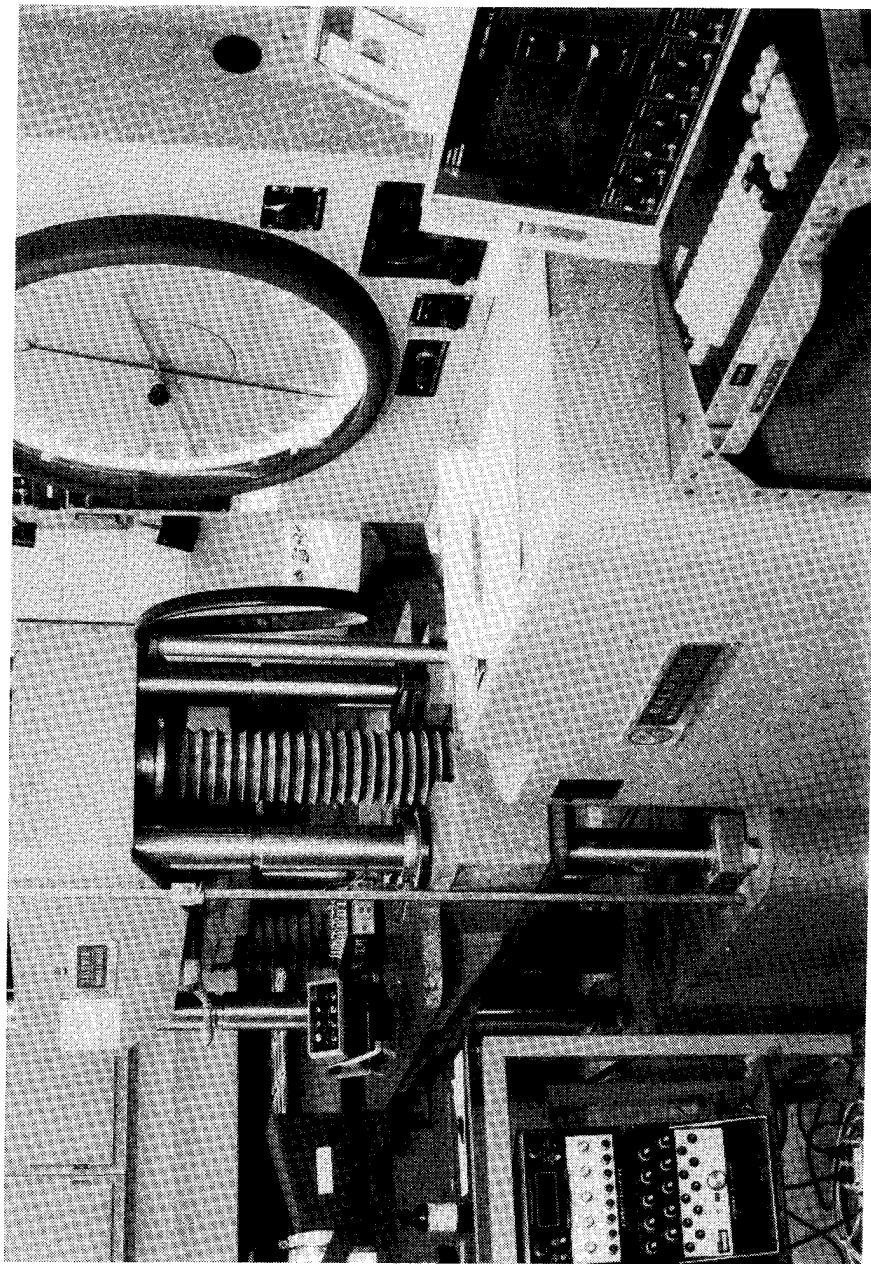
34

Figure 9. Typical test setup showing the X-ray unit, test machine, strain indicator, and AE display.
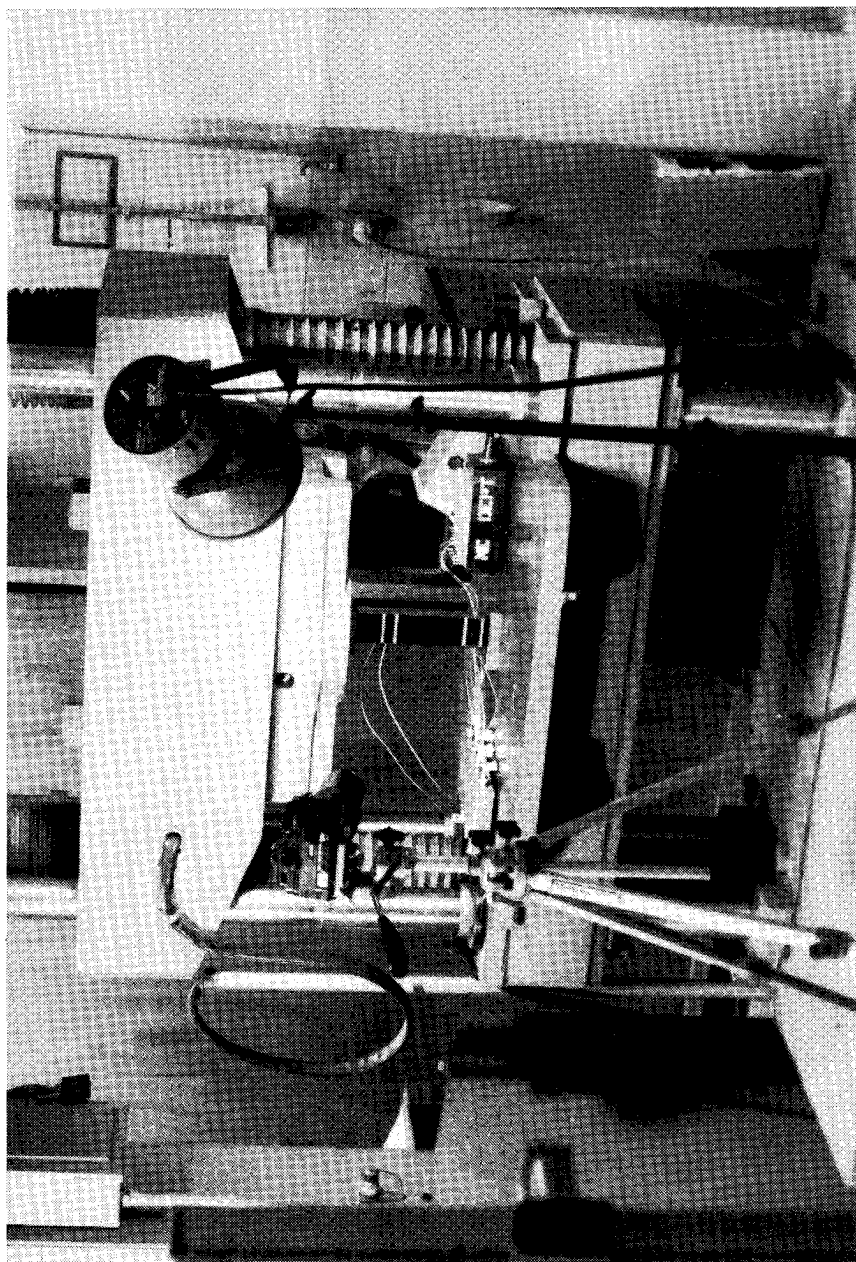
Figure 10. Test setup showing brittle coating photography.

CHAPTER III

ANALYSIS

Mathematical Model Description

The experimental program was designed to determine the actual frac-

ture behavior of unidirectional, notched graphite/epoxy laminates when

subjected to tensile loading. One of the primary objectives was to

examine how this behavior compared to the behavior predicted by the

shear-lag modeling analysis. The shear-lag approach involves the

assumption that load is transferred between adjacent fibers by shear

stresses. This shear stress will be directly proportional to the dif-

ference in axial displacements of the adjacent fibers and is independent

of transverse displacements. The particular model to be considered in

this study is based on this shear-lag stress transfer mechanism and has

been developed by Goree and Gross [10]. The model will be outlined here

so the fundamental assumptions can be pointed out for use in future com-

parisons between actual and predicted behavior.

Figure (11) shows the laminate as it is modeled. Due to symmetry,

only the first quadrant is necessary. It is modeled as a two-dimen-

sional region having a single row of parallel, identical, equally spaced

fibers with matrix material between the fibers. The laminate is consid-

ered to continue indefinitely in both directions. The damage consists

of an arbitrary number of broken fibers (notch), and matrix damage in

the form of yielding and splitting between the last broken fiber and the

first unbroken fiber. The fibers are assumed to support all the axial

load due to their high elastic modulus, while the matrix is assumed to

support shear stresses and transverse normal stresses. The free body diagram in Figure (12) shows the assumed stresses for a single fiber and the surrounding matrix.

It should be noted that this analysis is for a single ply, whereas the experimental study involved eight-ply laminates. As pointed out by Goree and Gross, any misalignment of the fibers between plies or within each ply itself could have a considerable influence on the stress state. Also affecting the stress state will be the minimum distance between fibers. As the minimum distance, d, decreases, the shear stress between fibers increases on the order of $1/\sqrt{d}$. Due to this effect, it was necessary to define a shear transfer distance, h, which could be chosen along with the matrix shear modulus, G_M, to account for the variations in the stress state. The G_M and h values need to be determined experimentally for the particular laminate being considered. The determination of these values (in the form of G_M/h) involves curve fitting of the analytical results to match the experimental results. The details of this will be discussed in the next section.

Returning to Figure (11), a special shear condition must be noted for the region between the last broken fiber and the first unbroken fiber. Defining L as the total longitudinal damage length, ℓ as the matrix split length, τ_0 as the matrix yield stress, and letting n=N denote the last broken fiber, the shear stress condition becomes

$$\tau\big|_{N+1} = -\tau_0 < y - \ell > , \tag{1}$$

where

$$< y - \ell > = 1, \quad y \geq \ell, \quad \text{and}$$
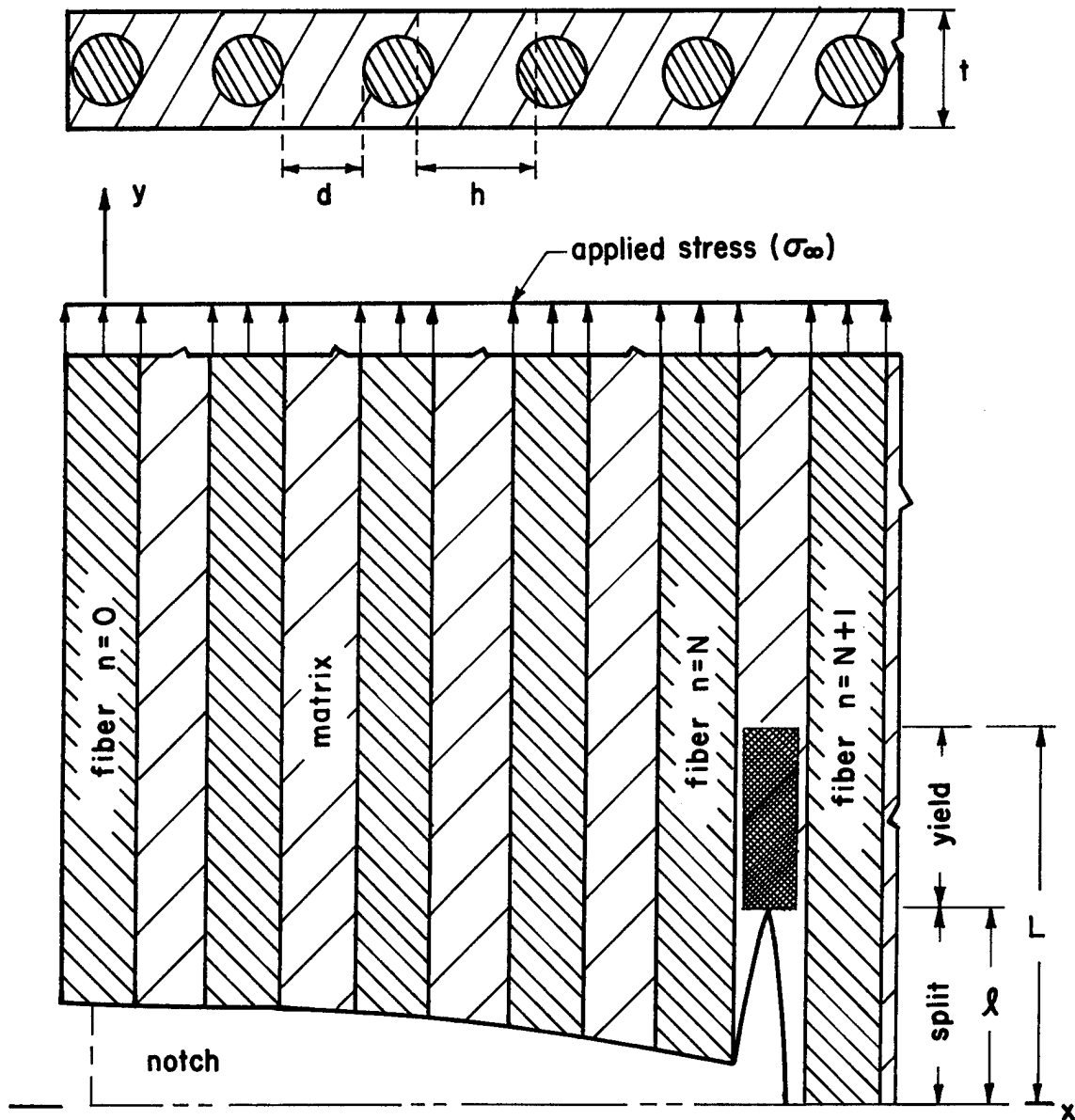$$< y - \ell > = 0, \quad y < \ell. \tag{2}$$

Figure 11. Two-dimensional unidirectional lamina with broken fibers, and longitudinal matrix splitting and yielding (first quadrant only).
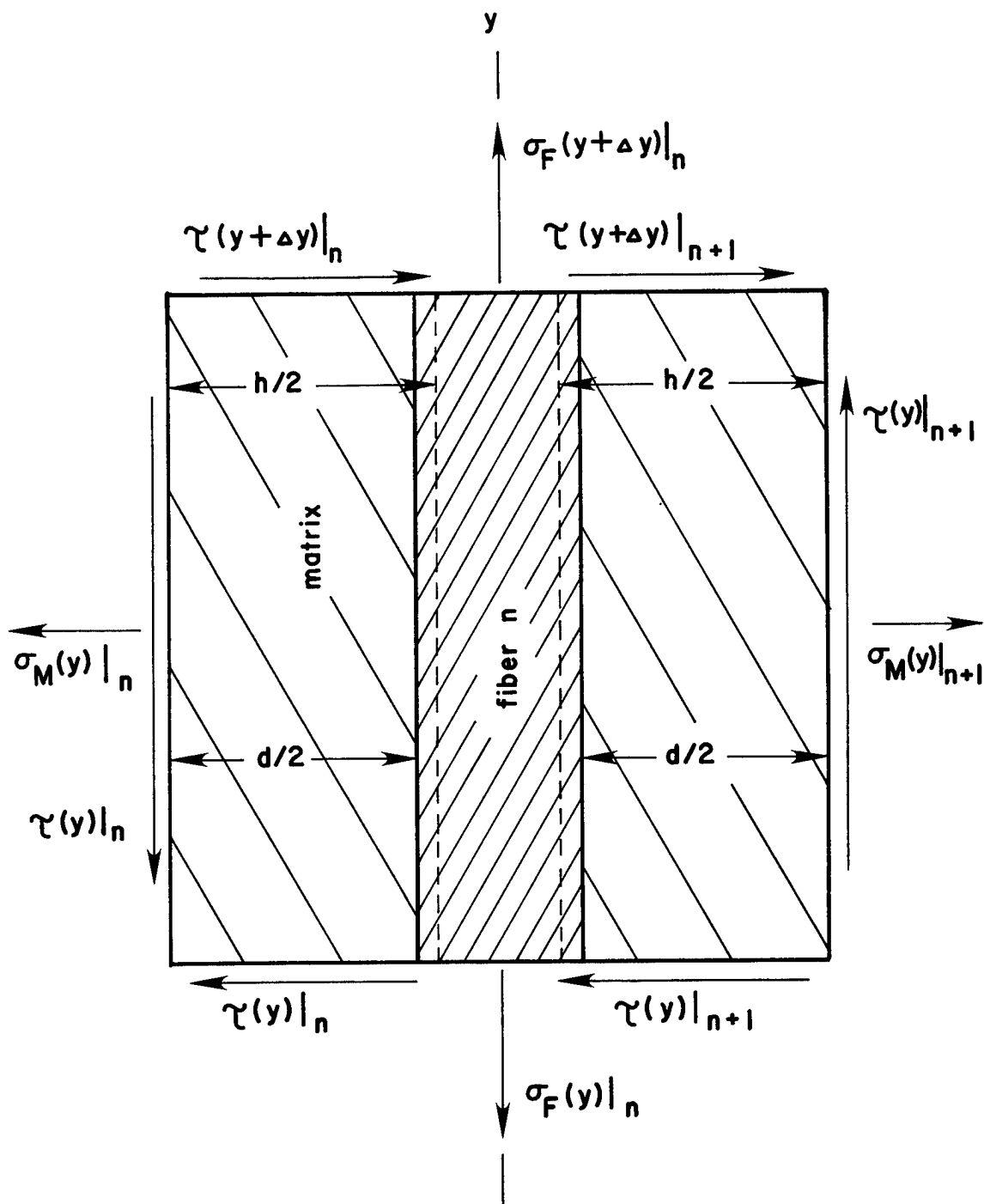
Figure 12. Free body diagram of a typical element.

40

This condition takes into account the assumption that matrix yielding occurs when the yield stress is reached and that this shear stress remains constant throughout the yield zone. In the split zone, no shear stress is present. Splitting is assumed to occur at a multiple of the yield strain, γ_o. The choice of the multiple is based on the type of matrix material being considered. A ductile matrix will be assumed to split at a larger multiple of its yield strain than a brittle matrix would.

From the conditions of static equilibrium, the equilibrium equations in the longitudinal and transverse directions for all fibers n, with the exception of N and N + 1 when $y \leq L$, are

$$\frac{A_F}{t} \left. \frac{d\sigma_F}{dy}\right|_n - \left. \tau \right|_{n+1} - \left. \tau \right|_n = 0 , \tag{3}$$

and

$$\left. \sigma_M \right|_{n+1} - \left. \sigma_M \right|_n + \frac{h}{2} \frac{d}{dy} \{ \left. \tau \right|_{n+1} + \left. \tau \right|_n \} = 0 . \tag{4}$$

For fiber N, $y \leq L$, Equation (1) is used and the equilibrium equations become

$$\frac{A_F}{t} \left. \frac{d\sigma_F}{dy}\right|_N - \tau_o < y - \ell > - \left. \tau \right|_N = 0 , \tag{5}$$

and

$$\left. \sigma_M \right|_{N+1} - \left. \sigma_M \right|_N + \frac{h}{2} \frac{d}{dy} \{ - \tau_o < y - \ell > + \left. \tau \right|_N \} = 0 . \tag{6}$$

For fiber N + 1, y ≤ L, Equation (1) is again used and the equilibrium equations become

$$\frac{A_F}{t} \left.\frac{d\sigma_F}{dy}\right|_{N+1} + \tau|_{N+1} + \tau_o < y - \ell > = 0 \ , \tag{7}$$

and

$$\sigma_M|_{N+2} - \sigma_M|_{N+1} + \frac{h}{2}\frac{d}{dy}\{\tau|_{N+2} - \tau_o < y - \ell >\} = 0 \ . \tag{8}$$

The equilibrium equations can be further simplified by using the following three stress-displacement relations:

$$\sigma_F|_n = E_F\frac{dv_n}{dy} \ , \tag{9}$$

$$\tau|_{n+1} = G_M(v_{n+1} - v_n)/h \ , \quad \text{and} \tag{10}$$

$$\sigma_M|_{n+1} = E_M(u_{n+1} - u_n)/h \ . \tag{11}$$

Equation (9) is a statement of Hooke's Law relating axial fiber stresses to the axial displacement of the fiber. Equation (10) is the basic shear-lag assumption, i.e. matrix shear stresses are assumed to be directly proportional to the relative displacement of adjacent fibers. G_M/h is the equivalent matrix shear stiffness and is experimentally determined. Equation (11) is a similar shear-lag assumption for transverse normal stresses in the matrix with E_M/h being the equivalent matrix transverse stiffness.

Use of these assumptions results in equilibrium equations with only axial displacements, v_n, and transverse displacements, u_n, as unknowns. In addition, the equation for axial equilibrium becomes uncoupled and may be solved independently. That is, the shear-lag model assumes that transverse displacements have no effect on the matrix shear stress. In this analysis, it is assumed that the matrix will fail in pure shear and thus depends only on the axial displacement of the fibers as given by the shear-lag mechanism. Therefore, the axial equilibrium equations are all that is necessary to determine the matrix stresses that will be used to predict matrix failure. For all fibers, except N and N+1 when $y \leq L$, the axial equilibrium equation becomes

$$\frac{E_F A_F h}{G_M t} \frac{d^2 v_n}{dy^2} + v_{n+1} - 2v_n + v_{n-1} = 0 \ . \tag{12}$$

For fiber N when $y \leq L$,

$$\frac{E_F A_F h}{G_M t} \frac{d^2 v_N}{dy^2} + v_{N-1} - v_N - \frac{h}{G_M} \tau_o < y - \ell > = 0 \ . \tag{13}$$

For fiber $N + 1$ when $y \leq L$,

$$\frac{E_F A_F h}{G_M t} \frac{d^2 v_{N+1}}{dy^2} + v_{N+2} - v_{N+1} + \frac{h}{G_M} \tau_o < y - \ell > = 0 \ . \tag{14}$$

By noting the coefficient of the second derivative terms, the following change of variables are suggested for non-dimensionalizing the equations. Let

$$\sigma_F \Big|_n = \sigma_\infty \bar{\sigma}_n = E_F \frac{d v_n}{dy} \ , \quad \text{and} \tag{15}$$

$$y = \left[\frac{E_F A_F h}{G_M t}\right]^{1/2} \eta \ . \tag{16}$$

From Equations (15) and (16), it can be shown that the normalized axial displacement, V_n is defined by

$$v_n = \sigma_\infty \left[\frac{A_F h}{E_F G_M t}\right]^{1/2} V_n = \frac{\tau_o h}{\bar{\tau}_o G_M} V_n \ , \tag{17}$$

and the normalized shear stress is defined by

$$\tau_o = \sigma_\infty \left[\frac{G_M A_F}{E_F ht}\right]^{1/2} \bar{\tau}_o \quad \text{or} \quad \sigma_\infty = \frac{\tau_o}{\bar{\tau}_o}\left[\frac{E_F ht}{G_M A_F}\right]^{1/2} = \frac{\tau_o}{\bar{\tau}_o} \ . \tag{18}$$

Algebraic manipulation then gives

$$\left.\begin{aligned}
\sigma_F\big|_n &= \sigma_\infty \frac{dV_n}{d\eta} = \frac{\tau_o}{\bar{\tau}_o}\left[\frac{E_F ht}{G_M A_F}\right]^{1/2} \frac{dV_n}{d\eta} \ , \\[2ex]
\tau_n &= \sigma_\infty \left[\frac{G_M A_F}{E_F ht}\right]^{1/2}\{V_n - V_{n-1}\} = \frac{\tau_o}{\bar{\tau}_o}\{V_n - V_{n-1}\} \ , \\[2ex]
L &= \left[\frac{E_F A_F h}{G_M t}\right]^{1/2}\alpha, \quad \text{and} \quad \ell = \left[\frac{E_F A_F h}{G_M t}\right]^{1/2}\beta \ .
\end{aligned}\right\} \tag{19}$$

In these equations, η, $\bar{\sigma}_n$, V_n, $\bar{\tau}_o$, α, and β are non-dimensional, while E_F, A_F, t, L, and ℓ are taken as actual values for the fiber modulus, fiber cross-sectional area, lamina thickness, damage length, and split length respectively.

The resulting non-dimensional equations are: For all fibers, except N and N + 1 when $\eta \leq \alpha$,

44

$$\frac{d^2V_n}{d\eta^2} + V_{n+1} - 2V_n + V_{n-1} = 0 \ , \tag{20}$$

for fiber N when $\eta \leq \alpha$,

$$\frac{d^2V_N}{d\eta^2} + V_{N+1} - 2V_N + V_{N-1} = - f(\eta) \ , \tag{21}$$

and for fiber N + 1 when $\eta \leq \alpha$,

$$\frac{d^2V_{N+1}}{d\eta^2} + V_{N+2} - 2V_{N+1} + V_N = f(\eta) \ . \tag{22}$$

The new unknown function, $f(\eta)$, is defined as

$$f(\eta) = V_N - V_{N+1} - \bar{\tau}_o < \eta - \beta > \ , \qquad \eta < \alpha \ , \quad \text{and}$$

$$f(\eta) = 0 \ , \qquad\qquad\qquad\qquad \eta \geq \alpha \ . \tag{23}$$

These differential-difference equations may be reduced to differen-
tial equations by introducing the even-valued transform,

$$\bar{V}(\eta,\theta) = V_0(\eta)/2 + \sum_{n=1}^{\infty} V_n(\eta) \cos(n\theta) \ , \tag{24}$$

from which

$$V_n(\eta) = \frac{2}{\pi} \int_0^{\pi} \bar{V}(\eta,\theta) \cos(n\theta) d\theta , \tag{25}$$

and the three equations become

$$\frac{2}{\pi} \int_0^{\pi} \left\{ \frac{d^2\bar{V}}{d\eta^2} - 2[1 - \cos(\theta)]\bar{V} \right\} \cos(n\theta) d\theta = 0 \ , \tag{26}$$

$$\frac{2}{\pi} \int_0^\pi \left\{ \frac{d^2\bar{V}}{d\eta^2} - 2[1 - \cos(\theta)]\bar{V} \right\} \cos(n\theta) d\theta = -f(\eta), \quad \text{and} \qquad (27)$$

$$\frac{2}{\pi} \int_0^\pi \left\{ \frac{d^2\bar{V}}{d\eta^2} - 2[1 - \cos(\theta)]\bar{V} \right\} \cos(n\theta) d\theta = f(\eta) . \qquad (28)$$

It should be noted that the left hand sides of the above functions are identical. Now, using the orthogonality of circular functions, the three equations may be written as one equation valid for all values of n and η as

$$\frac{2}{\pi} \int_0^\pi \left\{ \frac{d^2\bar{V}}{d\eta^2} - 2[1 - \cos(\theta)]\bar{V} \right\} \cos(n\theta) d\theta = \frac{2}{\pi} \, . X$$

$$< \alpha - \eta > \int_0^\pi f(\eta) \{\cos[(N+1)\theta] - \cos(N\theta)\} \cos(n\theta) d\theta . \qquad (29)$$

This equation is of the form

$$\frac{2}{\pi} \int_0^\pi F(\eta, \theta) \cos(n\theta) d\theta = 0 \qquad \text{for all } \eta \text{ and } n.$$

Noting the definition of $V(\eta, \theta)$ in Equations (24) and (25), it is seen that the function $F(\eta, \theta)$ is even-valued in θ and therefore, if the integrand is to vanish for all η, the function $F(\eta, \theta)$ must be zero. The single equation specifying $V(\eta, \theta)$ is then

$$\frac{d^2\bar{V}}{d\eta^2} - \delta^2\bar{V} = - < \alpha - \eta > D^2 f(\eta) , \qquad (30)$$

where

$$\delta^2 = 2[1 - \cos(\theta)] = 4 \sin^2(\theta/2), \quad \text{and}$$

$$D^2 = \cos(N\theta) - \cos[(N+1)\theta].$$

Goree and Gross point out that it is possible for the irregular boundary condition, Equation (1), of specified stress over a finite length, not coincident with either coordinate axis to be accounted for exactly and that the problem reduces to one differential equation which must satisfy boundary conditions along coordinate axes only. The ability to do so is largely due to the assumed failure criterion where matrix shear stresses are purely dependent on axial displacements. Inclusion of transverse displacements in the shear stress equation would couple the axial and transverse equilibrium equations and yield a more complicated set of differential equations.

For the problem of a stress-free notch surface in a coupon loaded with a uniform axial stress, superposition is used to separate the problem into two cases with boundary conditions that can be solved. The differential equation (30) will be solved using vanishing stresses and displacements at infinity and uniform compression on the notch surface as boundary conditions. This solution will then be added to the results from the problem of uniform axial stress and no broken fibers (no notch) to obtain the complete solution. Figure (13) shows the superposition pictorially.

The boundary conditions for the problem of vanishing displacements and stresses and compression on the crack surface are

$$V_n = 0 \quad \text{as} \quad \eta \to \infty , \tag{31}$$

$$\frac{dV_n}{d\eta} = 0 \quad \text{as} \quad \eta \to \infty , \quad \text{and} \tag{32}$$

$$V_n = 0 \quad \text{for} \quad \eta = 0 , \tag{33}$$
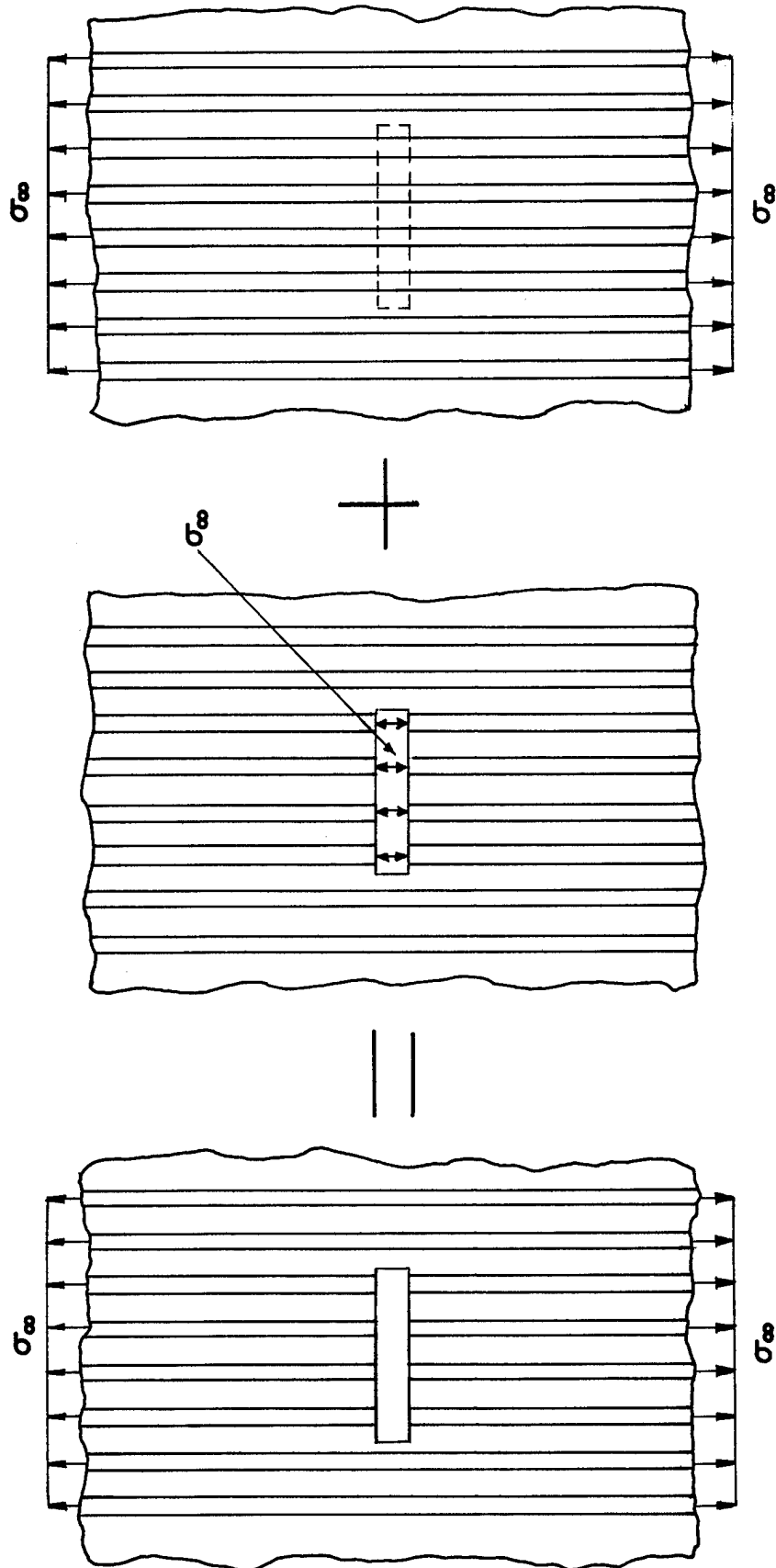
for unbroken fibers, and

Figure 13. Diagram of superposition used to solve for the problem of a stress free crack with uniform axial tension.

48

$$\frac{dV_n}{d\eta} = \bar{\sigma}_n = -1 \ , \tag{34}$$

for broken fibers (n=0 to n=N).

The complete solution satisfying vanishing stresses and displacements at infinity is

$$\bar{V}(\eta,\theta) = A(\theta) \ e^{-\delta\eta} + \frac{D^2}{\delta} \int_\eta^\alpha \sinh[\delta(\eta-t)] < \alpha - \eta > f(t)\,dt, \tag{35}$$

where the unknown functions are $A(\theta)$ and $f(t)$. The remaining two boundary conditions give

$$\frac{dV_n(0)}{d\eta} = \frac{2}{\pi} \int_0^\pi \{-\delta A(\theta) + D^2 \int_0^\alpha \cosh(\delta t)f(t)\,dt\}\cos(n\theta)\,d\theta = -1 \ , \tag{36}$$

for all broken fibers, and

$$V_n(0) = \frac{2}{\pi} \int_0^\pi \{A(\theta) - \frac{D^2}{\delta} \int_0^\alpha \sinh(\delta t)f(t)\,dt\}\cos(n\theta)\,d\theta = 0, \tag{37}$$

for all unbroken fibers. Equation (37) is solved exactly by taking

$$A(\theta) - \frac{D^2}{\delta} \int_0^\alpha \sinh(\delta t)f(t)\,dt = \sum_{m=0}^N B_m \cos(m\theta) \ , \tag{38}$$

where m is the broken fiber index and the B_m are constants. There are precisely as many constants B_m as there are broken fibers.

Using Equation (38) in Equation (36), $A(\theta)$ may be eliminated and Equation (36) gives a system of N+1 algebraic equations for the N+1 constants B_m in terms of $f(\eta)$ which is, as yet, unknown. For longitudinal

matrix damage, Equation (36) must be supplemented by the condition that

$$f(\eta) = g(\eta) - \bar{\tau}_o < \eta - \beta > , \quad \eta < \alpha ,$$ (39)

where

$$g(\eta) = V_N - V_{N+1} .$$

and, since $f(\alpha)=0$ from Equation (23),

$$g(\alpha) = \bar{\tau}_o .$$ (40)

The constants B_m and the function $g(\eta)$ are specified by requiring that Equations (36), (39), and (40) be satisfied. Using Equation (35), and the relation between $V(\eta,\theta)$ and $V_n(\eta)$, the axial displacement of any fiber for all values of η may be expressed as

$$V_n(\eta) = \frac{2}{\pi} \int_0^\pi e^{-\delta\eta} \sum_{m=0}^N B_m \cos(m\theta)\cos(n\theta)\,d\theta$$

$$+ \frac{1}{2} \int_0^\alpha f(t) \{ C_n(|t-\eta|) - C_n(t+\eta) \}\,dt ,$$ (41)

where

$$C_n(\xi) = \frac{2}{\pi} \int_0^\pi \frac{D^2}{\delta} e^{-\delta\xi} \cos(n\theta)\,d\theta .$$

Equation (36) then becomes

$$\frac{2}{\pi} \int_0^\pi \left\{ -\delta \sum_{m=0}^N B_m \cos(m\theta) + D^2 \int_0^\alpha e^{-\delta t} g(t)\,dt \right.$$

$$\left. - D^2 \bar{\tau}_o \int_\beta^\alpha e^{-\delta t}\,dt \right\} \cos(n\theta)\,d\theta = -1 ,$$ (42)

for broken fibers, and Equation (39) along with (41) gives, for $\eta \leq \alpha$,

$$g(\eta) = \frac{2}{\pi} \int_0^\pi e^{-\delta\eta} \sum_{m=0}^N B_m \cos(m\theta) \{\cos(n\theta)$$

$$- \cos[(N+1)\theta]\} d\theta$$

$$+ \frac{1}{2} \int_0^\alpha g(t) \{C_N(|t-\eta|) - C_N(t+\eta) - C_{N+1}(|t-\eta|)$$

$$+ C_{N+1}(t+\eta)\} dt$$

$$- \frac{\bar{\tau}_o}{2} \int_\beta^\alpha \{C_N(|t-\eta|) - C_N(t+\eta) - C_{N+1}(|t-\eta|)$$

$$+ C_{N+1}(t+\eta)\} dt = V_n - V_{n+1}, \qquad (43)$$

which is a Fredholm integral of the second kind. The last condition that must be satisfied is the condition of Equation (40).

It would be desirable to use the above equations to solve for the matrix damage zones, α and β, for a given applied stress, σ_∞, and number of broken fibers, N. Also, the yielding and splitting conditions for the matrix must be given. Since α and β are integral limits, this is not convenient mathematically. Instead, the damage zones and the number of broken fibers are specified and the applied stress required to produce these conditions is computed.

The computer solution involved solving Equations (40), (42), and (43) simultaneously for the unknown B_m, $g(\eta)$, and $\bar{\tau}_o$. The $g(\eta)$ function was approximated by a Gauss quadrature scheme with k quadrature points. Therefore, the unknowns consisted of N+1 Fourier coefficients (B_m), the

value of the function $g(\eta)$ at k discrete points, and $\bar{\tau}_o$. Once these values had been determined, fiber displacements and stresses could be found from Equation (41). After superposition of the uniform axial stress problem, the final non-dimensional results were obtained. In turn, Equations (17), (18), and (19) could then be used with the known fiber and matrix properties to determine the predicted values for the fracture behavior of the particular laminate.

Determination of Material Properties

As mentioned in the previous section, G_M/h, the equivalent matrix shear stiffness, and τ_o, the matrix yield stress, are determined by curve fitting the analytical results to match the experimental results. They are matched by forcing the applied load, the COD, and the matrix split length to agree at one point. The specifics of the matching process will be discussed later in this section. This point matching was done for only one notch width since it was assumed that G_M/h and τ_o are material properties and would be the same for all coupons. Therefore, the values obtained by matching one point for one notch width would be used to dimensionalize the computer results for all split lengths and all notch widths.

The curve fitting was accomplished by matching the predicted COD and remote stress values at split initiation to the actual values obtained experimentally. For this study, it was assumed that the elastic-perfectly plastic matrix had no yield zone at the tip of the split. In other words, the yield strain was the same as the splitting strain and all longitudinal matrix damage was in the form of splitting ($\ell=L$). Since epoxy is a brittle material, this was a reasonable assumption.

From Equation (18), it can be seen that

$$\sigma_\infty = \frac{\tau_o}{\bar{\tau}_o} \left[\left(\frac{E_F t}{A_F} \right) \left(\frac{h}{G_M} \right) \right]^{1/2} , \qquad (44)$$

and Equation (17), for fiber 0 at $\eta = 0$, becomes

$$v_o(0) = (\tau_o) \left(\frac{V_o(0)}{\bar{\tau}_o} \right) \left(\frac{h}{G_M} \right) , \qquad (45)$$

where $v_o(0)$ is the COD for the center fiber. These are expressions for the remote stress and COD in terms of known fiber and laminate proper-ties (E_F, A_F, t), non-dimensional values from the analytical results ($\bar{\tau}_o$, $V_o(0)$), and the parameters to be determined (G_M/h, τ_o). The remote stress and COD are known experimental values for a particular notch width at the point of split initiation. For the same notch width, the $\bar{\tau}_o$ and $V_o(0)$ values for split initiation are determined by computer solution. Now, the G_M/h and τ_o values are varied until the σ_∞ and $v_o(0)$ values from Equations (44) and (45) agree with the experimental values.

For this study, the fiber and laminate properties of the gra-phite/epoxy coupons were,

$E_F = 256.5 \times 10^9$ Pa $(37.2 \times 10^6$ psi),

$A_F = 1.40 \times 10^{-8}$ m² $(2.17 \times 10^{-5}$ in²),

$t = 0.159$ mm $(0.00625$ in), and

$\sigma_{ult} = 1.17 \times 10^9$ Pa $(169.7 \times 10^3$ psi).

The fiber modulus and ultimate strength were determined experimentally by testing unnotched coupons. The thickness, t, is for a single ply.

The experimental remote stress at split initiation and COD value were chosen from tests run on coupons with a 3.175 mm notch (19 broken fibers). These values were

σ_∞ = 225 MPa, and

COD = 0.030 mm.

The computer solution was matched to these values and the equivalent matrix shear stiffness and matrix yield stress were found to be

G_M/h = 7.347 $\times$ 10^{12} N/m^3 (27.1 x 10^6 lb/in^3), and

τ_0 = 4.336 $\times$ 10^7 N/m^2 (69289 psi)

Figure (14) shows the resulting remote stress versus COD curves using these determined values. The analytical and experimental curves agree up to the point of split initiation, as expected, but show large disagreement after this point. This is due to the model predicting a much more rapid rate of split growth, and therefore, COD increase, than was actually observed experimentally. As for predicting split initiation stress levels, the model worked very well for all notch widths. This will be discussed in more detail in the next chapter.

It was pointed out earlier that the G_M/h factor can not be obtained directly from the matrix shear modulus and fiber spacing. It was previously noted that the matrix shear stress is strongly dependent on fiber spacing and that the G_m and h parameters would be combined and used to account for the variations in the stress state. Even so, a value for the shear modulus obtained from the G_M/h factor should be of the same

order of magnitude as the actual shear modulus. If h is taken to be the assumed fiber centerline spacing of 0.178 mm, then a shear modulus of

$$G_M = 1.308 \text{ GPa} \quad (189.7 \text{ kpsi})$$

is calculated. This appears to be a reasonable value. Likewise, the matrix yield stress value is of the same order of magnitude as an actual value for brittle epoxies.
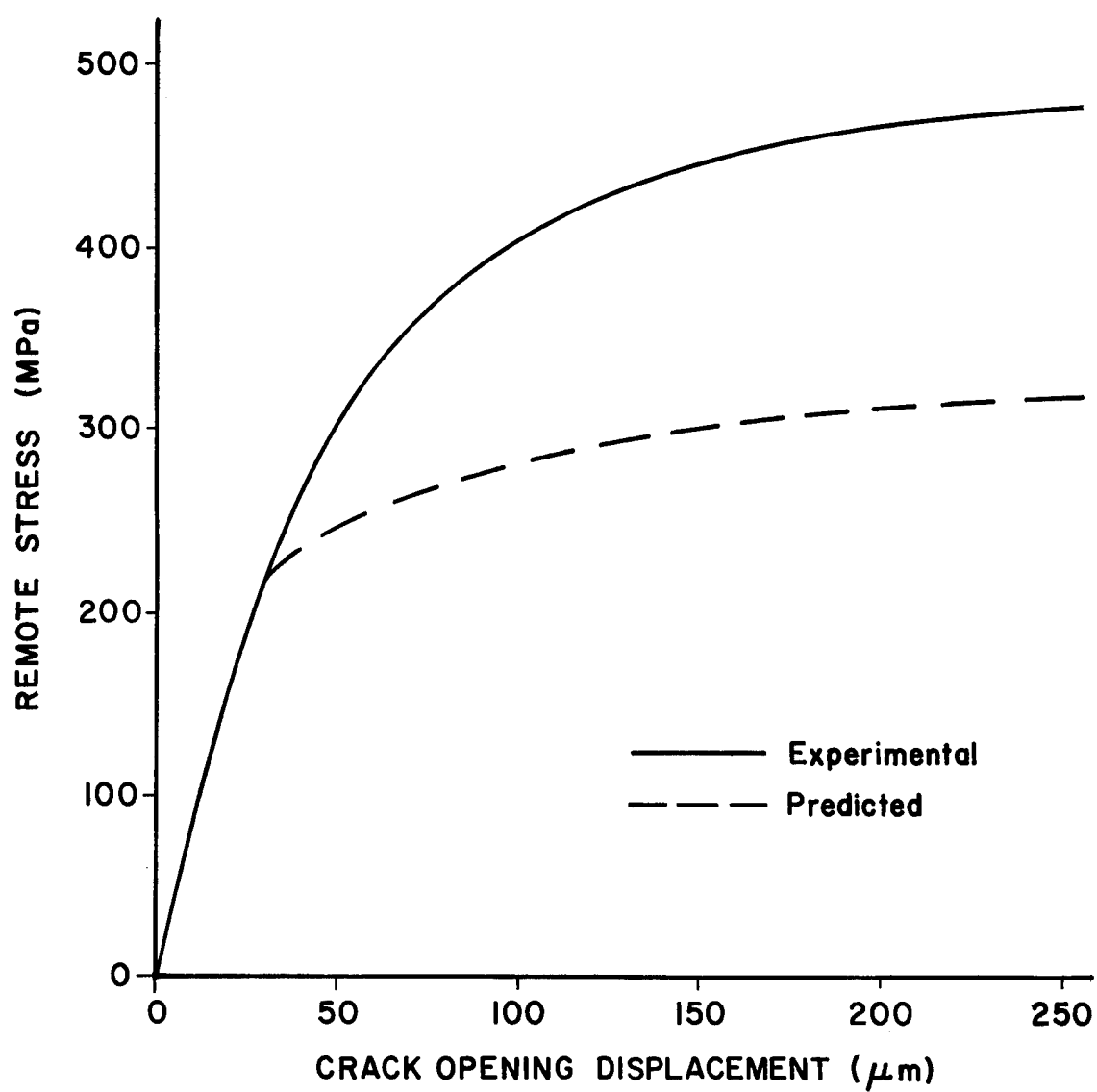
Figure 14. Remote stress versus COD curves for 19 broken fibers: comparison of analytical and experimental results.

CHAPTER IV

RESULTS AND DISCUSSION

Damage Growth Sequence

It has been stated that the main objective of this study was to determine the fracture behavior of damaged graphite/epoxy laminates and compare it to the behavior predicted by the shear-lag analysis. For unidirectional graphite/epoxy laminates with a center notch perpendicular to the fiber direction, the fracture behavior consisted of matrix splitting between the last broken fiber and the first unbroken fiber. Four splits were formed (two at each notch tip) and grew as the load was increased. AE monitoring was used to detect the first split initiation and radiography and brittle coating techniques were used to monitor the subsequent split growth. Before discussing the details of the results, a typical damage growth sequence will be presented in the form of a series of radiographs and brittle coating photographs. Since all coupons exhibited the same behavior, a representative test was chosen to serve as an example. The test chosen was for a 50.8 mm wide coupon with a 6.35 mm notch (37 broken fibers).

Figures (15) and (16) show the baseline radiograph and brittle coating photograph respectively. Dye penetrant solution has been injected at the notch. The edges of the notch, as well as some damage to the laminate caused by cutting the notch appear darker than the surrounding area. This damage above and below the notch is located in a non-critical area and will not affect the fracture behavior. Using a stereo microscope, the initial notch opening at the center of the notch

was measured and found to be 2.32 mm. On subsequent radiographs, this opening was measured and the increase from the initial opening was the COD.

From the AE, split initiation was detected after eight events. The radiograph of Figure (17) reveals the existence of small splits in the bottom right and top left directions. Both splits are less than 2 mm in length. Figure (18) shows that the brittle coating was unable to give a measurable indication of these splits. The splits had initiated at 176 MN/m^2 (15 percent of unnotched ultimate stress), but the radiograph was taken after the load had been reduced to 164 MN/m^2 (14 percent of ultimate) to prevent creep at the split tips.

Figure (19) shows the damage due to a peak stress of 218 MN/m^2 (18.6 percent of ultimate). All four splits have begun to grow, but are still less than 3 mm in length. As Figure (20) shows, the brittle coating still gives no evidence that splitting has occurred. Again, the damage corresponds to the peak stress level while the pictures were taken at a reduced load. This will be the case for all the subsequent pictures. As pointed out in the previous chapter, the COD values are no longer valid at this stage due to the reduced load combined with the damage caused by a higher stress level.

Figures (21) and (22) show the damage due to a peak stress of 248 MN/m^2 (21.2 percent of ultimate). The brittle coating now reveals the existence of the splits, but it indicates split lengths that are less than the actual lengths found from the radiograph. The brittle coating does not begin to give an accurate indication of the split lengths until they grow to approximately 7 to 15 mm as shown in Figures (23) and (24). These figures show the damage caused by a peak stress of 270 MN/m^2 (23.1 percent of ultimate).

Figures (25) through (30) show the damage at successive stress levels. The final split lengths shown range from 34 to 48 mm. It should be noted that none of the brittle coating photographs give a noticeable indication of matrix yield zones ahead of the split tips. A more sensitive measurement technique might provide more conclusive evidence as to the existence and size of yield zones, but it is sufficient for this study to assume that no yield zone exists.

General Results

A general damage sequence typical of all tests has been discussed. Each individual test has been analyzed and now the general results will be presented in graphical and tabular form. The results are examined primarily as a function of the initial notch width (number of broken fibers, NBF). Duplicate tests were run for each notch width and data presented for any given notch width is based on a best-fit curve of the combined data from the duplicate tests.

The ability to predict and detect split initiation has been stressed in this study. Table II shows the experimental and predicted split initiation stress levels for a range of broken fibers. The exact agreement between the experimental average and the predicted value for 19 broken fibers is misleading since it has been forced to be exact. The reasons and method for forcing the exact agreement at this point were discussed in the material properties determination section of the previous chapter. It was hoped that after forcing the model to predict split initiation for 19 broken fibers correctly, it would be able to accurately predict the split initiation stress levels for all notch widths. Except for the 107 broken fiber case, good agreement was found with the predicted values all varying less than six percent from the

experimental average. For most cases, the scatter of experimental data was within reasonable range.

Table II. Split initiation stress levels.

Number of Broken Fibers (NBF)	Experimental Split Initiation Levels (MN/m²)	Experimental Average (MN/m²)	Predicted Value (MN/m²)
19	220, 230	225.0	225.0
27	190, 192	191.0	188.4
37	159, 171, 174, 176, 176	170.0	160.7
55	125, 130, 144, 154	138.3	131.7
71	89, 112, 122, 134	114.3	115.8
81	108, 109	108.5	108.4
107	76, 88	82.0	94.3
143	79, 87	83.0	81.5
215	68, 71	69.3	66.5

Excessive scatter due to coupon or test variation might possibly explain the relatively poor agreement for 107 broken fibers. As discussed in the introduction, variations arising from laminate or coupon preparation, along with variations in test procedure will affect the composite behavior. A sufficient number of duplicate tests must be performed to reduce the random error effects of these variations. From the 71 broken fiber case, it can be seen that the experimental stress values can scatter wide enough to cross over into the stress ranges for other notch widths. Since good agreement was found for all other notch widths, it is likely that scatter and an insufficient number of duplicate tests for 107 broken fibers has caused the inferior result. In fact, the average experimental value is lower than the average for the next larger notch width (143 broken fibers), which indicates faulty data for split initiation values in the 107 broken fiber case. Only two

tests were run with 143 broken fibers (same number as with 107), but, since they show better agreement with predicted results, it is felt that they yielded valid data while the data from 107 broken fibers is in error.

In addition to determining the effectiveness of predicting split initiation, the ability of the model to predict split growth as a function of remote stress was of major importance. Ideally the four matrix splits would grow at the same rate, but as the radiographs have shown, this does not occur. Figure (31) shows the typical split length versus remote stress variations that occur in a single test. It can be seen that each split propagates at a different rate and it is possible for a smaller split to become larger than one or more of the other splits after a small increase in load. To make direct comparisons between tests it was necessary to average the four split lengths present at any stress level. If only one split was present, it was still averaged as if all four splits had been initiated. After averaging the split lengths, the split length versus remote stress data for all tests involving the same notch width were combined and a best-fit curve was determined (using a B-spline fit to discrete data) to represent the behavior for that notch width. Figure (32) shows these curves for several notch widths. It should be noted that the rate of split growth increases with the number of broken fibers. This is expected since greater initial damage will result in higher stress concentrations and shear stresses at the notch tip for a given remote stress. Therefore, more broken fibers will result in the yield stress being reached at a lower remote stress level and more rapid subsequent split growth. The experimental results follow the proper trend, but do not show the

expected amount of variation between different notch widths. Specifically, the closeness of the curves for 27 and 37 broken fibers, as well as for 55 and 71 broken fibers was not expected. It is felt that coupon and test variations are responsible for most of this behavior.

Due to insufficient split length data, a curve was not possible for 143 and 215 broken fibers. The split growth rates for these notch widths were such that splits had grown past the strain gages before a sufficient number of radiographs could be taken. The point where the splits approach the gages is critical since in this range the gages will no longer be measuring remote strain. The splits cause the load carrying portion of the coupon to be reduced by allowing the center region (between the splits) to unload. The strain in the outer, load carrying regions (where the gages are located) increases and no longer represents the remote strain. Therefore, remote stress values obtained from the strain readings become invalid. This behavior places a limit of approximately 60 mm on the maximum split length that can be tolerated for any test before the remote stress values become invalid.

Direct comparison of the experimentally determined average split length versus remote stress data to that predicted by the model reveals large differences. Figures (33), (34), (35), and (36) show this comparison for 19, 27, 37, and 55 broken fibers respectively. Higher numbers of broken fibers were not compared due to the excessive amount of computer time required to determine the predicted behavior. In each of the cases where comparisons were possible, the model predicts a rapid rate of split growth once the splits have been initiated. In contrast, the experimental results reveal that there is a region of slow, stable split growth followed by a region of rapid split growth. Comparison of the

slopes of the predicted curves to the rapid portion of the experimental curves reveals that the actual growth rate approaches the predicted rate, but always remains slower.

The differences between the actual and predicted behavior will be expressed in terms of the percent increase in the initiation stress required to produce an equivalent amount of damage.For comparison purposes, an average split length of 35 mm was chosen. This is well within the region where the remote strain values are known to be reliable. For each case in Figures (33) through (36), the percentage increase in stress needed to cause an average split length of 35 mm in length to be formed was determined. Table III summarizes the results. These values further point out the large disparities existing between the actual and predicted behavior. In all cases, the actual behavior requires that the initiation stress be more than doubled to produce the damage. It is believed that the assumed matrix failure criteria for the model needs to be modified. The modifications will be discussed in the following section.

Table III. Percentage stress increases required to cause 35 mm damage.

NBF	Experimental	Predicted
19	116 %	30 %
27	101 %	27 %
37	107 %	20 %
55	110 %	12 %

It has been emphasized that the test procedure involved unloading the coupon following each load increment. This was done to limit any

viscoelastic creep while the radiograph was being taken. If the coupon had been held at the peak stress level, any non-elastic behavior would act to reduce the stress concentration present at the split tip resulting in a toughened matrix at this location. Some of the preliminary tests were run in this manner. Figure (37) shows the comparison between the test methods for 37 broken fibers. It is obvious that the tests run without unloading resulted in slower split growth. This seems to confirm that matrix toughening does occur and points out that unloading is necessary to provide experimental results that can be compared to the predicted results. The mathematical model used in this study does not account for matrix toughening.

As a final note, it should be mentioned that the AE source location technique was unable to track the split growth. The timing value for most tests was less than 50 microseconds which was too small to obtain sufficient resolution. In addition, the notch acted as a barrier to wave propagation from one side of the notch to the other. With a barrier affecting the wave propagation, the data used to predict source location was most likely erroneous.

Discussion

The results indicate that the shear-lag modeling analysis of [10] is unable to predict accurately the fracture behavior of graphite/epoxy laminates. The model was successful in predicting the point of split initiation, but failed to predict the subsequent split growth rates. The experimental results have revealed the existence of a slow, stable split growth region following split initiation that the model does not predict. It is felt that a discrepancy of this magnitude must be due to improper assumptions for the failure criteria in the model. The model,

as presently developed, assumes that the matrix will fail in pure

shear and that this is the dominant failure mechanism throughout the

fracture process. The experimental results suggest that different

failure mechanisms are responsible for initiating the split and

propagating it during the slow growth phase. Only after the split has

grown to some critical length does failure by shear appear to dominate

as indicated by the increased growth rate. The modified failure

sequence will now be discussed in detail.

From the analysis of the shear-lag model, recall that the matrix

was assumed to support only shear and transverse normal stresses. It

was further assumed that the shear stresses would be the dominant stress

affecting failure and the transverse normal stresses could be neglected

in the failure analysis. It is now felt that the transverse normal

stresses are, in fact, responsible for split initiation and the early,

slow split propagation. The matrix is weak in tension and if the tran-

sverse stresses are tensile, they could cause matrix failure before the

yield stress for shear is reached. The significant question is then,

what is the behavior of the crack tip stresses as the split grows?

A special case of this problem was, in fact, considered by Goree

and Venezia [28] for bonded, isotropic half-planes. Although this sol-

ution does not account for orthotropic materials or distinct fiber and

matrix regions it does give a clear indication as to the nature of the

split growth. Some particular results are given in Figure 38. These

values were obtained by the present authors using the analysis and com-

puter code developed in [28]; i.e. this figure was not taken from [28].

Figure 38 depicts the variation of the stress intensity factors

(coefficients of the singular stress field at the crack tip) where k_1

is the opening mode stress intensity factor and k_2 is the shear mode.

It is clear from Figure 38 that k_1 is a decreasing (stable) function of split length and that k_2 is an increasing function. Further, k_1 is seen to vanish for a split length, C, equal to about ten percent of the transverse notch length. This indicates that the split tip closes and that further growth is due to shear alone. This is very close to the split length found in the present study at which rapid growth starts.

Additional study into this behavior is certainly indicated, with the solution for orthotropic half-planes now being considered by the first author. It is felt however, that the qualitative nature of the longitudinal split growth is as discussed above. That is, the initiation and early stable growth is due to tension and the rapid growth due to shear. It seems that the early part of the splitting process was not observed by Mar and Lin [16], and that their conclusion that the matrix splitting "is caused by shear stresses at the tip of the split" only applies to the later stages of the growth.

A problem still exists in that the mathematical model, as presently developed, predicts compressive transverse stresses at the notch tip. This is in disagreement with the exact solution for the infinite plate described earlier. It appears that, as a consequence of the shear-lag assumption for shear stress transfer, an incorrect boundary condition is imposed on the model that affects the transverse normal stress computation. The assumption in the model states that the shear stress is dependent on the relative axial displacement of adjacent fibers. Since the broken fibers of the notch all displace relative to each other, even on the notch surface, shear stresses are set up in the matrix between the broken fibers. To satisfy equilibrium, shear stresses are required to act on the notch surface which should be stress free. In the model

development, superposition was used to guarantee a stress free notch in the axial direction, but not in the transverse direction, as the solution does not have enough freedom to impose conditions on the shear stresses over this region. Apparently, the existence of the transverse shear stresses on the notch surface causes the model to incorrectly evaluate the transverse matrix stresses at the notch tip. This problem is presently under investigation.

The experimental results do indicate that a rapid growth region due to shear failure does exist, but it does not occur immediately after initiation as the model predicts. Also, the rate of this growth due to shear is less than the predicted rate. Differences between the growth rates can be attributed to the idealized assumptions of laminate construction in the model. First of all, the laminate is modeled as a single-ply of uniformly spaced, identical fibers. If more than one ply is used for experimental coupons, the fibers would have to be perfectly aligned between plies to maintain the modeled configuration. Likewise, the fibers within each ply would have to be perfectly straight and uniformly spaced. For the graphite/epoxy coupons used in this study, the actual conditions are far from these ideal conditions. The yarn nature of the graphite fibers makes them difficult to align and space properly when in the pre-preg tape form. This nonuniformity within a single ply is compounded when several plies are combined to form a laminate. The curing process allows the fibers to deviate further from the ideal configuration. As a result, there will be numerous interferences with the ideal matrix fracture path that will tend to decrease the growth rate. Examination of the fracture surfaces under a stereo microscope confirms that the splits do follow a winding path through the matrix to form a complete split.

The model also assumes that the matrix damage will be restricted to the region between the last broken fiber bundle and the first unbroken bundle. Awerbuch and Hahn [29] have documented fracture surface studies on graphite/epoxy laminates and have observed that, in many cases, a complete fiber tow may fail in addition to matrix splitting parallel to the fibers. A fracture surface examination for this study did indicate some fiber breakage along the split. The model does not account for matrix splitting that crosses over fibers and this will surely cause a decreased split growth rate.

These deviations from ideal behavior are, for the most part, unavoidable when using graphite/epoxy. The problems can be reduced by using a composite such as boron/epoxy. Boron fibers are single fibers, not yarns formed by combining many smaller filaments. They can be spaced much more uniformly and provide a fracture path very similar to the model. Some initial testing has been done on boron/epoxy and the preliminary results are very good. As Figure (39) shows, the boron/epoxy laminate has the same initial slow growth region as was found with graphite/epoxy. The subsequent rapid growth region due to shear failure has a higher rate, though. In fact, the rapid growth region agrees very well with the predicted growth rate. This indicates that the model describes failure by shear very well, but lacks the ability to describe the failure due to transverse normal stresses.

As discussed previously, the model is able to predict the actual split initiation stress levels accurately, even though it apparently does not consider the appropriate mechanism for split initiation. The assumed failure mode, shear failure, does appear to take over in an abrupt manner, though. This is evidenced by the bilinear nature of the

curves in Figure (32). If indeed the model does describe the shear stresses accurately, then it is felt that it should be able to predict the point where shear failure begins to dominate the fracture behavior.

To check for the ability of the model to predict the initiation of splitting due to shear, the same procedure used earlier to match experimental and analytical values for 19 broken fibers is used. If one visualizes the removal of the slow growth portion of the curves in Figure (35) and moves the remaining portion down to the stress axis (zero split length level), the resulting curve closely resembles the predicted behavior with the initiation point being the point where shear failure is assumed to begin. As before, one notch width will be chosen for the curve fitting and material properties determination process. The 37 broken fiber case is chosen since it has reliable COD values for full load at the apparent shear split initiation point. The values needed are

$$\sigma_\infty = 240 \text{ MPa, and}$$
$$\text{COD} = 0.075 \text{ mm.}$$

The computer solution for split initiation is matched to these values and the material properties are found to be

$$G_M/h = 4.946 \times 10^{12} \text{ N/m}^3 \quad (18.2 \times 10^6 \text{ lb/in}^3), \text{ and}$$
$$\tau_o = 5.314 \times 10^7 \text{ N/m}^2 \quad (7707 \text{ psi})$$

The yield stress has increased and the modulus has decreased as expected since the apparent failure stress of the matrix is greater than the

value used when it was thought that shear was responsible for split initiation. These material properties are used to predict the split initiation levels due to shear for other notch widths. Table IV summarizes the estimated experimental values and the predicted values. There seems to be good agreement for the cases where experimental estimates could be made. The 19 and 55 broken fiber cases did not have distinct points where the split growth rate changed abruptly. Further testing should be done to get a more accurate value for the point of failure mode changeover, but the initial results indicate that the model is able to predict split initiation due to shear failure. This further supports the conclusion that the model is approximating the shear stresses accurately.

Table IV. Stress values at which shear dominated failure begins to dominate the fracture behavior.

NBF	Estimated Experimental Value	Predicted Value
19	No estimate	336 MN/m^2
27	292 MN/m^2	281 MN/m^2
37	240 MN/m^2	240 MN/m^2
55	No estimate	197 MN/m^2
71	185 MN/m^2	173 MN/m^2
81	167 MN/m^2	162 MN/m^2
107	138 MN/m^2	141 MN/m^2

Also from Figure (32), note that there appears to be a relatively constant amount of slow split growth before shear begins to dominate. In all cases where the bilinearity is pronounced, the average split length is four to five millimeters when the split growth rate increases substantially. Whether this is a critical split length at which transverse stresses die out or become compressive, or the point at which

shear stresses have increased to where they control the behavior can not be determined. This split length does appear to be independent of the initial notch width, though. It has become obvious that more work is needed to determine which fracture modes, or combinations of modes, control the fracture behavior during the transition from slow to fast split growth.

It should be pointed out that the inability of the shear-lag model to predict adequately the fracture behavior of graphite/epoxy does not contradict the findings of Goree and Jones [15] in their work with boron/aluminum. The dominant fracture processes in boron/aluminum are matrix yielding due to shear and transverse damage due to tensile fracture of the fibers. The model is capable of describing accurately the stresses responsible for these failure modes. The transverse matrix normal stresses do not play a significant role in boron/aluminum damage as they apparently do with graphite/epoxy.

A further comparison between the present work and that of Mar and Lin [16] is given in Figure (40), where the results of Figure 7 in [16] are compared with normalized values obtained from Tables II and IV in this report. The unnotched tensile strength of the laminates used in this study was 1.17 GPa (169.7 x 10^3 psi). It is seen that the axial stress at which shear splitting appears to begin (Table IV) is much closer to [16] than the early tension related split initiation of Table II. From this comparison it seems that the aluminum honeycomb used in the four-point bend test coupons [16] gave some constraint to the splitting and increased the toughness and also masked the early tension splitting completely.
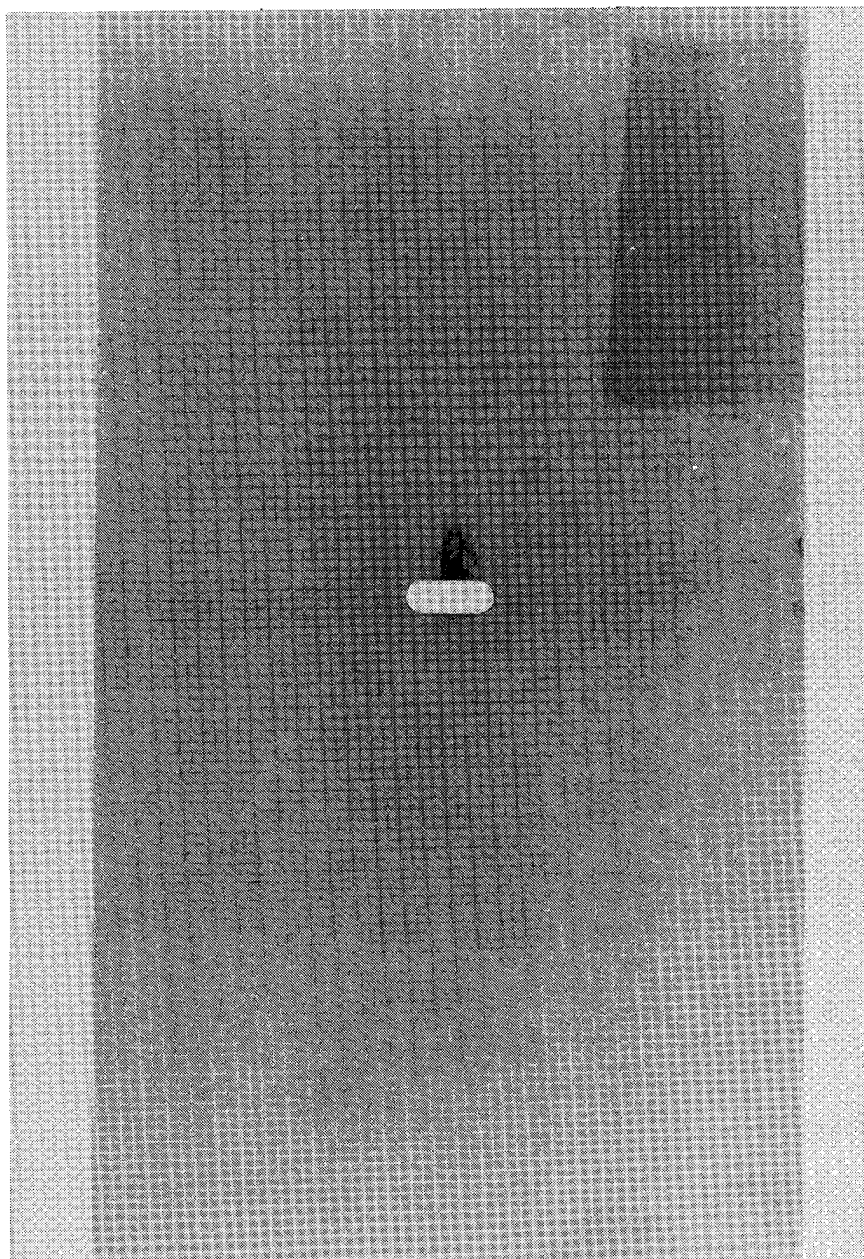
Figure 15. Baseline radiograph.
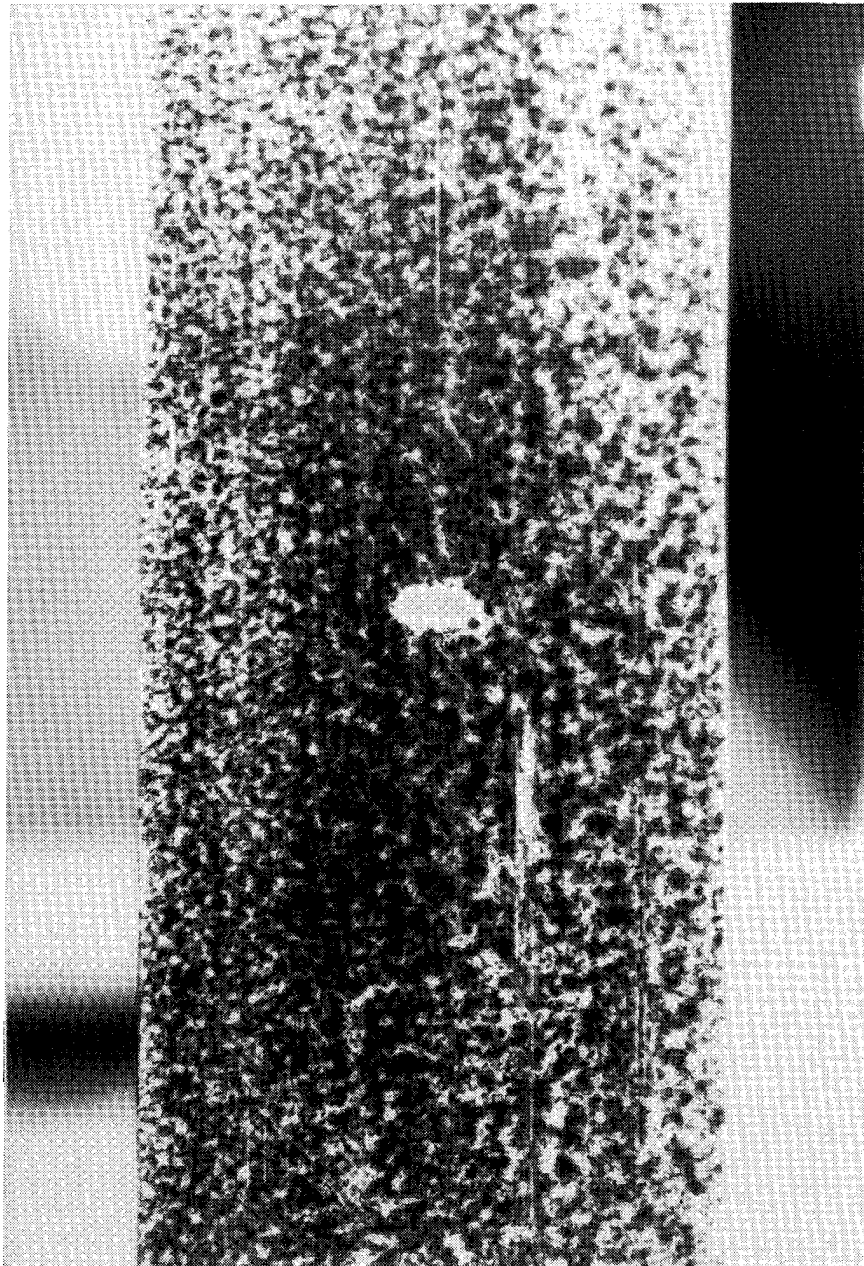
Figure 16. Baseline brittle coating photograph.
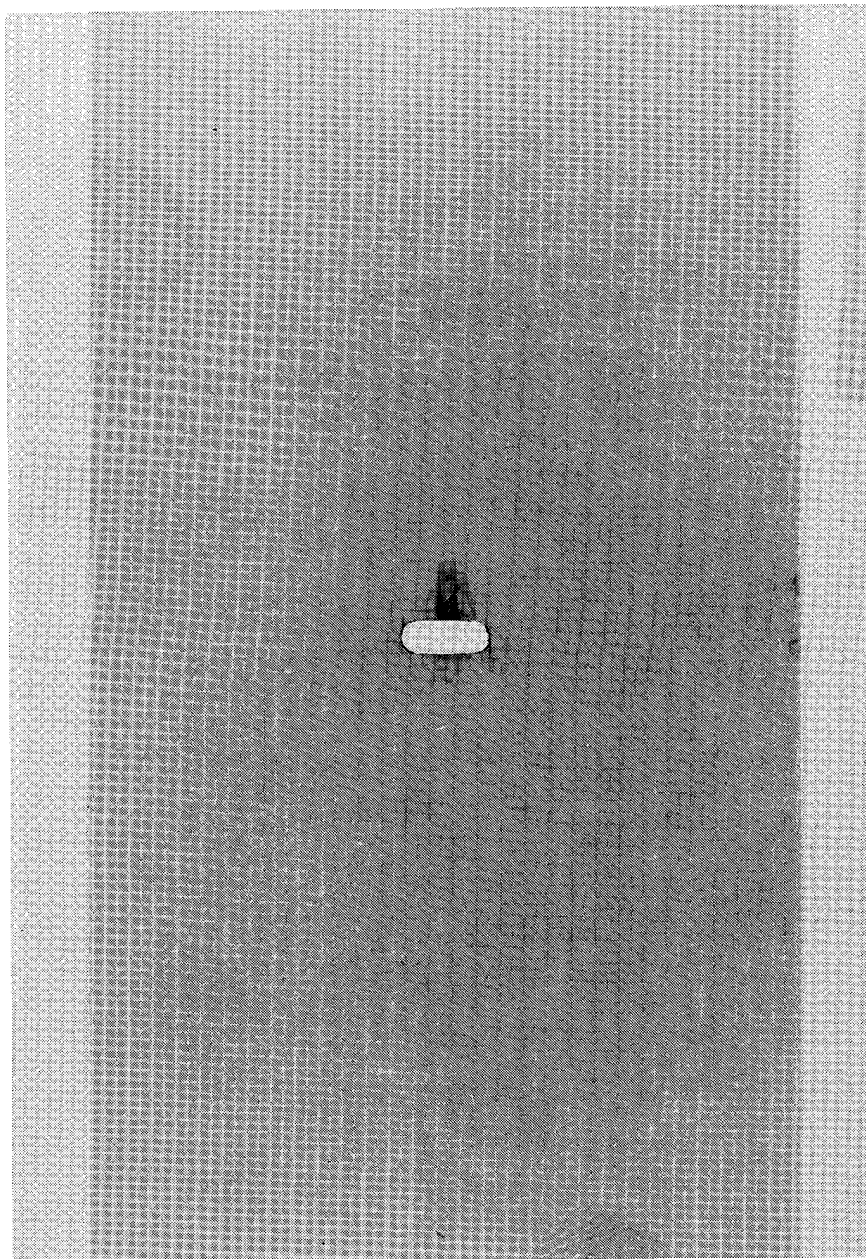
Figure 17. Radiograph of damage at 176 MN/m^2: 15.0 percent of unnotched ultimate stress.
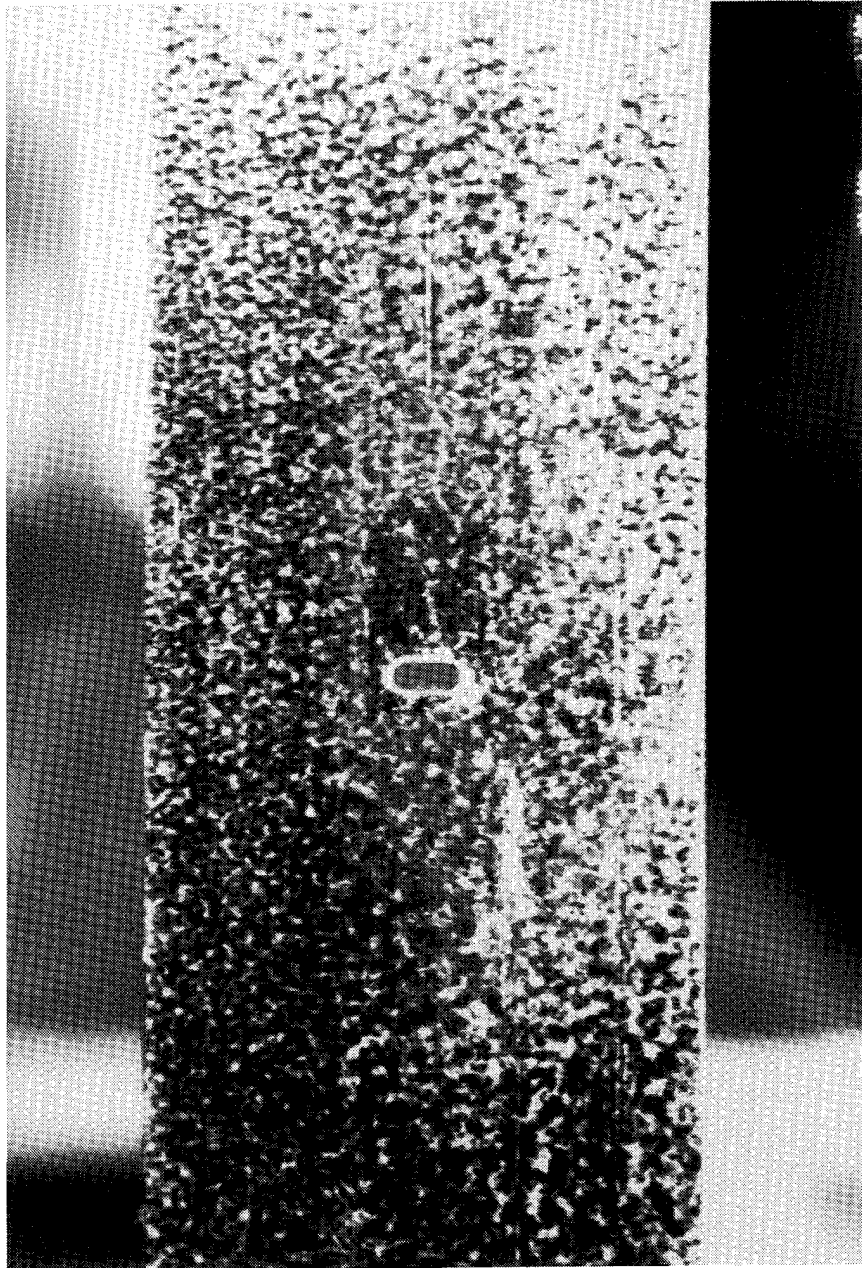
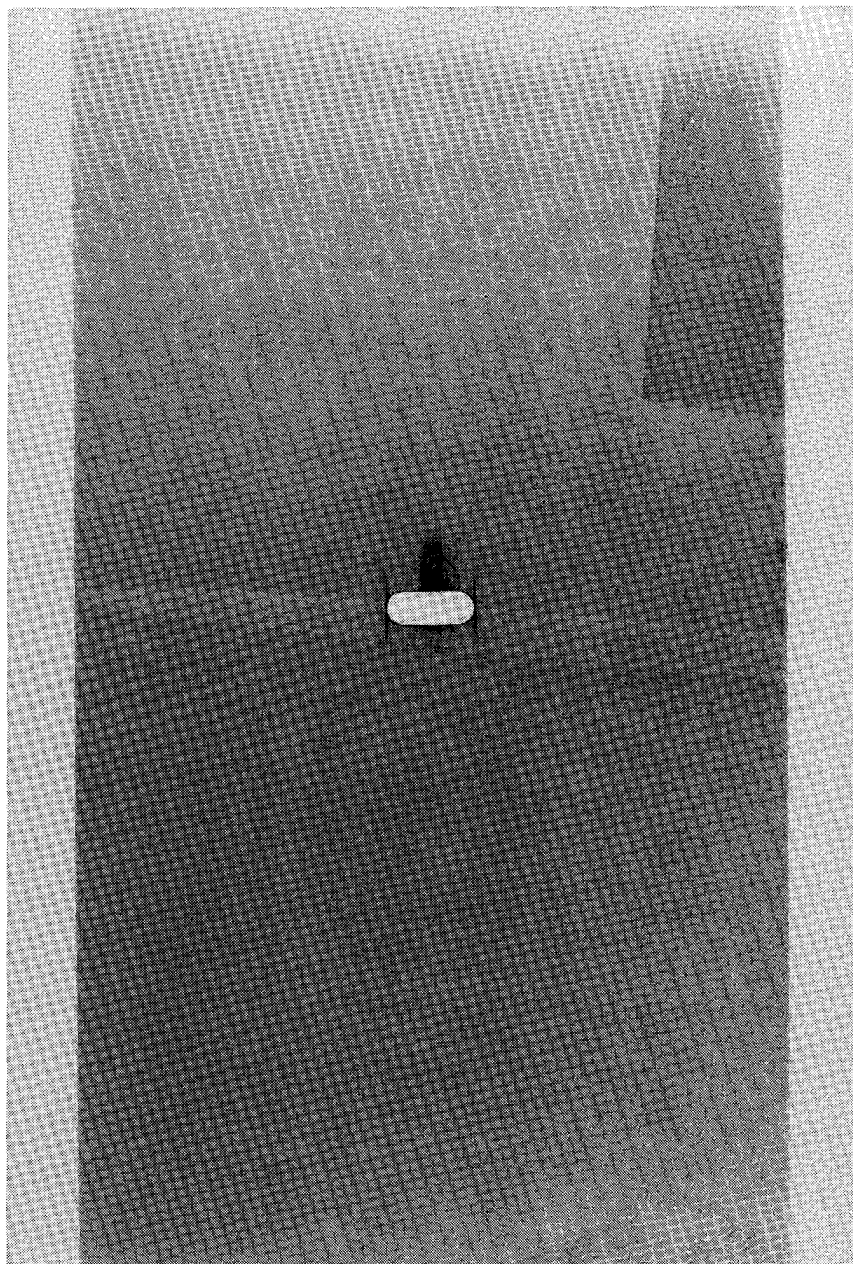Figure 18. Brittle coating photograph of damage at 176 MN/m^2: 15.0 percent of unnotched ultimate stress.

Figure 19. Radiograph of damage at 218 MN/m^2: 18.6 percent of
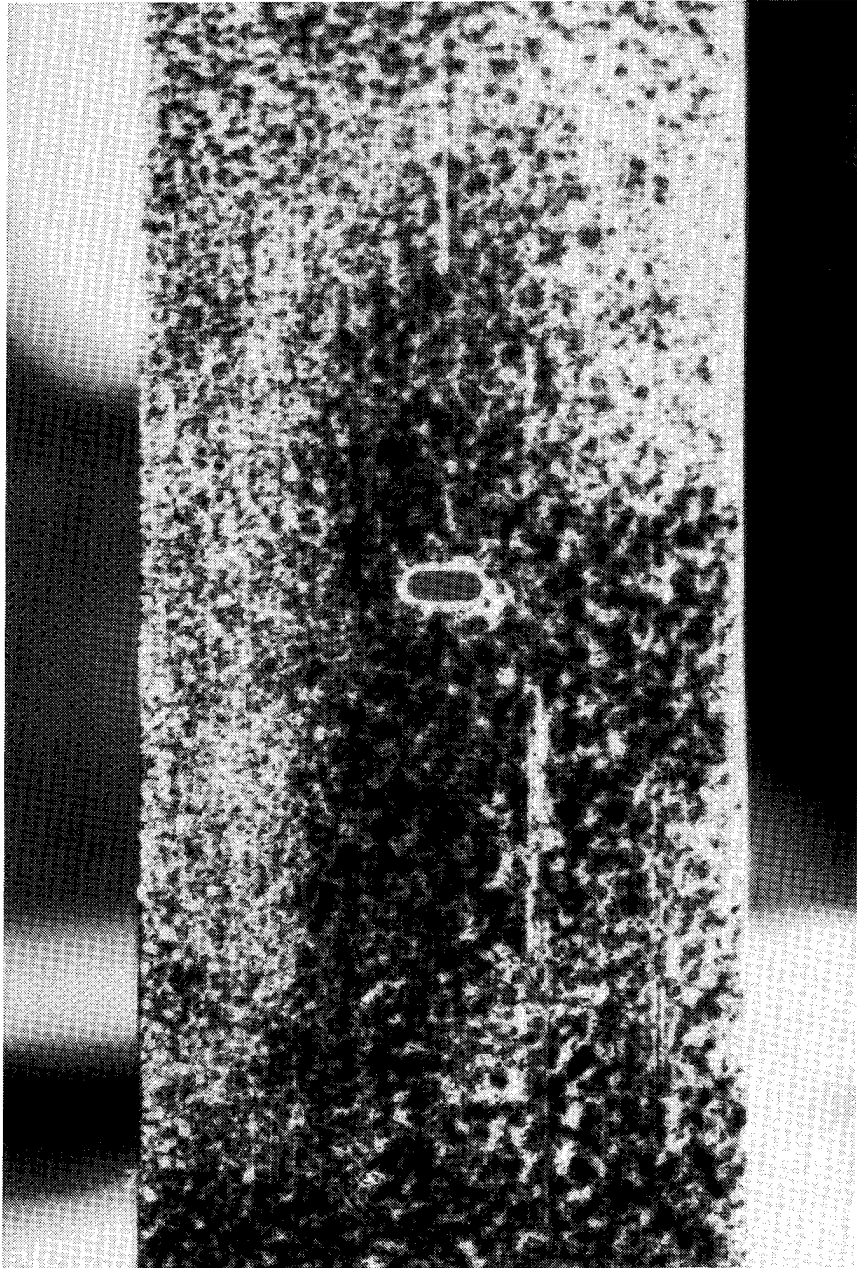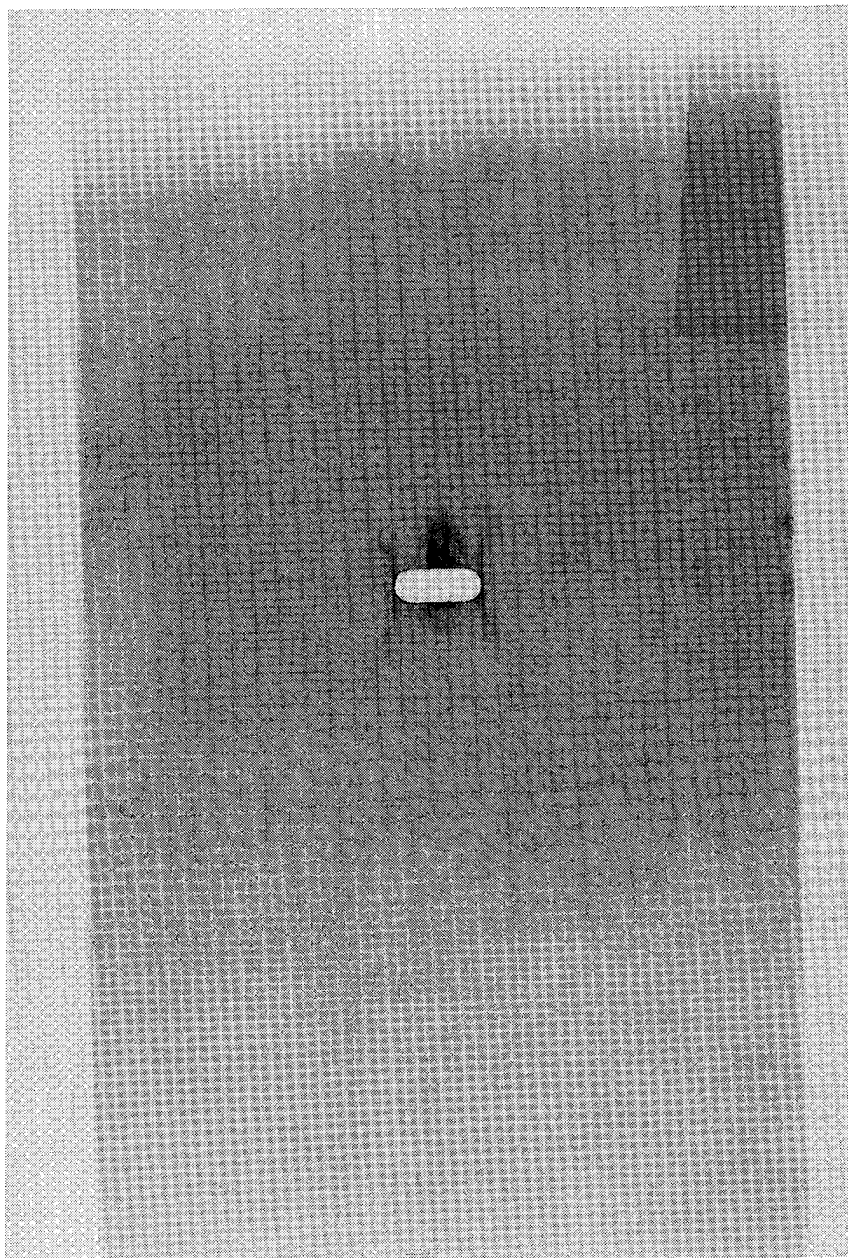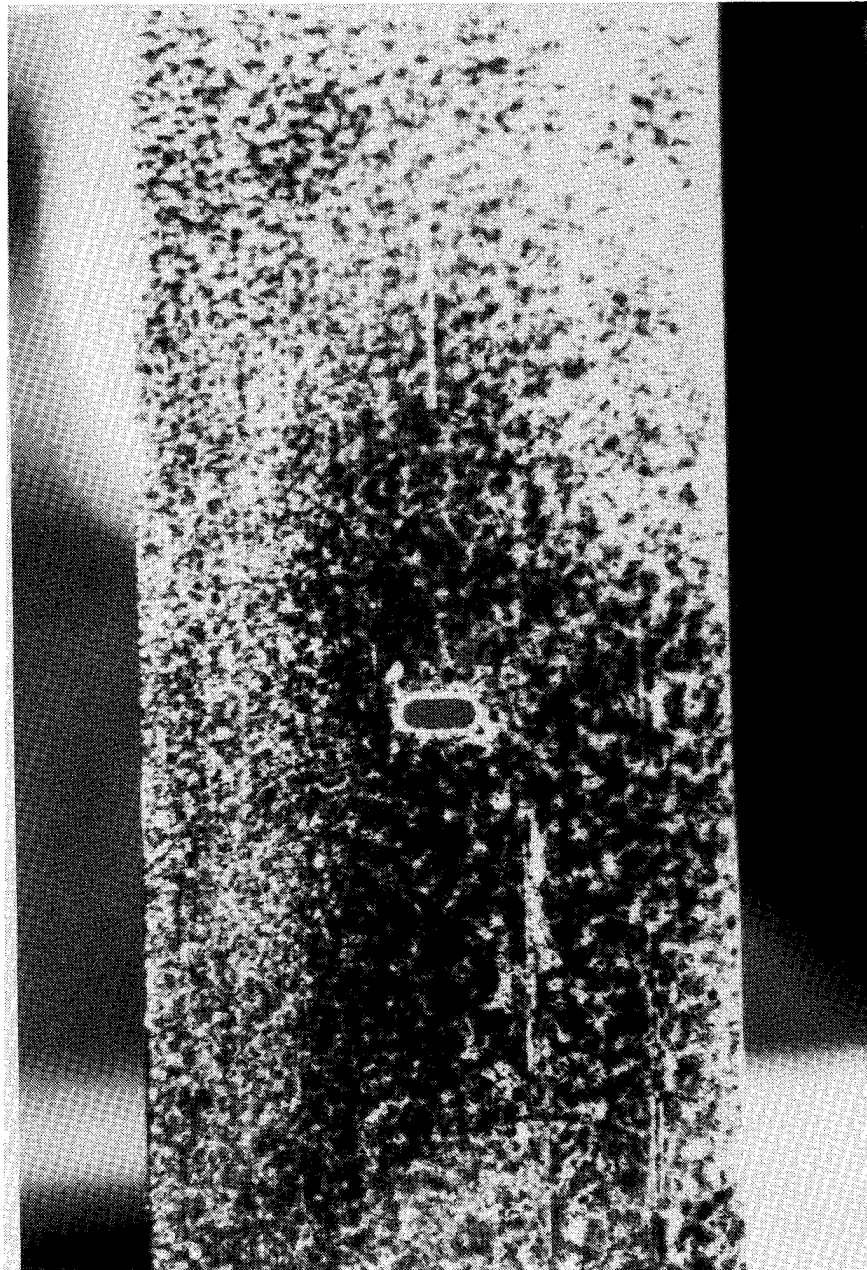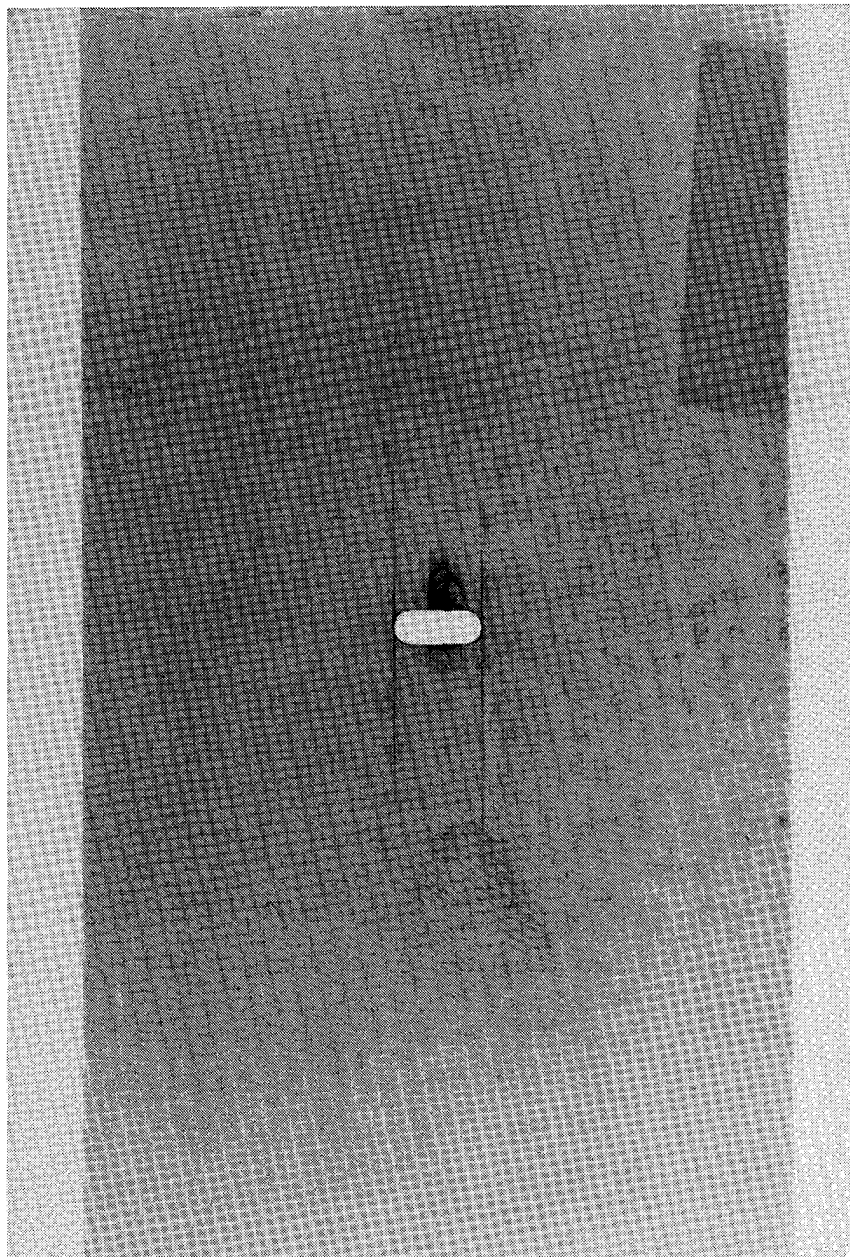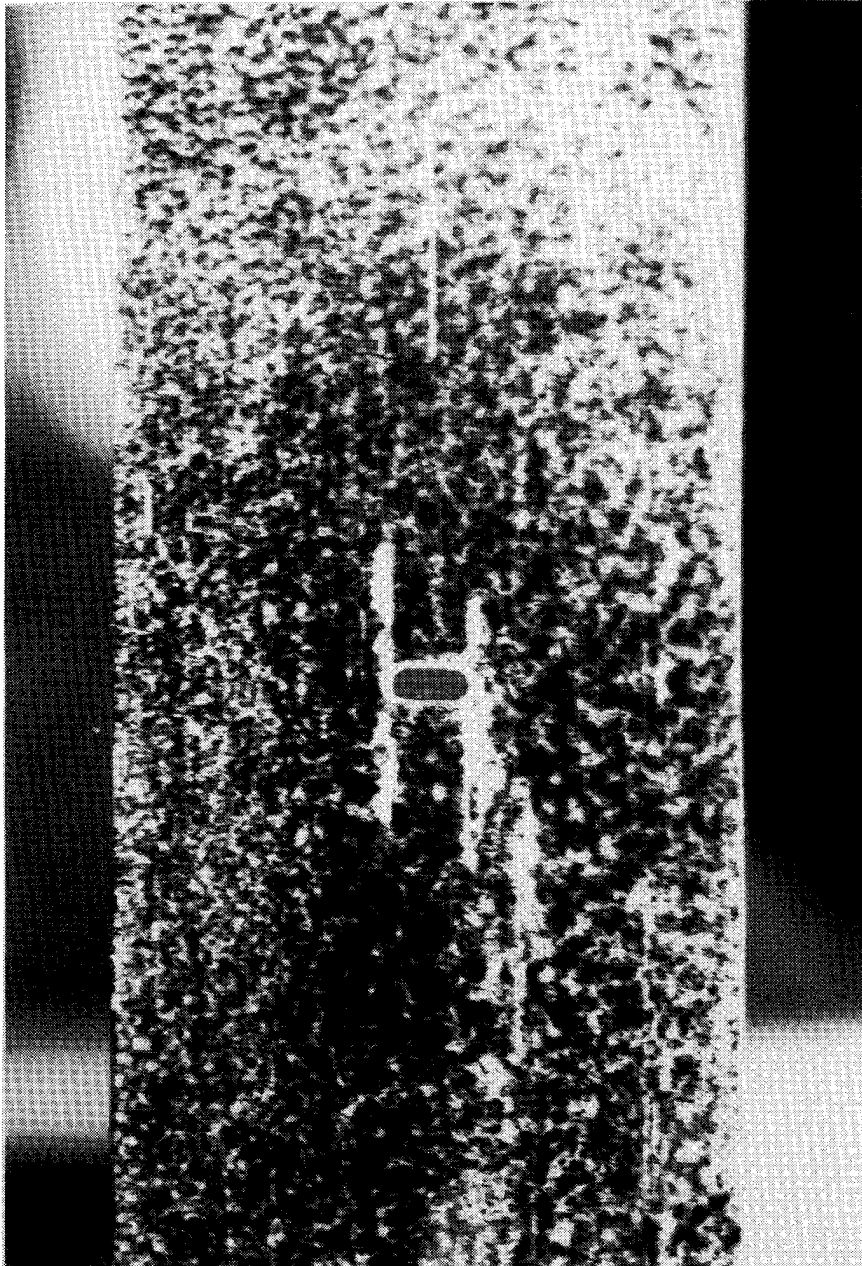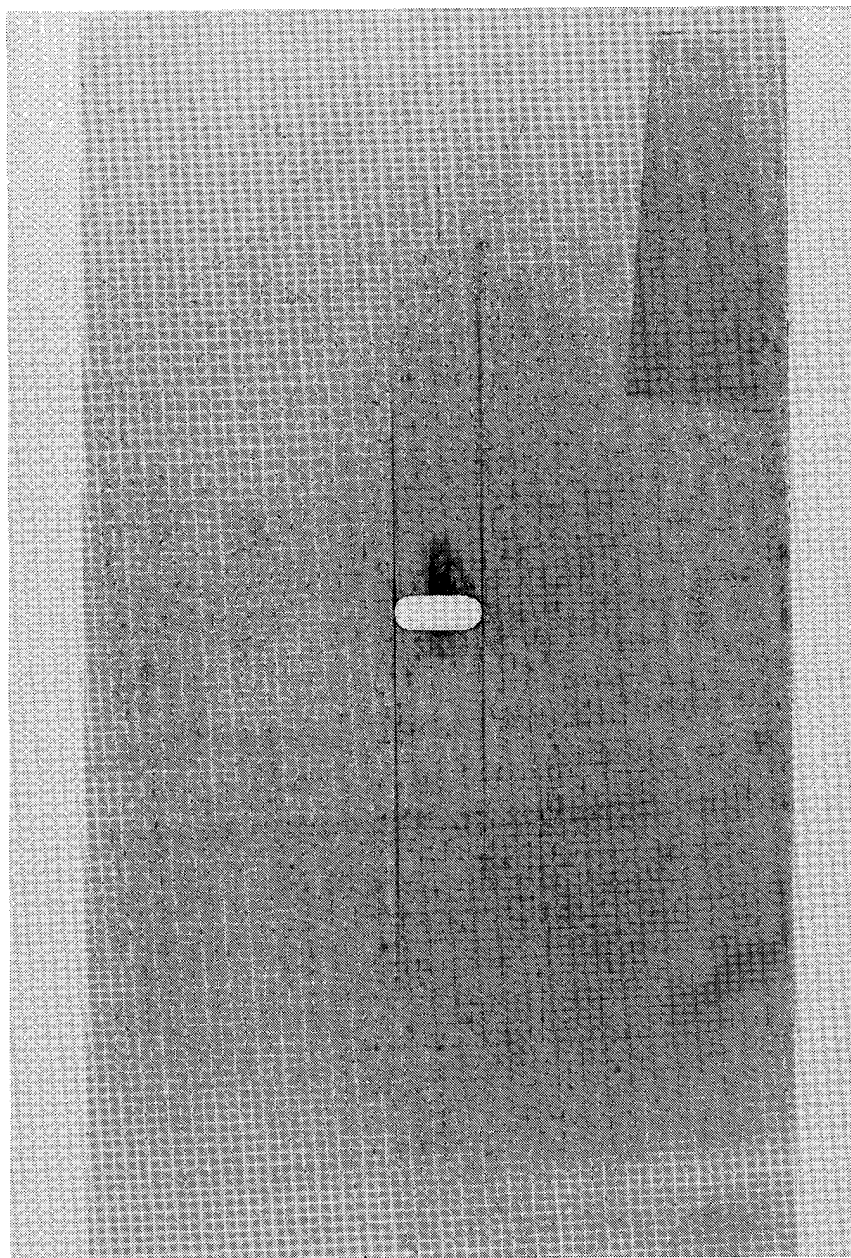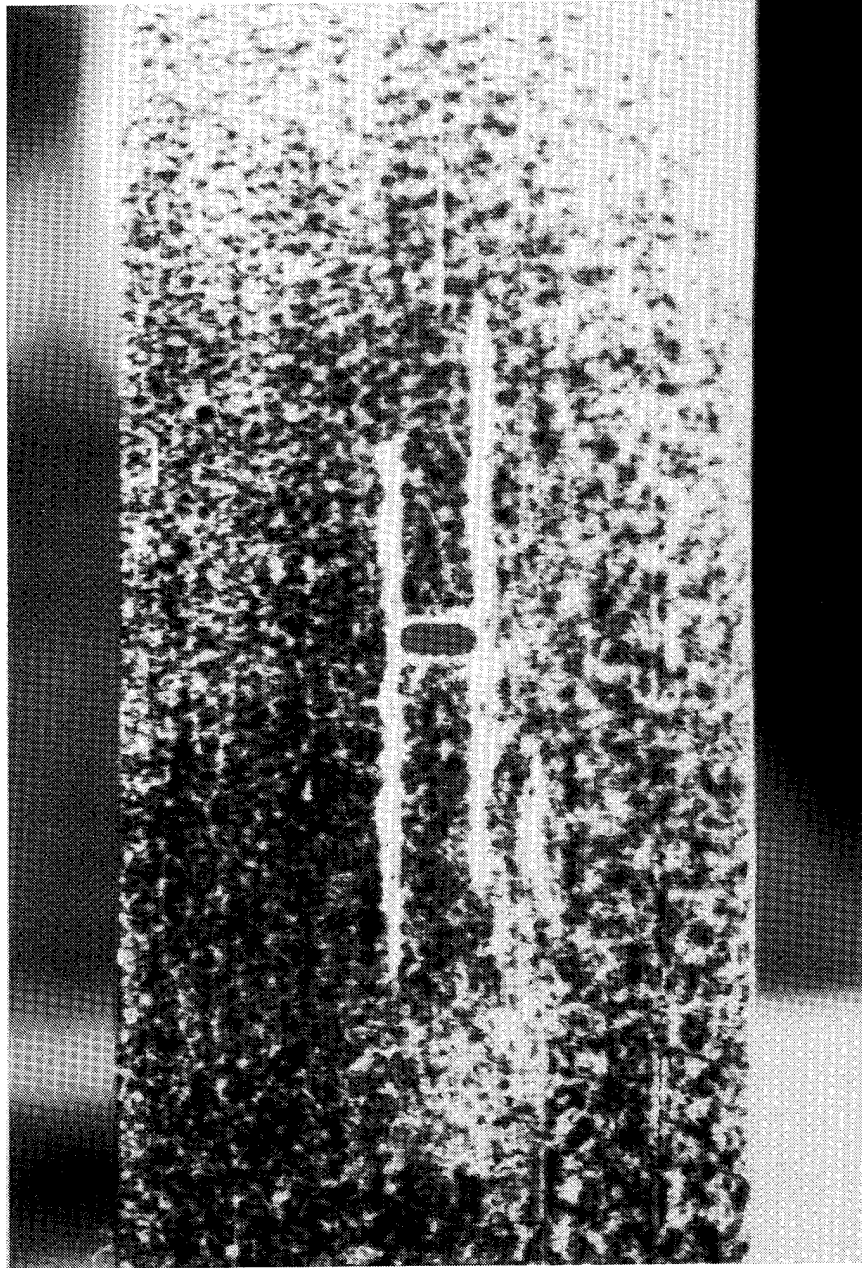unnotched ultimate stress.

Figure 20. Brittle coating photograph of damage at 218 MN/m^2: 18.6 percent of unnotched ultimate stress.

Figure 21. Radiograph of damage at 248 MN/m^2: 21.2 percent of
unnotched ultimate stress.

Figure 22. Brittle coating photograph of damage at 248 MN/m^2: 21.2 percent of unnotched ultimate stress.

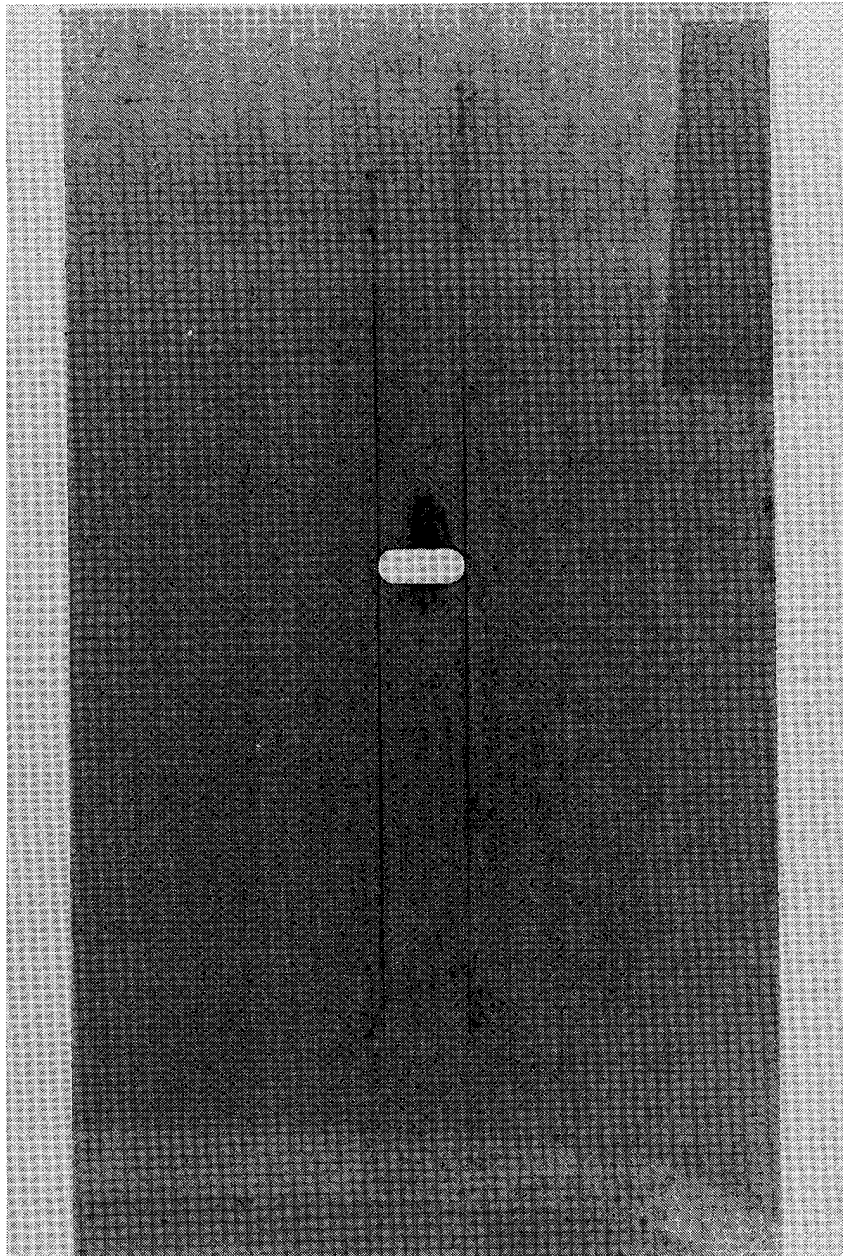Figure 23. Radiograph of damage at 270 MN/m^2: 23.1 percent of unnotched ultimate stress.
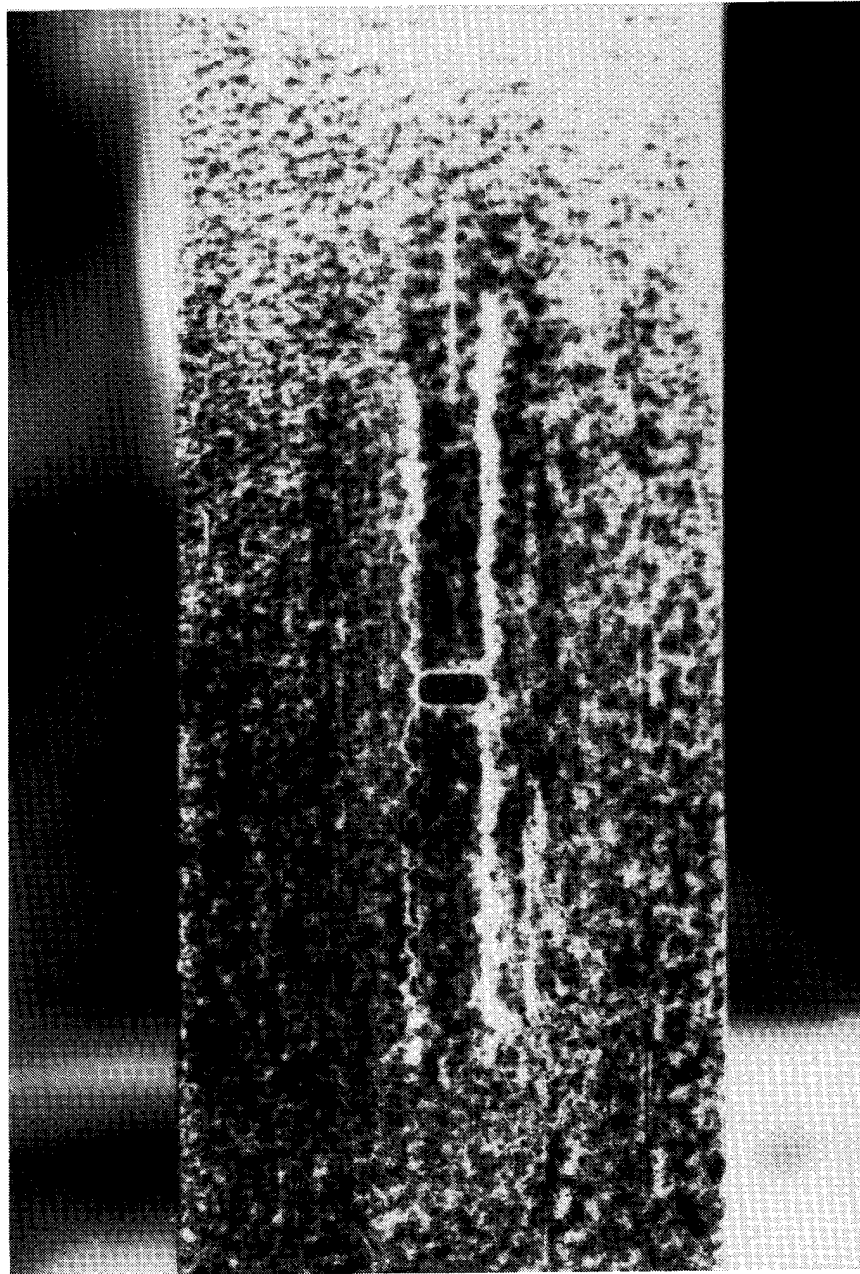
Figure 24. Brittle coating photograph of damage at 270 MN/m^2:
23.1 percent of unnotched ultimate stress.

Figure 25. Radiograph of damage at 304 MN/m^2: 26.0 percent of unnotched ultimate stress.

Figure 26. Brittle coating photograph of damage at 304 MN/m^2:
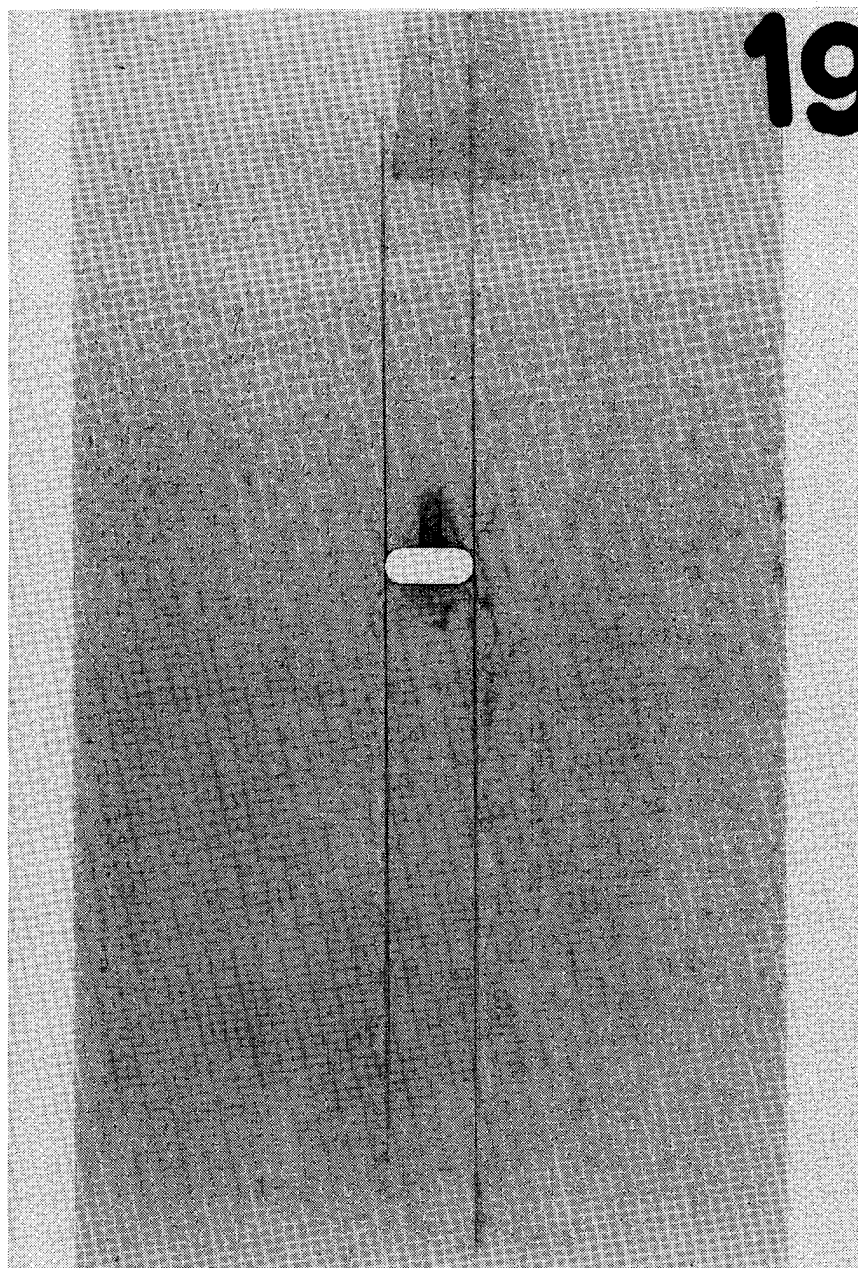26.0 percent of unnotched ultimate stress.

Figure 27. Radiograph of damage at 341 MN/m^2: 29.1 percent of unnotched ultimate stress.

84

Figure 28. Brittle coating photograph of damage at 341 MN/m^2: 29.1 percent of unnotched ultimate stress.

Figure 29.   Radiograph of damage at 373 MN/m^2: 31.9 percent of
             unnotched ultimate stress.
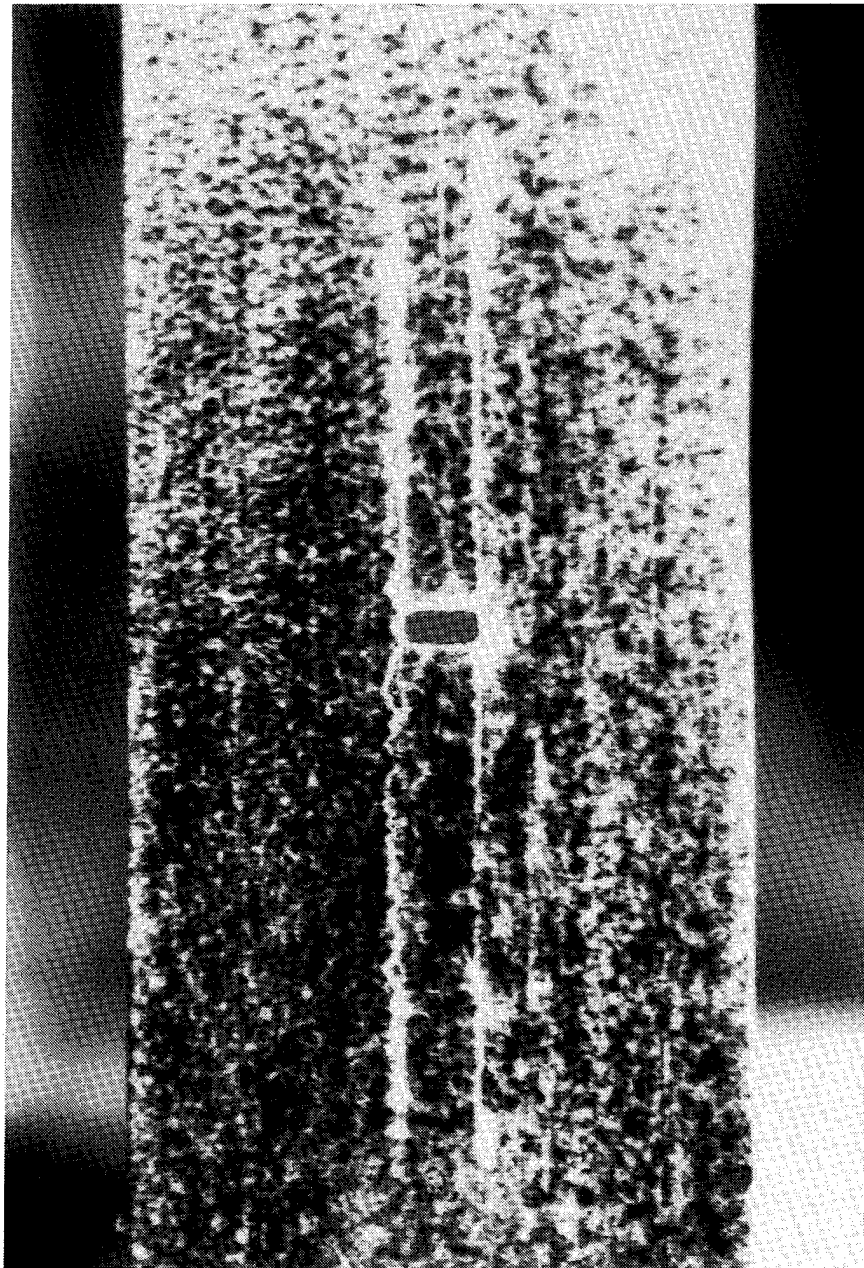
Figure 30. Brittle coating photograph of damage at 373 MN/m^2:
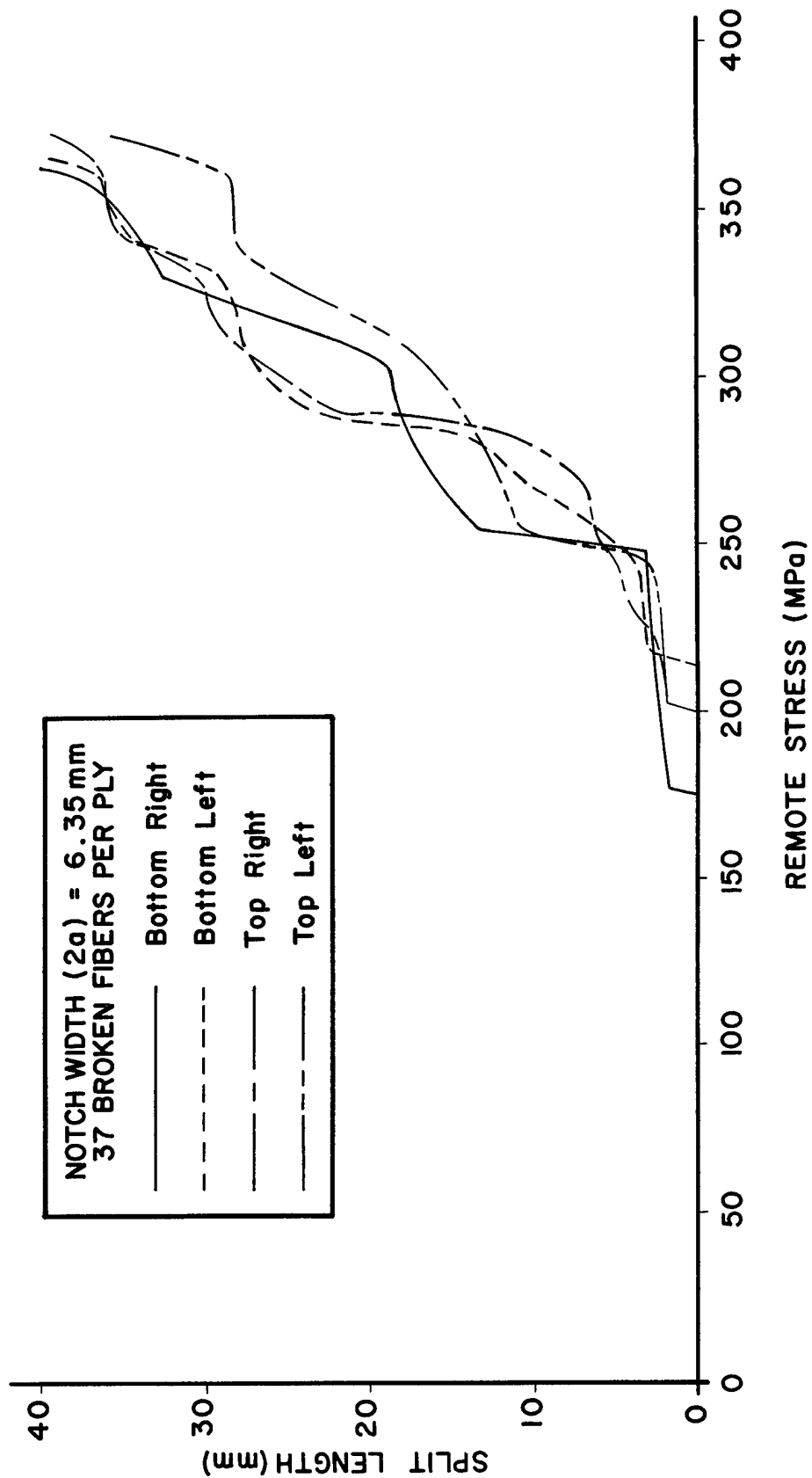31.9 percent of unnotched ultimate stress.

Figure 31. Experimental average split length versus remote stress showing the variation of growth rates among the splits of a single coupon.
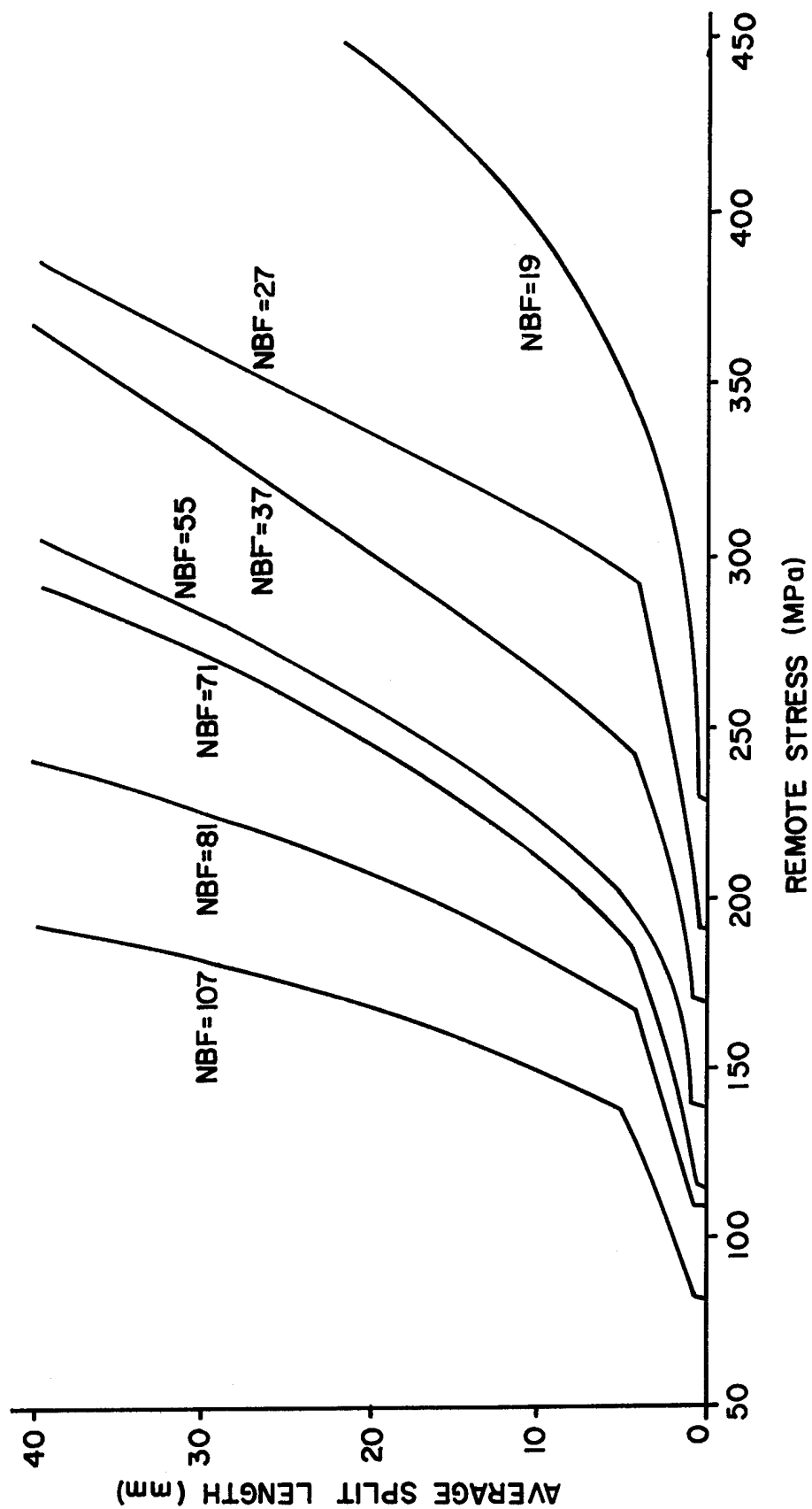
Figure 32. Experimental average split length versus remote stress for several notch widths.
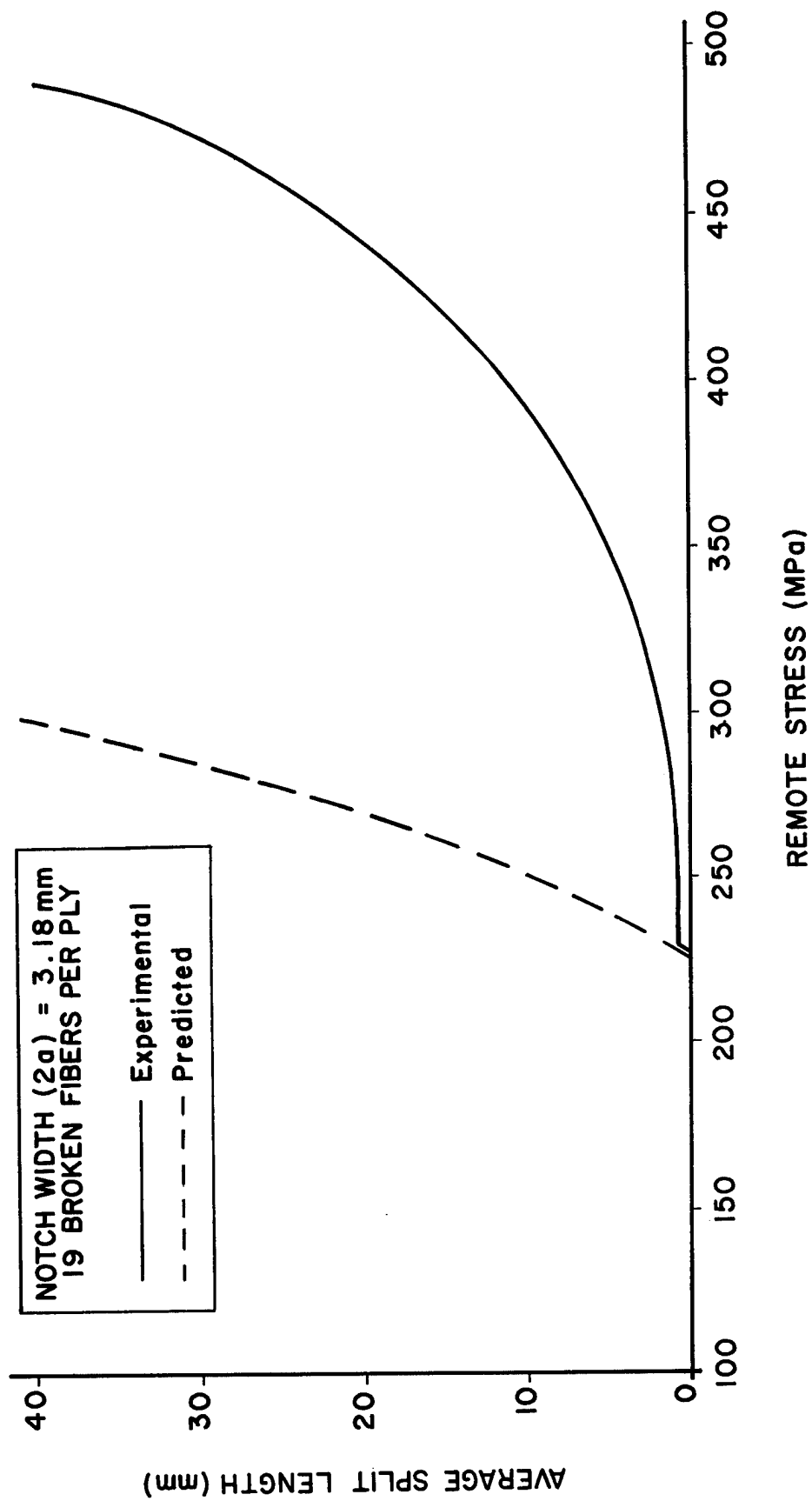
Figure 33. Average split length versus remote stress for 19 broken fibers: comparison of experimental and predicted behavior.
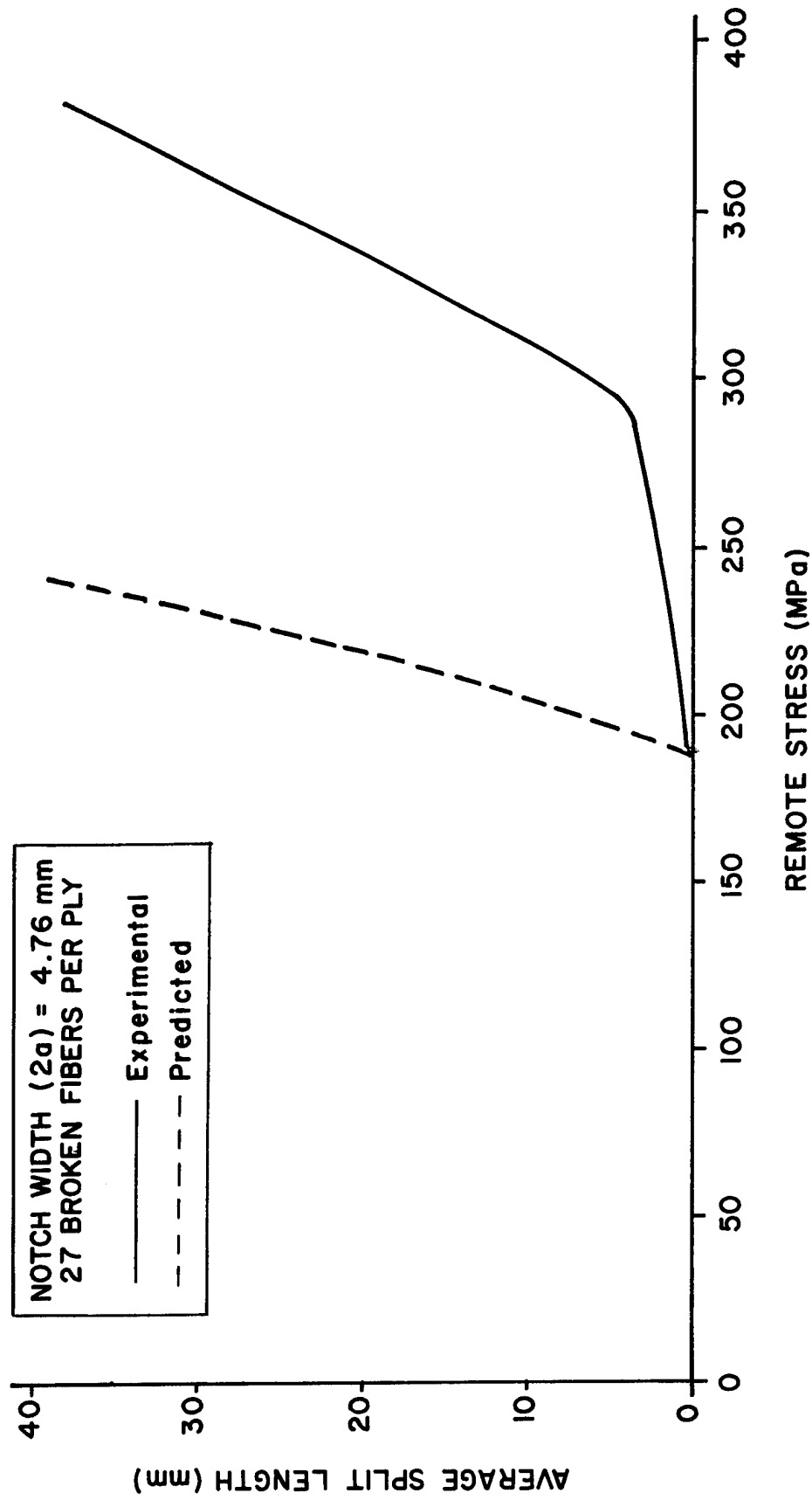
Figure 34. Average split length versus remote stress for 27 broken fibers: comparison of experimental and predicted behavior.

Figure 35. Average split length versus remote stress for 37 broken fibers: comparison of experimental and predicted behavior.
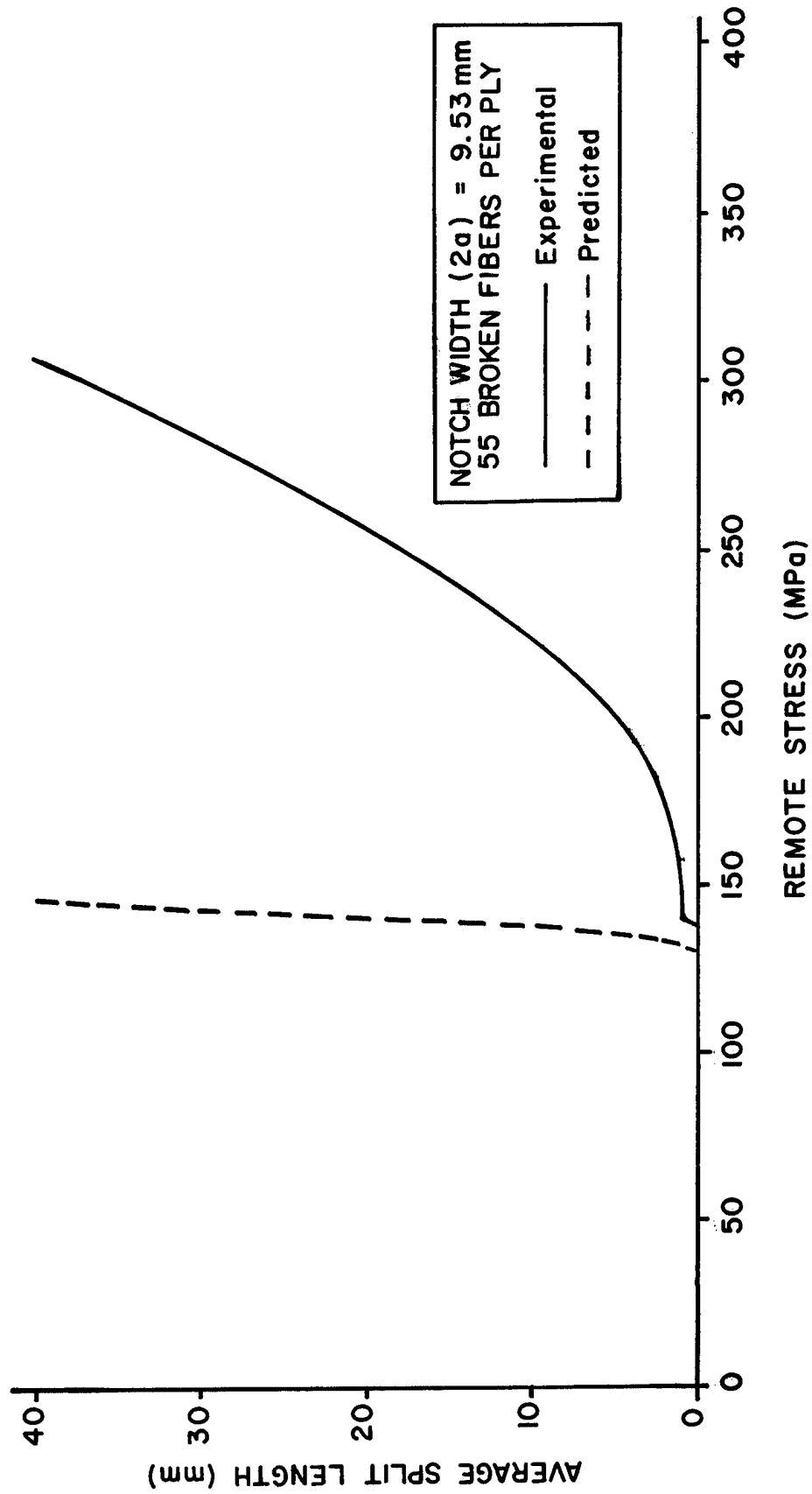
Figure 36. Average split length versus remote stress for 55 broken fibers: comparison of experimental and predicted behavior.
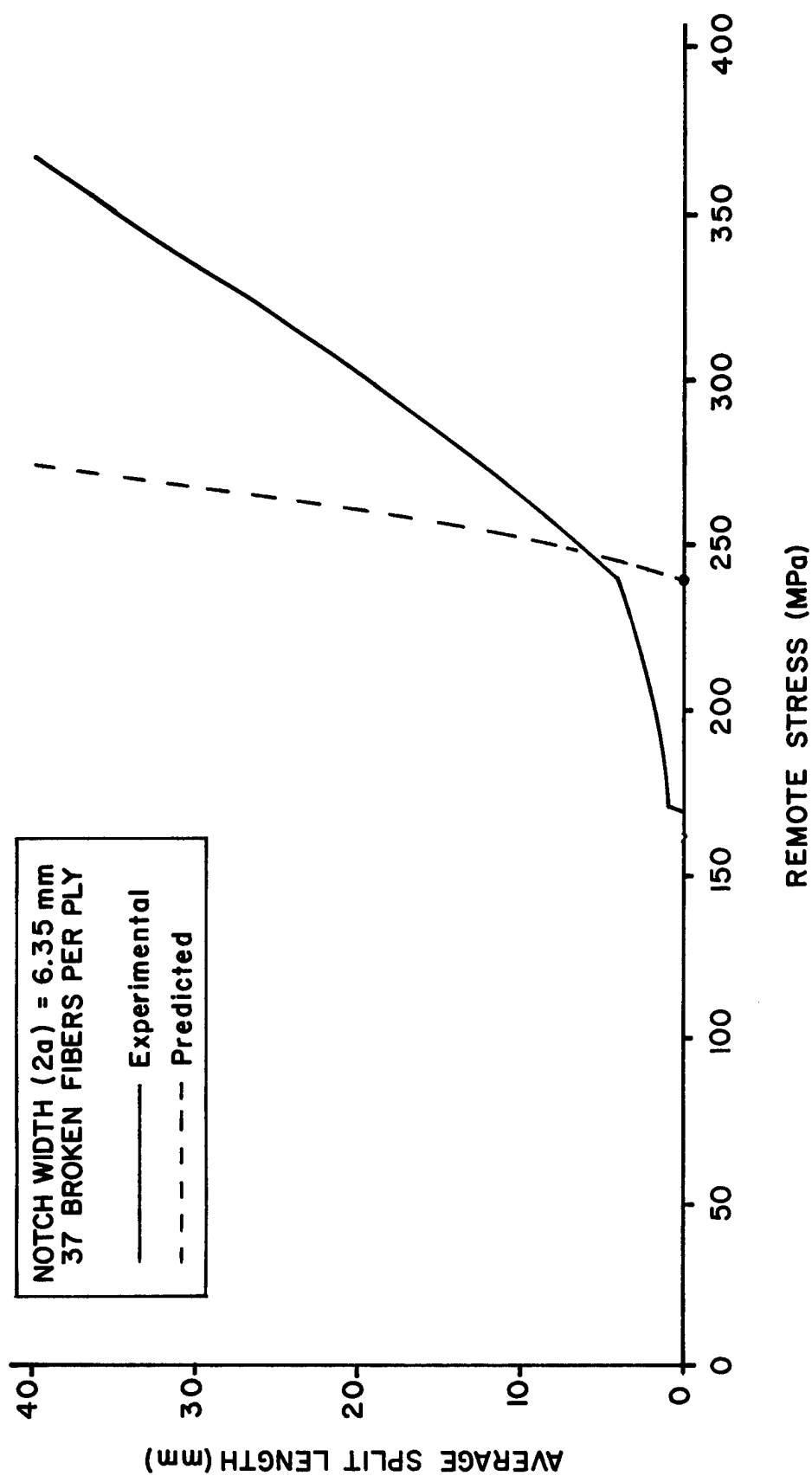
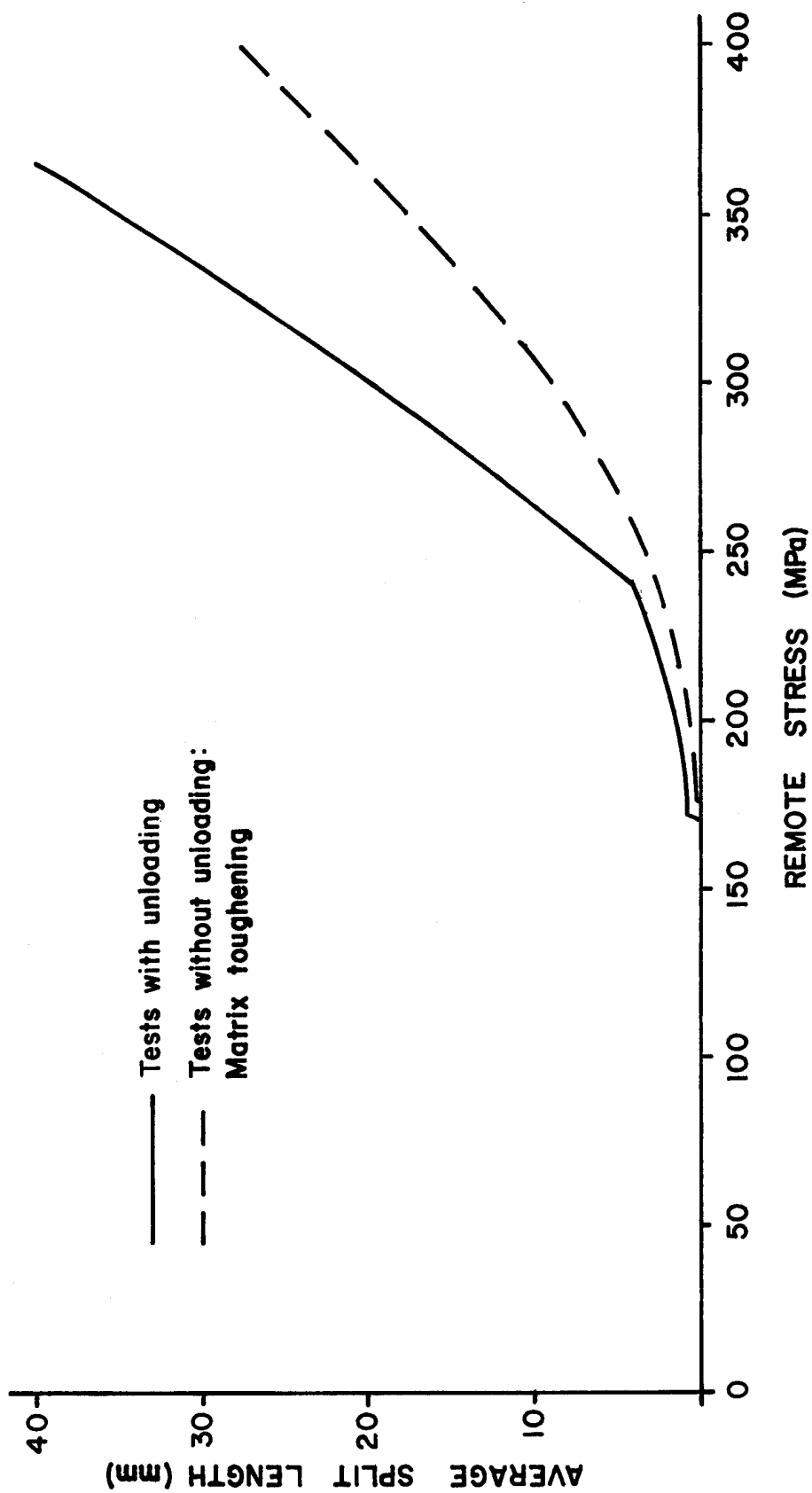Figure 37. Experimental average split length versus remote stress for 37 broken fibers: comparison of test procedures.
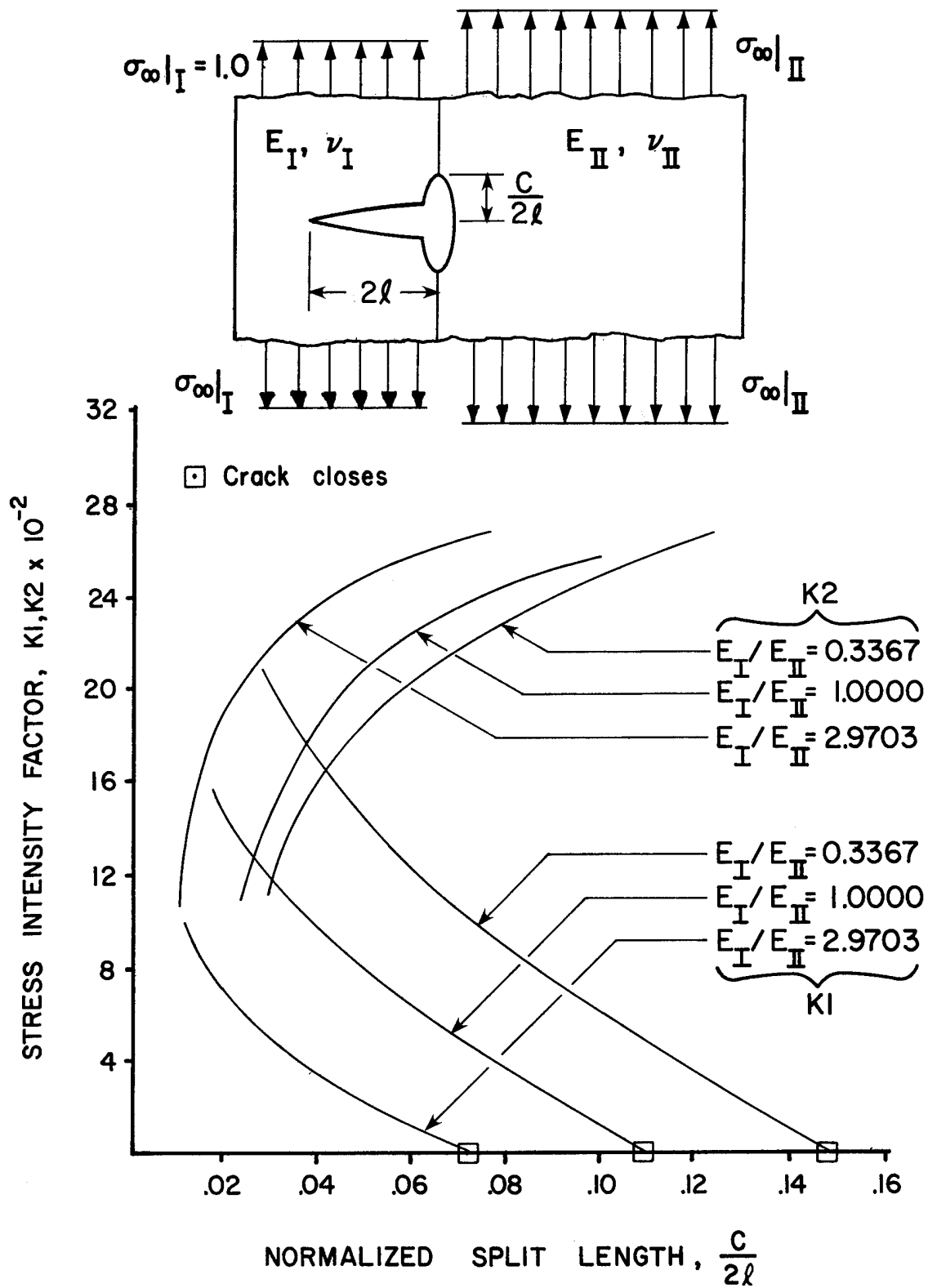
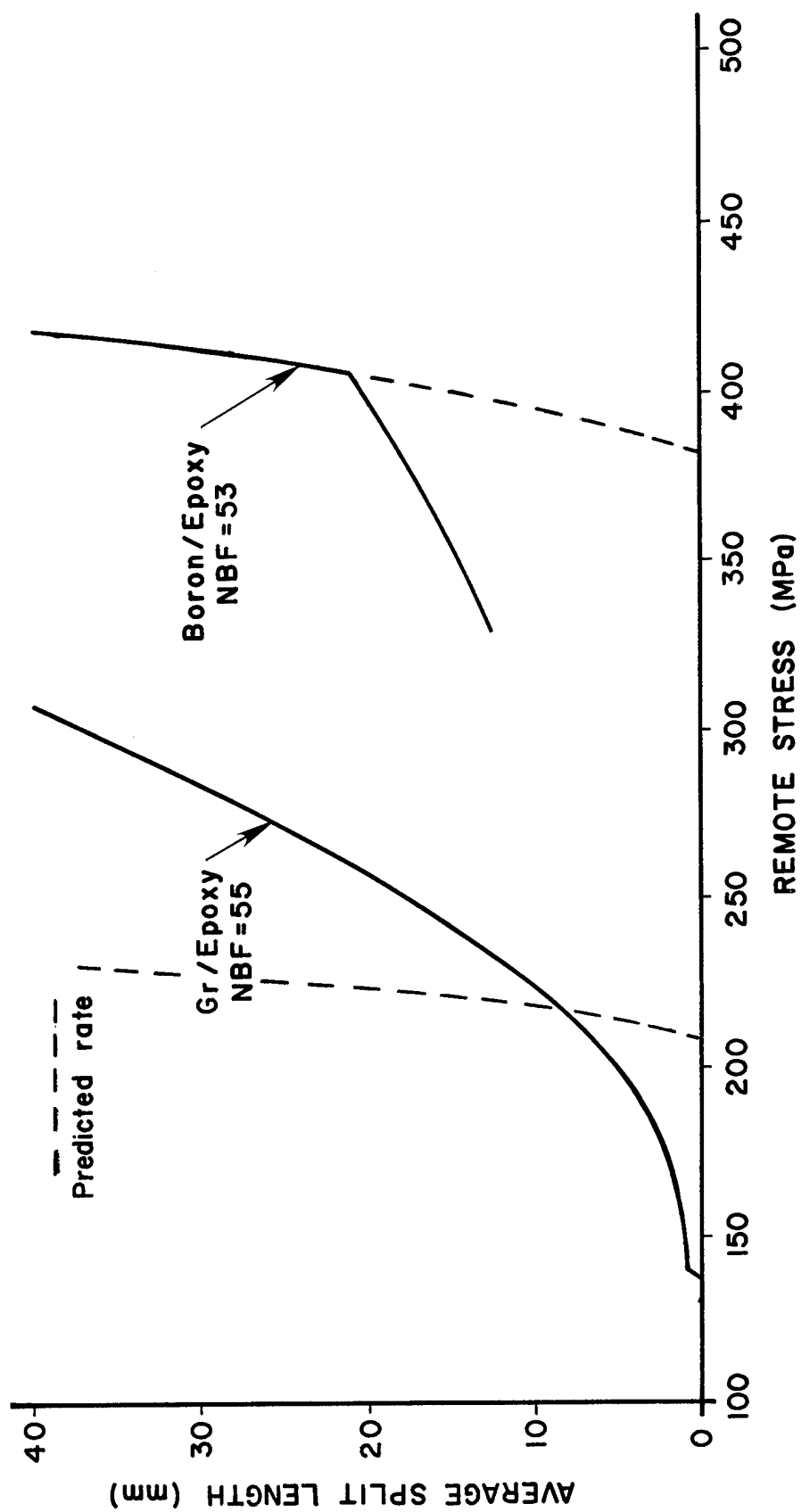Figure 38. Stress intensity factors at the split tip, obtained from reference [28].

Figure 39. Average split length versus remote stress: comparison of graphite/epoxy and boron/epoxy split behavior to predicted split growth rates.
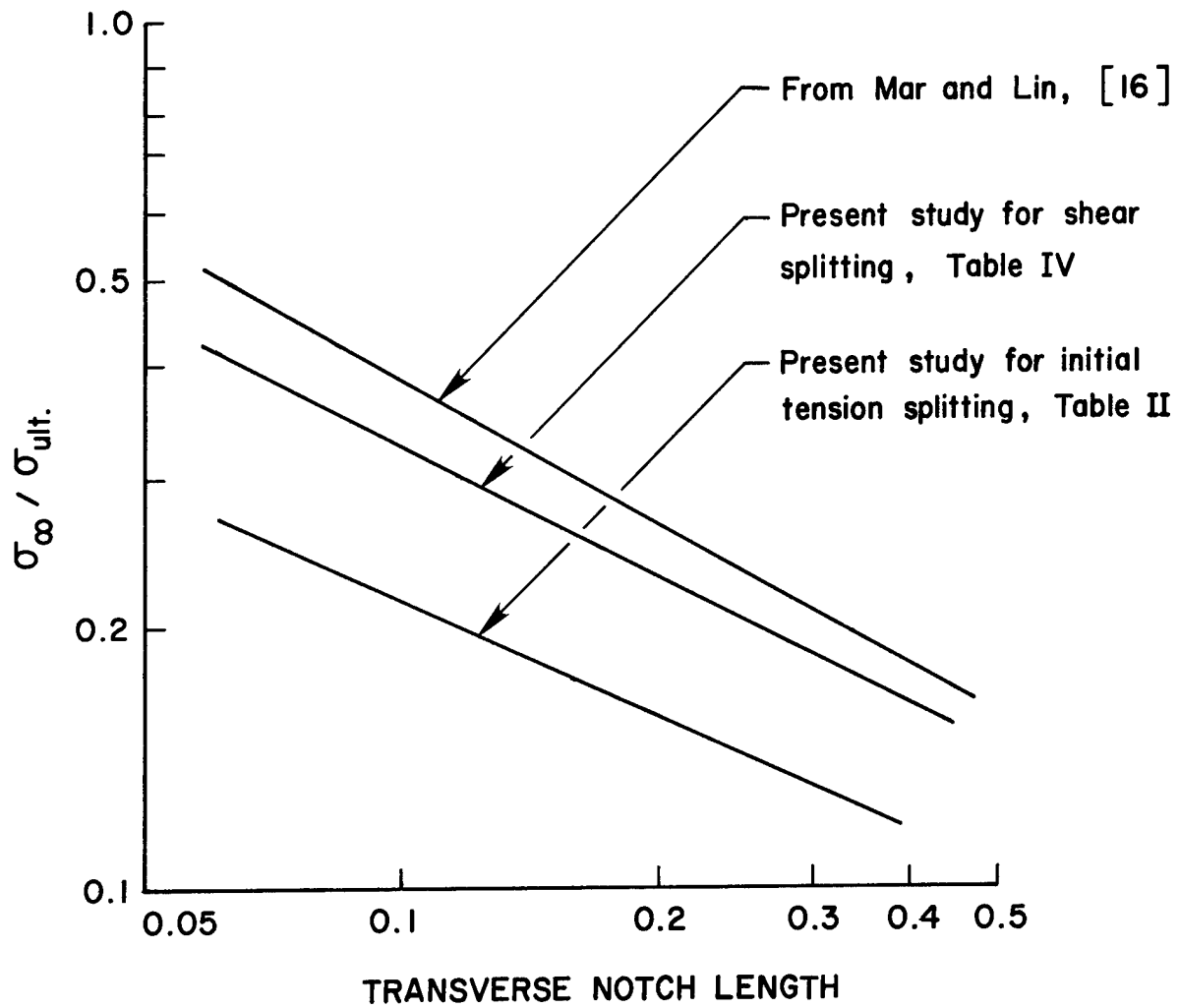
Figure 40. Comparison of split-initiation stress with results of reference [16].

CHAPTER V

CONCLUSIONS

The results of this study show that graphite/epoxy laminates
exhibit a fracture behavior consisting of a region of slow, stable
matrix splitting followed by a region of rapid split growth. The
shear-lag model used by Goree and Gross [10] is unable to describe this
behavior adequately. Whereas, the model is able to predict the initia-
tion of the splits reliably, it is unable to predict the subsequent
split growth. The model does not consider the effects of transverse
matrix normal stresses in the matrix failure criteria and these stresses
appear to be the dominant factor in split initiation and in the slow,
stable split growth region.

As a consequence of the shear-lag assumption for shear stress
transfer, an incorrect boundary condition along the notch surface
arises. The existence of this condition appears to cause the model to
incorrectly determine the transverse matrix normal stresses and, there-
fore, even though it is indicated that normal stresses should be
included, they apparently can not be obtained accurately from the shear-
lag model.

In addition to predicting the actual split initiation stress lev-
els, the model appears to be capable of predicting the stress levels at
which shear failure will begin to dominate the fracture behavior. This
shear failure region is characterized by a large increase in the split
growth rate. The ability to predict the actual split initiation, even
though an incorrect failure criteria is used, indicates that the model
does contain the correct dependency on notch width.

The model is able to predict the split growth rate adequately once shear failure begins to dominate. Discrepancies between the actual and predicted growth rates in this region do exist, but are felt to be primarily due to interference with the fracture path and irregular damage rather than the presence of the matrix normal stresses. The interferences are caused by nonuniformities in the laminate structure which deviate from the assumed structure in the model. Irregular damage in the form of fiber breaks and crossover of matrix splits is not accounted for in the model.

Several recommendations for further work are suggested based on the findings of this study.

1. The mathematical model should be modified to correctly evaluate transverse matrix normal stresses. This is presently being investigated.

2. The matrix failure criteria should be modified to include the effects of transverse matrix normal stresses.

3. The interaction between fracture modes as the split growth rate increases needs to be more clearly understood. The existence of a critical split length at which shear failure begins to dominate needs to be investigated.

4. Further experimental studies should be conducted using a laminate with uniform structural properties such as boron/epoxy.

REFERENCES

1. Jones, R. M., <u>Mechanics of Composite Materials</u>, (McGraw-Hill, New York, 1975).

2. Zweben, C., "Tensile Strength of Fiber-Reinforced Composites: Basic Concepts and Recent Developments," Symposium on Composite Materials: Testing and Design, ASTM STP 460, American Society for Testing and Materials, 1969, pp. 528-539

3. Zweben, C., "Fracture Mechanics and Composite Materials: A Critical Analysis," Analysis of the Test Methods for High Modulus Fibers and Composites, ASTM STP 521, American Society for Testing and Materials, 1973, pp. 65-97.

4. Kanninen, M. F., Rybicki, E. F., and Griffith, W. I., "Preliminary Development of a Fundamental Analysis Model for Crack Growth in a Fiber Reinforced Composite Material," Composite Materials: Testing and Design (Fourth Conference), ASTM STP 617, American Society for Testing and Materials, 1977, pp. 53-69.

5. Hedgepeth, J. M., "Stress Concentrations in Filamentary Structures," NASA TN D-882, May 1961.

6. Hedgepeth, J. M., and Van Dyke, P., "Local Stress Concentrations in Imperfect Filamentary Composite Materials," J. Composite Materials, Vol. 1, (1967), pp.294-309.

7. Hedgepeth, J. M., and Van Dyke, P., "Stress Concentration from Single-Filament Failures in Composite Materials," Textile Research Journal, Vol. 39, (1969), pp. 618-626.

8. Eringen, A. C., and Kim, B. S., "Stress Concentration in Filamentary Composites with Broken Fibers," Princeton University Tech. Report No. 36, September 1973.

9. Goree, J. G., and Gross, R. S., "Stresses in a Three-Dimensional Unidirectional Composite Containing Broken Fibers," Engineering Fracture Mechanics, Vol. 13, (1980), pp. 395-405.

10. Goree, J. G., and Gross, R. S., "Analysis of a Unidirectional Composite Containing Broken Fibers and Matrix Damage," Engineering Fracture Mechanics, Vol. 13, (1979), pp. 563-578.

11. Dharani, L. R., Jones, W. F., and Goree, J. G., "Mathematical Modeling of Damage in Unidirectional Composites," Engineering Fracture Mechanics, Vol. 17, No. 6, (1983), pp. 555-573.

12. Brinson, H. F., and Yeow, Y. T., "An Experimental Study of the
    Fracture Behavior of Laminated Graphite/Epoxy Composites,"
    Composite Materials: Testing and Design, ASTM STP 617, Ameri-
    can Society for Testing and Materials, 1977, pp. 18-38.

13. Peters, P., "Fracture Mechanical Investigations on Unidirectional
    Boron/Aluminum and Boron/Epoxy Composites," J. Composite Mate-
    rials, Vol. 12, (1978), pp. 250-261.

14. Awerbuch, J., and Hahn, H. T., "Fracture Behavior of Metal Matrix
    Composites," Proc. of the Soc. of Engr. Science, Recent
    Advances in Engineering Science, 1977, pp. 343-350.

15. Goree J. G., and Jones, W. F., "Fracture Behavior of Unidirec-
    tional Boron/Aluminum Composite Laminates," NASA CR 3753,
    December 1983.

16. Mar, J. W., and Lin, K. Y., "Characterization of Splitting
    Process in Graphite/Epoxy Composites," Carbon Reinforced
    Epoxy Systems, Part III, Vol. 9, Mat. Tech. Series,
    Technomic Press 1982, pp. 38-47.

17. Stephens, R. W. B., and Pollack, A. A., "Waveforms and Frequency
    Spectra of Acoustic Emissions," J. Acoustical Society of Amer-
    ica, Vol. 50, Part 2, No. 3, (1971), pp. 904-910.

18. Graham, L. J., and Alers, G. A., "Acoustic Emission in the Fre-
    quency Domain," Monitoring Structural Integrity by Acoustic
    Emission, ASTM STP 571, American Society for Testing and Mate-
    rials, 1975, pp. 11-39.

19. Evans, A. G., and Linzer, M., "Acoustic Emission in Brittle Materi-
    als," Annual Review of Material Science, Vol. 7, 1977, pp.
    179-208.

20. Tetelman, A. S., and Evans, A. G., "Failure Prediction in Brittle
    Materials Using Fracture Mechanics and Acoustic Emission,"
    Fracture Mechanics of Ceramics, Vol. 2, Microstructure, Mate-
    rials, and Applications, 1974, pp. 895-924.

21. Harris, D. O., Tetelman, A. S., and Darwish, F. A., "Detection of
    Fiber Cracking By Acoustic Emission," Acoustic Emission,
    ASTM STP 505, American Society for Testing and Materials,
    1972, pp. 238-249.

22. Hennecke, E. G., III, and Jones, G. L., "Description of Damage in
    Composites by Acoustic Emission," Materials Evaluation, Vol.
    37, No. 8, (1979), pp. 70-75.

23. Rotem, A., and Altus, E., "Fracture Modes and Acoustic Emission of
    Composite Materials," J. Testing and Evaluation, Vol. 7, No. 1,
    (1979), pp. 33-40.

24. Hamstad, M. A., "Testing Fiber Composites with Acoustic Emission Monitoring," J. Acoustic Emission, Vol. 1, No. 3, (1982), pp. 151-164.

25. Hamstad, M. A., "Acoustic Emission Uses in Research and Development of Composite Materials," UCRL-76257, Lawrence Livermore Laboratory, 1974.

26. Bailey, C. D., Hamilton, J. M., Jr., and Pless, W. M., "Acoustic Emission of Impact-Damaged Graphite/Epoxy Composites," Materials Evaluation, Vol. 37, No. 6, (1979), pp. 43-48.

27. Bailey, C. D., Freeman, S. M., and Hamilton, J. M., Jr., "Acoustic Emission Monitors Damage Progression in Graphite Epoxy Structure," Materials Evaluation, Vol. 38, No. 8, Aug. 1980, pp. 21-27.

28. Goree, J. G., and Venezia, W. A., "Bonded Elastic Half-Planes with an Interface Crack and a Perpendicular Intersecting Crack that Extends into the Adjacent Material-I," I. J. Engineering Science, Vol. 15, No. 1, 1977, pp. 1-18.

29. Awerbuch, J., and Hahn, H. T., "Off-Axis Fatigue of Graphite/Epoxy Composite," Fatigue of Fibrous Composite Materials, ASTM STP 723, American Society for Testing and Materials, 1981, pp. 243-273.

1. Report No. NASA CR-3881	2. Government Accession No.	3. Recipient's Catalog No.
4. Title and Subtitle Longitudinal Splitting in Unidirectional Composites, Analysis and Experiments		5. Report Date April 1985
		6. Performing Organization Code
7. Author(s) James G. Goree and Jeffrey M. Wolla		8. Performing Organization Report No.
		10. Work Unit No.
9. Performing Organization Name and Address Department of Mechanical Engineering Clemson University Clemson, SC 29631		11. Contract or Grant No. NSG-1297
		13. Type of Report and Period Covered Contractor Report
12. Sponsoring Agency Name and Address National Aeronautics and Space Administration Washington, DC 20546		14. Sponsoring Agency Code 505-33-33-05

15. Supplementary Notes

Langley Technical Monitor: Clarence C. Poe, Jr.
Final Report

16. Abstract

An experimental study is conducted to determine the fracture behavior of center notched, unidirectional graphite/epoxy laminates when subjected to tensile loading. The actual behavior is compared to the behavior predicted by a mathematical model based on classical shear-lag assumptions. The model allows for damage to occur in the form of longitudinal matrix yielding and splitting with the matrix assumed to fail in pure shear. Acoustic emission monitoring techniques are used to detect the initiation of matrix splitting, while radiographic and brittle lacquer coating techniques are used to determine the amount of matrix damage as a function of remote stress. Results indicate that the model is capable of predicting split initiation stress levels accurately, but does not describe the subsequent split growth adequately. The model predicts rapid split growth following split initiation due to shear failure, while the actual behavior involves a slow split growth region prior to the rapid growth region. It is suggested that transverse matrix normal stresses are responsible for split initiation and the early, slow split growth. The model predicts the actual initiation stress levels reliably, and also appears to be able to predict the point at which the shear failure mode begins to dominate. The shear failure mode does eventually dominate, but at a slower rate than predicted. The nonuniform structure of the graphite/epoxy laminates is thought to be responsible for decreasing the split growth rate due to shear failure.

17. Key Words (Suggested by Author(s)) Composite laminate Fracture Crack growth Graphite/Epoxy	18. Distribution Statement Unclassified-Unlimited Subject Category 24		
19. Security Classif. (of this report) Unclassified	20. Security Classif. (of this page) Unclassified	21. No. of Pages 114	22. Price A06